MTL TR 89-20

AD

THE INFLUENCE OF SECOND-PHASE DISPERSIONS ON SHEAR INSTABILITY AND FRACTURE TOUGHNESS OF ULTRAHIGH STRENGTH 4340 STEEL

JOHN G. COWIE
METALS RESEARCH BRANCH

March 1989

US ARMY
LABORATORY COMMAND
MATERIALS TECHNOLOGY LABORATORY

U.S. ARMY MATERIALS TECHNOLOGY LABORATORY
Watertown, Massachusetts 02172-0001

The findings in this report are not to be construed as an official Department of the Army position, unless so designated by other authorized documents.

Mention of any trade names or manufacturers in this report shall not be construed as advertising nor as an official indorsement or approval of such products or companies by the United States Government.

DISPOSITION INSTRUCTIONS

Destroy this report when it is no longer needed.
Do not return it to the originator

UNCLASSIFIED

SECURITY CLASSIFICATION OF THIS PAGE (When Data Entered)

REPORT DOCUMENTATION PAGE		READ INSTRUCTIONS BEFORE COMPLETING FORM
1. REPORT NUMBER MTL TR 89-20	2. GOVT ACCESSION NO.	3. RECIPIENT'S CATALOG NUMBER
4. TITLE (and Subtitle) THE INFLUENCE OF SECOND-PHASE DISPERSIONS ON SHEAR INSTABILITY AND FRACTURE TOUGHNESS OF ULTRAHIGH STRENGTH 4340 STEEL		5. TYPE OF REPORT & PERIOD COVERED Final 6. PERFORMING ORG. REPORT NUMBER
7. AUTHOR(s) John G. Cowie		8. CONTRACT OR GRANT NUMBER(s)
9. PERFORMING ORGANIZATION NAME AND ADDRESS U.S. Army Materials Technology Laboratory Watertown, Massachusetts 02172-0001 SLCMT-EMM		10. PROGRAM ELEMENT, PROJECT, TASK AREA & WORK UNIT NUMBERS D/A Project: 1L162105AH84
11. CONTROLLING OFFICE NAME AND ADDRESS U.S. Army Laboratory Command 2800 Powder Mill Road Adelphi, Maryland 20783-1145		12. REPORT DATE March 1989 13. NUMBER OF PAGES 140
14. MONITORING AGENCY NAME & ADDRESS(if different from Controlling Office)		15. SECURITY CLASS. (of this report) Unclassified 15a. DECLASSIFICATION/DOWNGRADING SCHEDULE

16. DISTRIBUTION STATEMENT (of this Report)

Approved for public release; distribution unlimited.

17. DISTRIBUTION STATEMENT (of the abstract entered in Block 20, if different from Report)

18. SUPPLEMENTARY NOTES

Thesis submitted to Worcester Polytechnic Institute, Worcester, Massachusetts, in partial fulfillment of the requirements for the Degree of Doctor of Philosophy in Materials Science and Engineering, December 1988.

19. KEY WORDS (Continue on reverse side if necessary and identify by block number)

Ordnance steel
High strength alloys
Fracture (mechanics)
Toughness
Dispersion relations
Shear tests
Shear properties
Plastic deformation

20. ABSTRACT (Continue on reverse side if necessary and identify by block number)

(SEE REVERSE SIDE)

DD FORM 1 JAN 73 1473 EDITION OF 1 NOV 65 IS OBSOLETE

UNCLASSIFIED

SECURITY CLASSIFICATION OF THIS PAGE (When Data Entered)

Block No. 20

ABSTRACT

The resistance to shear instability and subsequent flow localization in ultrahigh strength (UHS) steels is dependent upon second-phase particle dispersions and the matrix strain hardening. The effect of the interparticle spacing (λ) to the geometric mean particle radius (R) ratio on the shear instability strain of UHS 4340 steel is discussed. Experimental results indicate a linear relationship exists between shear instability strain and this λ/R ratio. Microvoid nucleation softening associated with second-phase particles appears to be the dominant destabilizing event leading to fracture. Strain rate and hydrostatic compression effects are also discussed.

Experimental results of modes I and II fracture toughness testing are compared and contrasted. A high hydrostatic tension field was found to be the cause for the lower mode I critical stress intensity factor (K_{Ic}) than mode II (K_{IIc}). The high hydrostatic tensile stress field induced early microvoid nucleation which promoted flow localization leading to fracture. However, both mode I (K_{Ic}) and mode II (K_{IIc}) critical stress intensity factors directly related to the critical particle distance ($\lambda/\sqrt{R}$).

A bimodal fracture toughness model has been developed for this material and failure mechanism, which relates K_c to a combination of microstructural features and stress-strain behavior. Excellent agreement was found between calculated and measured mode I fracture toughness values. The calculated mode II fracture toughness did not relate as well to the measured toughness values due to the influence of hydrostatic compression on the shear instability strain.

TABLE OF CONTENTS

LIST OF TABLES

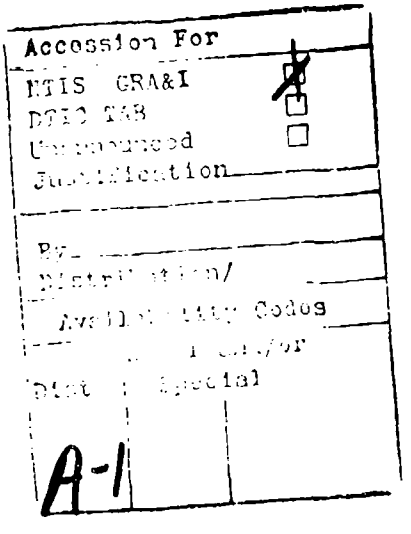

LIST OF FIGURES

ACKNOWLEDGEMENTS

Sincere thanks to my advisor, Professor Floyd Tuler, for his guidance and inspiration in this research project. His knowledge and experience contributed greatly to the successful completion of this work.

In addition, the constant interest and financial support of the U.S. Army Materials Technology Laboratory, Watertown, Massachusetts is deeply appreciated. Especially Dr. Morris Azrin, Dr. Eric B. Kula, and Dr. Gregory B. Olson who's help was necessary to the completion of this research. It is my hope that the results contained within benefit the U.S. Army in some way.

I would also like to express my appreciation and gratitude to my wife, Kerry N. Siebein, whose TEM expertise proved invaluable, without which the research could not have been a success.

I am deeply grateful to Professor Ronald R. Biederman entrusting me with his TEM after business hours. Special thanks to both John V. Kelley Jr. and John B. Breedis who helped me immensely with the nearly endless details associated with experimental research.

I am indebted to Professor Norman Fleck for the very fruitful discussion we had concerning fracture toughness which later led to the development of the K_{Ic} - materials properties model.

INTRODUCTION

The phenomenon of shear instability and flow localization in ultrahigh strength (UHS) steels is of considerable interest because it is one of the principal fracture mechanisms during ballistic penetration. This fracture mechanism is a limiting factor in the design and use of UHS steel armor. Much of the reported research has focused on the thermal softening effect arising from the high strain rate adiabatic constraint. The conventional view is that the phenomenon can be treated as a continuum plastic instability problem. Models based on isothermally derived empirical constitutive relations have been used to account for strain localization conditions observed in high strain rate shear tests, but recent experiments have cast doubt on the validity of this approach [1]. Experimental evidence strongly suggests that flow localization in UHS steels is driven by microvoid softening controlled by nucleation at fine dispersions [2]. In addition, a direct correlation has been demonstrated to exist between fracture toughness and shear instability strain in these steels [2]. This study is aimed at determining relationships between second-phase particle size, type, and distribution on shear localization and fracture toughness, with the ultimate objective of understanding and controlling the ballistic penetration and dynamic fracture of UHS armor steels.

BACKGROUND

The phenomenon of deformation localization as it occurs in ballistic penetration is illustrated in Figure 1 [3], showing the localized deformation mode of failure, commonly referred to as adiabatic shear. The plastic flow after the onset of shear instability is concentrated in thin shear bands which appear white after metallographic etching. The localized flow produces a 'shear plugging' failure mode in which the material ahead of the projectile is ejected as a solid cylindrical piece absorbing relatively little associated energy.

Much has been written over the past forty years on the subject of shear localization. The reviews by Rogers [4,5] and Bedford [6], give an excellent overview of the general phenomenon including the microstructures resulting from the localized flow. The continuum plasticity theory of adiabatic flow localization is treated by Clifton [7], and a general survey of strain localization is given by Argon [8].

A concise treatment of the specific influence of adiabatic shear in armaments and ballistics can be found in the review of Samuels and Lamborn [9]. Olson *et al.* [10] endeavored to computer model the ballistic penetration event of high strength steels using experimentally derived constitutive flow relations, but met with limited success. The authors proposed that the material exhibited a pressure dependence that the conventional thermal softening models could not describe. Experiments were designed to determine how the pressure dependence affects the deformation of UHS steels.

More recent research by Azrin *et al.* [1], demonstrated that the critical strain for shear localization in UHS 4340 steel is nearly identical for both quasi-static and dynamic loading conditions. While thermal softening undoubtedly provides a contribution to the measured stress-strain relations, this result of nearly identical instability strains and shear

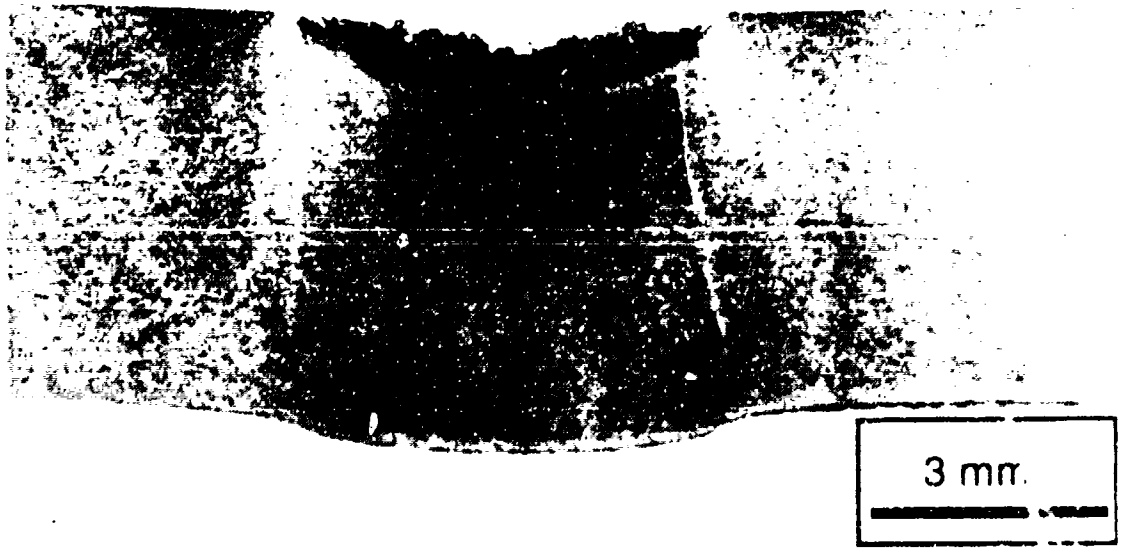

Figure 1. Photomicrograph of a 4340 steel (Rc 52) plate (5.6 mm thick) that underwent a localized failure during ballistic impact. Note the white etched shear bands beneath the area of impact.

localization behavior in UHS steels at both high and low strain rates indicated that another flow softening phenomenon was equally important.

As was reviewed in Olson *et al.* [10], observations that the instability strain is strongly influenced by the hydrostatic component of stress, together with metallographic evidence of microvoid nucleation at second-phase particles, indicate that the fracture related processes can also contribute to the strain softening effects underlying plastic shear localization [2,11,12]. Such phenomena must also be taken into account for a complete understanding of flow localization and subsequent shear banding.

FLOW LOCALIZATION MODELS

Portion of this section were taken directly from the recent review by Cowie and Tuler [13]. This literature review describes the various modelling approaches to the problem of shear localization.

According to Anand [14], *"Our state of understanding of the various features of the shear band localization phenomenon appears to be in its infancy,"* although the beginnings of quantitative models of shear localization have been established [15]. A schematic representation of shear localization and the onset of shear band formation is presented in Figure 2.

The purpose of this literature review is to identify and describe these shear localization models. Various approaches to the problem have been attempted. The diverse models are separated into four categories: flow softening constitutive, deformation heating, textural softening and void nucleation softening models. In addition, a section on flow localization in fracture has been included which describes the state of understanding of the relationship between shear instability and fracture toughness. It is thought that continued progress toward fully understanding shear banding will require corresponding developments in experimentation and modelling.

Flow Softening Constitutive Models

The bifurcation of deformation analysis concentrates on the macroscopic continuum level and explores the conditions for which the pre-localization constitutive relations will permit shear banding. Plastic strain localization owing to flow softening in the presence of metallurgical defects has been modelled by Semiatin and Jonas [16] for axisymmetric

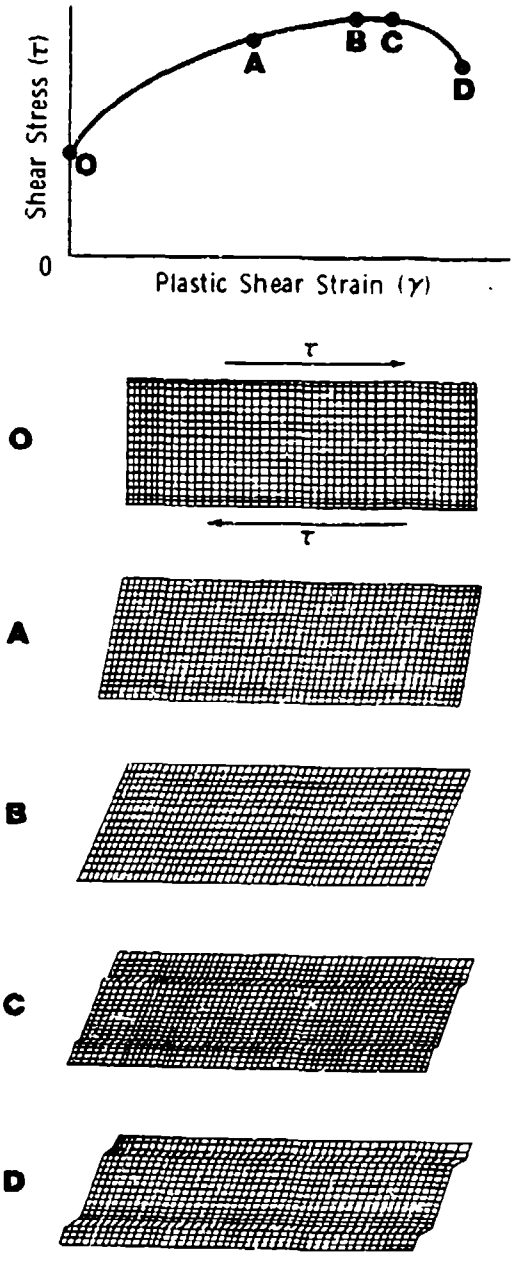

Figure 2. Schematic representation of the shear localization process and an accompanying stress-strain curve. Labelled points on the curve are associated with the various stages of deformation of the block of material. The material begins to yield (0), and then undergoes uniform deformation (A,B) up to the instability (C), after which shear bands begin to form (D).

deformation such as isothermal uniaxial compression. The model requires that the material behaves according to the parabolic strain and strain rate laws

$$\tau = k\,\dot{\gamma}^{m}\,\gamma^{n}$$

where τ is the shear flow stress, k is the material constant, $\dot{\gamma}$ is the shear strain rate, γ is the shear strain, m is the strain rate sensitivity exponent, and n is the strain hardening exponent.

Additional restrictions of this model are that the material is isotropic, the von Mises yield criterion holds, and the deformation is performed under plane strain conditions. The model uses a strain-dependent flow localization parameter (α) to rank the materials according to their tendency for shear instability. The flow localization parameter is calculated from experimentally determined material parameters

$$\alpha = \frac{1}{\sigma}\frac{d\sigma}{d\varepsilon}\bigg|_{\dot{\varepsilon}}$$

where σ is the flow stress, ε is the strain, and $\dot{\varepsilon}$ is the strain rate. For a given strain, if α is greater than zero, flow localization is permitted whereas, when α is less than zero, no localization can occur.

Deformation Heating

Deformation-heating-produced flow softening models have been developed. Starting with a mechanical equation of state originally formalized by Baron [17], Culver [18] derived a thermal instability model which was then modified by Semiatin and Jonas

[16]. This model has led to a simple equation relating the critical strain to localization (γ_i) during high strain rate deformation to other experimentally determined parameters

$$\gamma_i = - \frac{\rho c n}{\beta \left(\frac{\partial \tau}{\partial T}\right)\Big|_{\gamma \dot{\gamma}}}$$

where ρ is the density, c is the specific heat, n is the work hardening exponent, τ is the shear flow stress, T is the temperature, γ is the shear strain, $\dot{\gamma}$ is the shear strain rate, and β is the fraction of plastic work converted to heat.

This model was subsequently tested by Staker's expanding cylinder tests [19]. Staker's experimental results show that localization occurred for $\alpha > 3.5$ (not $\alpha > 0$ as predicted by the model), which somewhat supports this deformation heating model (Figure 3).

A more recent thermoplastic instability model has been proposed by Clifton *et al.* [20] which in some ways resembles Culver's analysis [18]. The resulting final relation equates the instability strain under high strain rate conditions with material parameters

$$\gamma_i = \frac{m}{\frac{\beta \tau \upsilon}{\rho c T} - \frac{n}{\gamma}}$$

where υ is the thermal softening parameter.

However, experimental data on high strength AISI 4340 steel have revealed that strain rate has no effect on the critical strain to localization (Figure 4) [1]. Therefore, it is concluded that adiabatic heating had little influence on initiating an instability in high strength steel and that other phenomena are responsible for producing the softening [1].

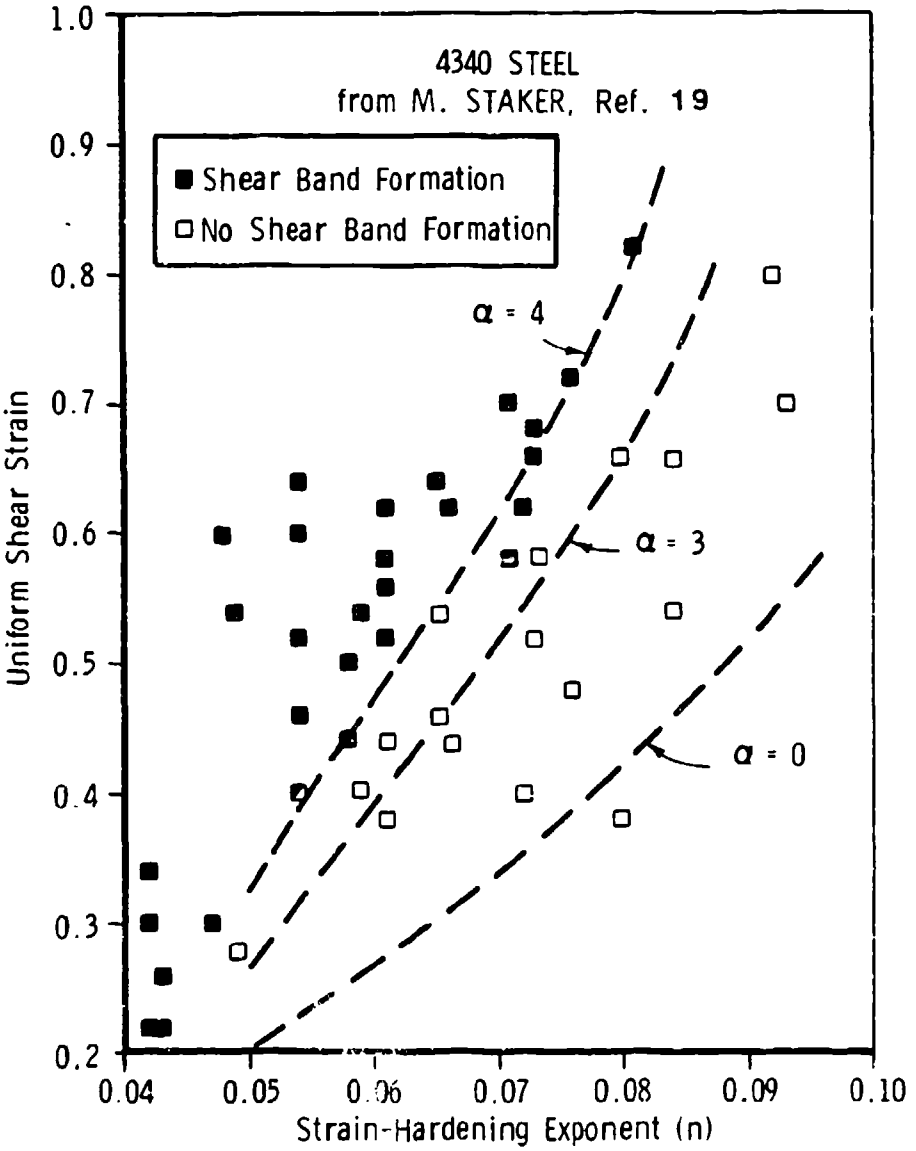

Figure 3. Shear strain data plotted as a function of the strain-hardening exponent. Data taken from Staker's [19] expanding cylinder tests on 4340 steel: - , constant flow localization parameters.

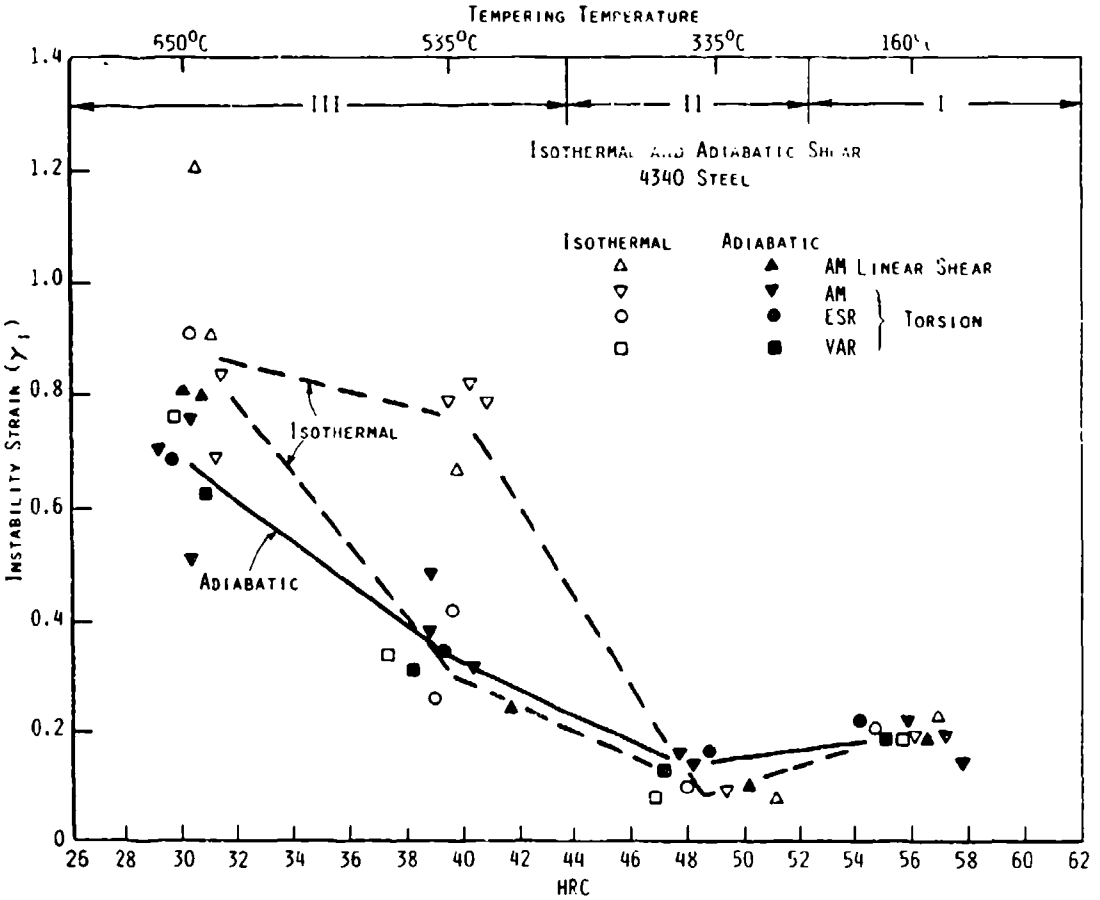

Figure 4. Experimental data [1] of shear tests performed on three different melting practices of 4340 steel: air melted (AM), electro-slag remelted (ESR), and vacuum arc remelted (VAR). Tests were performed at both high (adiabatic) and low (isothermal) strain rates over a range of Rockwell C hardness levels. There is little strain rate effect on the instability strain, especially at the higher hardness levels.

Textural Softening

Even though shear band initiation is commonly associated with softening, there exists little evidence for flow softening before localization under isothermal conditions [21]. This does not preclude some type of softening mechanism from involvement in initiating shear bands. Textural or geometric softening resulting from lattice reorientation during straining produces soft textures with respect to shear bands [21]. A material's resistance to strain localization may be bound by some intrinsic characteristic of the plastic flow process such as the yield surface vertex structure which originates from the inherent nature of crystalline slip [21,23]. Shear strain localization can occur if a vertex develops on the yield surface defined for the material [22].

The extent to which textural softening influences the promotion of shear instability is directly related to the amount of uniform strain preceding the localization. In other words, higher strength materials which receive small strains preceding localization have a lesser textural softening effect. The converse is also true.

Although much experimental and analytical work has been performed on lower strength materials in the form of sheet metal forming tests, no research on the textural softening effect has been reported on these higher strength materials. To separate the effects of textural softening from the other metallurgical factors contributing to strain localization, shear tests similar to those performed by Azrin *et al.* [1] should be performed on highly textured, high strength material and compared with the isotropic counterpart.

Void Nucleation Softening

Not all localization phenomena can be considered applicable to the bifurcation of deformation theoretical model. A bifurcation analysis cannot allow for the important role of

material defects in shear band initiation [24]. The critical strain at which strain localization develops in addition to the susceptibility to plastic instability is acutely sensitive to material inhomogeneities [25]. When subjected to an increasing triaxial stress state, void nucleation can promote plastic flow localization and shear instability [23,26]. A sudden burst of nucleation events may result in a destabilization of the plastic flow by strain localization into shear bands [26,27]. The existence of voids can substantially change the bulk plastic flow constitutive relationship.

For the purposes of modelling, the material can then be viewed as a plastically dilating continuum which allows the possibility of strain softening, with simultaneous strain hardening of the surrounding matrix material [21,28]. Likewise, the macroscopic effect of void formation has been modelled as an apparent volume loss of load-bearing material [29]. A variety of local material defects will always exist in real materials, and it is probable that the numerous closely spaced shear bands, observed by Anand and Spitzig [30] in a maraging steel at relatively small strains, are localizations initiated by inhomogeneities.

The softening induced by microvoid nucleation produces macroscopically observable strain localization [31]. Therefore, an established critical stress void nucleation model is included in this review. A critical stress criteria model based on dislocation models developed by Argon *et al.* [32] provides the relationship for the inclusion-matrix interfacial stress (for large inclusions where the radius $R > 100$ Å). For materials which have a large interparticle spacing (λ), the inclusions can be considered non-interacting. The equation for the interfacial stress is

$$\sigma_{rr} = k_o\left[\left(\frac{\gamma}{\gamma_o}\right)^{1/n} + \sqrt{3}\left\{\frac{\sqrt{6}\,(1+n)}{M}\frac{\gamma}{\gamma_o}\right\}^{1/(1+n)}\right].$$

For materials which have a small interparticle spacing, the inclusions can be considered interacting. The equation for the interfacial stress becomes

$$\sigma_{rr} = k_o\left[\left(\frac{\gamma}{\gamma_o}\right)^{1/n} + \sqrt{3}\left\{\frac{\sqrt{3}\left(\frac{\gamma}{\gamma_o}\right)}{\left(\frac{\lambda}{R}\right)}\right\}^{1/n} + \frac{\sqrt{6}}{M}\frac{\lambda}{R}\right]$$

where σ_{rr} is the interfacial tensile stress, k_o is the yield stress in shear, γ is the shear strain, γ_o is the shear strain at yield, n is the stain hardening exponent, M is the Taylor factor, λ is the interparticle spacing, and R is the particle radius.

Interactions between inclusions occur when the plastic zones of neighboring particles touch. The critical strain ratio for particle interaction is determined by [32]

$$\left(\frac{\gamma}{\gamma_o}\right) = \frac{M}{\sqrt{6}\,(n+1)}\left(\frac{\sqrt{2}}{M}\frac{\lambda}{R}\right)^{n+1}.$$

When the volume fraction of inclusions is small, the particles act in isolation to very large strains. In addition, the interfacial stress is independent of the inclusion radius and spacing. However, when the volume fraction is large, the particles interact at very small strains. The interactions enhance the interfacial stress and hasten particle-matrix separation, *i.e.*, void nucleation [33]. The critical interfacial stress to void nucleation varies with the size and distribution of particles. The number of nucleated voids is a direct function of the λ/R ratio. Given the same volume fraction (*i.e.*, the same λ/R ratio), small, evenly distributed particles permit larger strains prior to void nucleation. Conversely, large or unevenly distributed particles nucleate at relatively small strains, and ultimately degrade the material's ductility [33]. Therefore, it can be inferred that both ductility and fracture toughness depend on the critical interfacial stress to nucleation.

From tension tests performed on three different materials by Argon and Im [33], good agreement was found between theory and experiment. They calculated that void nucleation occurs at second-phase particles or inclusions when the interfacial stress produced by the combined effect of hydrostatic tension and drag of the plastically flowing matrix equals the interfacial cohesive strength. For spheroidized 1045 steel, the experimentally calculated strength was 35.1 MPa. However, the theoretically calculated interfacial strength was 77.6 MPa, considering no particle interactions, and 41.0 MPa with particle interactions considered. This good agreement between theory and experiment leads to the assumption that this model is valid.

Flow Localization in Fracture

Current research is focusing on the role of flow localization in fracture of elastoplastic materials under quasi-static conditions. When flow localization develops in advance of a pre-existing microcrack as a result of the interactions of microstructural inhomogeneities, local hydrostatic stresses and strain concentrations necessary to drive the fracture process are attained within the shear band. High concentrations of microstructural inhomogeneities result in early degradation of a material's load bearing capacity [34]. Microvoid nucleation can be regarded as the micromechanism responsible for plastic instability and constitutes an important fracture process for elastoplastic materials.

In the case of spheroidized steel, the value of critical strain at which strain localization initiates is approximately the strain at the microscopic level for microcrack extension [35,36]. Numerical models based on J_2 corner theory of plasticity demonstrate that the shear bands initiate at the surface of a blunted crack tip [37]. Together, these observations indicate that microvoid nucleation and flow localization are part of the fracture process, and govern the prevailing deformation field in the process zone [34].

The destabilizing influence of void formation increases with interfacial stress to void nucleation [34]. In other words, the size, type and distribution of the inhomogeneities present in the material, the matrix strain hardening rate and the local stress state control the extent of the localized void profusion and the promotion of plastic instability. The extent of localized void profusion governs the ease of microcrack extension. The onset of crack propagation as enhanced by void profusion is usually signified by a pop-in failure, *i.e.*, a rapid load drop following maximum load in a load displacement curve. However, crack tip blunting is more prominent when the void profusion is more homogeneous, leading to higher toughness as crack propagation becomes dependent on the plastic deformation involved in void growth and coalescence rather than localization.

Schwalbe [38] lists two of the more successful relationships between K_{Ic}, particle spacing and other material properties

$$K_{Ic} = \frac{\sigma_{ys}}{(1-2\upsilon)} \sqrt{\lambda\pi\,(1+n)\left\{\frac{\varepsilon_f^{\bullet} E}{\sigma_{ys}}\right\}^{(1+n)}}$$

and

$$K_{Ic} = \sqrt{4.55\,(\varepsilon_f^{\bullet} + 0.23)\,\lambda E \sigma_{ys}}$$

where

$$\varepsilon_f^{\bullet} = \frac{\delta_{crit}}{2r}$$

and δ_{crit} is the critical crack tip opening displacement, r is the width of region of intense plastic deformation in the vicinity of the crack tip, σ_{ys} is the yield strength, υ is Poisson's ratio, λ is the interparticle spacing, n is the matrix strain hardening exponent, and E is the modulus of elasticity.

The onset of crack propagation in precracked elastoplastic components is sometimes preceded by crack tip blunting. The crack growth controlling micromechanism, whether void nucleation and flow localization or void growth and coalescence, is expected to

determine whether the crack extends as a mode II shear crack along an instability trace (for lower toughness), or blunts and grows by void coalescence (for higher toughness).

The factor which controls the magnitude of the stress intensity factor, where the crack extension mechanism is a microvoid coalescence, is the nucleation event. The nucleation event governs the initial void size in addition to the spacing between voids. However, it is the initial void spacing that controls the final dimple size after coalescence [39]. The fracture processes are neither considered nor resolved by the present continuum mechanics fracture toughness models. In addition, little experimental data pertinent to the nucleation event have been published.

Flow Localization Summary

The various models of flow localization have been reviewed. The flow softening constitutive models provide a convenient way of ranking materials in order of their tendency to form shear bands. However, constitutive models deal only with the macroscopic phenomena and there is no provision for the inclusion of microscopic parameters. The deformation heating models permit the calculation of a material's instability strain - specifically at high strain rates. As in the case of flow softening constitutive models, deformation heating models employ only bulk material properties and do not allow for microscopic inhomogeneities. Textural softening models incorporate a geometric softening resulting from lattice reorientation during straining which produces soft crystallographic textures with respect to shear bands. These models also fail to consider the influence of microscopic inhomogeneities on shear localization. Additionally, textural softening models are more applicable to low strength materials. Void nucleation softening provides a micromechanism by which flow localization can occur in engineering alloys. This theory demonstrates that ductility is directly related to the critical interfacial stress to nucleation for a second-phase particle. Lastly, fracture has been related to the susceptibility

of a particular material to flow localization. Consequently, fracture toughness is a function of the size, type and distribution of second-phase particles.

I believe that microvoid nucleation softening models provide an appropriate description of the shear localization behavior in ultrahigh strength steels. In addition, I contend that fracture is related to second phase particles through the microvoid induced shear localization process in theses steels. It is my hope to prove these theories in this thesis.

RESEARCH PROGRAM

This study was initiated to quantitatively determine a relationship between the second-phase particles, shear instability, and fracture toughness for UHS 4340 steel. Experiments were also devised to study the effect of both hydrostatic stress and normalizing temperature on the critical strain to localization and fracture toughness.

A simple shear specimen was used to measure instability strain as described in the Experimental Procedure section of this study. Stress-strain data and corresponding strain profiles were obtained from each test in order to quantify the flow behavior in addition to accurately determining the instability strain.

Quantitative metallography was performed on each specimen to determine the type, size and distribution of the second-phase particles. A comparison was made between mode I (tension) and mode II (shear) fracture.

Flow localization models are also described. A simple model relating fracture toughness and microstructural features and properties has been developed from first principles. The model is derived in the Toughness-Instability Correlations section of this study.

EXPERIMENTAL PROCEDURE

In this study, a vacuum-arc remelted (VAR) heat of AISI 4340 steel supplied by Republic Steel was examined. The Chemical Composition is given in Table I. This selection was made since extensive data exist on this heat of steel.

TABLE I. CHEMICAL COMPOSITION OF VAR 4340 STEEL (Weight Percent)

C	Mn	Si	Ni	Cr	Mo	P	S	Cu	Al	N	O	Hppm
0.42	0.46	0.28	1.74	0.89	0.21	0.009	0.001	0.19	0.031	0.005	0.001	1.0

The material was heat treated for one hour at different normalizing temperatures ranging from 845°C to 1100°C. Different normalizing treatments were employed in order to create different second phase sizes and distributions. After normalizing, each specimen was austenitized at 845°C for 15 min. and subsequently oil quenched. By austenitizing all specimens at the same temperature, nearly identical prior austenite grain sizes and retained austenite contents were obtained (see Results section). Two different tempering treatments were used. The first tempering treatment was performed at 200°C for 2 hours which resulted in a martensitic (stage I) structure with a fine dispersion of ε–carbides and also results in a maximum in the sharp crack toughness for UHS 4340 steel [40]. If tempering is performed at temperatures greater than 200°C (stage II and III), the benefit obtained through the dissolution of second-phase particles is lost, due to microvoiding at cementite particles [2]. The second tempering treatment was performed at 650°C for 2 hours which resulted in a spheroidized cementite dispersed in lath martensite (stage III) structure.

The first aim of the research was to characterize the second-phase dispersions in each specimen in terms of type, size, and distribution as a function of the heat treatment.

The second aim was to relate these quantified microstructural characteristics to the tendency for shear localization. Shear tests were performed to obtain shear stress-strain curves in order to relate them to the microstructure. It has been shown that shear instability is induced by microvoid nucleation softening in the material and consequently is dependent on the particle dispersions and the local stress state [2]. Therefore it was desired to identify the microvoid initiating particles and determine how this varies with normalizing temperature and the local stress state. By normalizing over a range of temperature, variations in particle size and distribution were achieved. Theoretical calculations reported in the literature indicate that shear instability is more sensitive to inhomogeneities in the distribution than to the overall volume fraction [41-43].

The third segment of the program involved fracture toughness testing of the various heat treated specimens. The toughness behavior of UHS steel to high temperature solutionizing has been well documented [44-47]. It was desired to obtain fracture toughness data as a function of solutionizing treatment given a nearly constant austenite grain size and retained austenite content. Consequently, various normalizing treatments were performed followed by a single short austenitizing treatment in order to study just the effects of dispersions on the fracture process without the complicating effects of grain size and retained austenite variations. Both mode I (tension) and mode II (shear) loading configurations were tested in order to determine the effect of hydrostatic stress on toughness.

Quantitative Metallography

In order to relate the mechanical properties to the second-phase particles, it was necessary to accurately determine particle size, type and distribution through quantitative electron microscopy incorporating a statistical error analysis. The method used for determining the size of the nearly spherical particles was diametral measurement in the

plane of intersection of extracted particles. The replication technique was originated by Fisher [48] as a means of identifying precipitates in steel.

Two stage extraction replicas were taken from the electropolished surface of each specimen. Electropolishing was performed at 25 volts for 15 seconds in a polishing solution of 10% perchloric acid and ethanol at room temperature. Electropolishing selectively polished the matrix material leaving the particles protruding from the surface. A thin sheet of acetyl cellulose film (Bioden®) was dissolved onto the specimen with reagent grade acetone and allowed to harden. At this stage, the particles were embedded into the replica material. The acetyl cellulose film was then stripped from the polished surface and subsequently coated with a thin layer of amorphous carbon using a vacuum carbon evaporation technique. During coating, the replica was continually rotated so that a uniform carbon layer is applied. The replica was then cut into 3 mm squares and placed on 100 mesh TEM specimen support grids. Lastly, the acetyl cellulose film was dissolved in several baths of reagent grade acetone and the replica was allowed to air dry.

This technique serves the purpose of a replica only in the sense that the contrast is enhanced at the extracted particles as compared with the electron beam intensity transmitting through the carbon support film as background. The unique advantage of extraction replication does not lie in the enhanced image contrast but rather in the ability to accurately measure the particle sizes and to identify the chemical nature of the particles by using energy dispersive x-ray spectroscopy. The usefulness of extraction replication therefore, really lies in the microscopy of the intrinsic particle structure. Random sampling was employed to obtain statistically significant data. Hundreds of particles per specimen were measured. Log-normal particle size distribution curves were produced for each specimen (see Results section), and geometric mean particle radii (R) were determined from these data. A statistical analysis was performed to indicate the relative accuracy of these

geometric mean radii. Statistical equations taken from Vander Voort [49] were used in this analysis.

The average deviation from the geometric mean is conveniently expressed by calculation of the standard deviation s of the data

$$s = \sqrt{\frac{\sum (R_i - R)^2}{N - 1}}$$

where R_i is the individual radius measurement, R is the geometric mean particle radius, and N is the total number of measurements. Although the standard deviation is an absolute measure of data dispersion, it is difficult to compare standard deviations when the mean values differ somewhat. It is useful to calculate the 95 percent confidence limit (95%CL) and the percent relative accuracy (%RA). The 95% CL can be determined

$$95\ \%\ CL = \frac{t\ s}{\sqrt{N - 1}}$$

where t is the confidence level which is equal to 2 for $60<N<120$ [49]. This 95 %CL is taken as the error of the mean particle radius value. In other words, if the mean radius was measured repeatedly, 95 times out of 100 times, the mean radius would fall within this error band. The percent relative accuracy (%RA) is determined by dividing the 95%CL by the mean radius and expressing it as a percentage

$$\%RA = \frac{95\%\ CV}{R} \times 100.$$

For determining the distribution of particles, two dimensional stereallographic data must be converted to three dimensional space [49]. Values of particle count per unit area (N_A) were obtained by simply counting the number of particles intercepting a planer section using scanning electron microscopy (SEM). SEM was used because the particles fluoresce making them easy to visualize, and because it was thought that not all particles

contained in a planer section would be extracted by the replication technique. The volume fraction (f_v) is determined from the planer relationship with N_A

$$f_v = N_A (\pi R^2)$$

where R is the geometric mean particle radius. More important than the volume fraction is the physically meaningful interparticle spacing (λ). In order to determine this spacing, the particle count per unit volume (N_v) must first be determined from the volume fraction and mean radius

$$N_v = \frac{f_v}{4/3\ \pi\ R^3}\ .$$

The interparticle spacing (λ) is defined as the mean distance from the centers of adjacent particles

$$\lambda = N_v^{-1/3}.$$

The mean particle radii confidence limits were carried through the above calculations resulting in interparticle spacing values having their own 95 percent confidence limits.

Shear Localization Testing

The specimen geometry consisted of a Charpy sized specimen with two narrow gauge sections which are displaced simultaneously under simple shear conditions. This specimen (Figure 5), commonly referred to as the double linear shear specimen, was employed for both quasi-static and dynamic tests. Dynamic tests were performed in a modified instrumented Charpy machine. The Charpy specimen fixture was replaced with one that rigidly holds the ends of the double linear shear specimen. In addition, the pendulum weight was increased by sixty percent in order to reduce the amount of deceleration during straining thereby maintaining a relatively constant strain rate. The shear

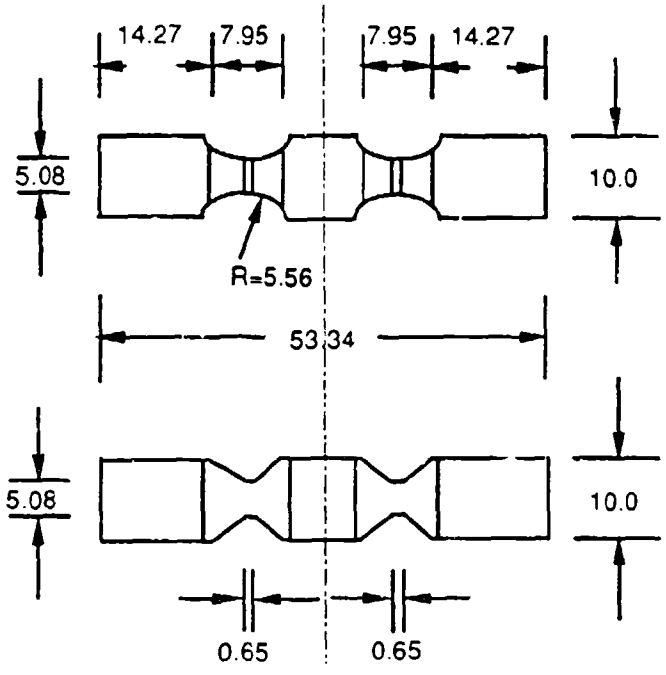

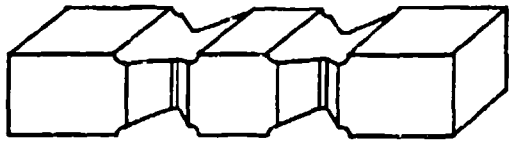

PERSPECTIVE DRAWING

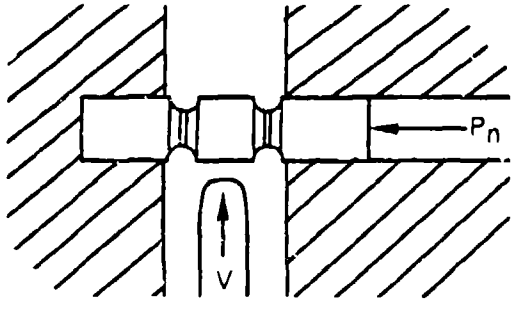

LOADING SCHEMATIC DIAGRAM

Figure 5. Mechanical drawing, perspective drawing and loading schematic diagram of a double linear shear specimen. The specimen is sheared within the two reduced sections at a preselected speed V while an axial load P_n can be superimposed on one end.

fixture may also apply up to 2250 N normal compressive load to the specimen's ends while shear deformation is underway in order to assess the material's response to different stress states. The load-time curve generated by the strain gauge instrumented tup is recorded and stored in the memory of a high speed digital oscilloscope. These dynamic tests were performed at an imposed strain rate in excess of 10^4 s^{-1}. Quasi-static double linear shear tests were performed on a hydraulic tension/compression test machine at an imposed strain rate of 10^{-3} s^{-1}.

Shear stress-strain curves were generated from the load-displacement curves for the low strain rate tests and from the oscilloscope voltage-time records for the high strain rate tests. Stresses were determined using calibrated constants. In the case of the low strain rate tests, shear strains were calculated from displacements, assuming uniform strain, and verified with the instability strains extracted from the specimens' strain profiles. In the case of the high strain rate tests, shear strains were determined from the instability strains extracted from the specimens' strain profiles. It was assumed that the instability strain occurred at maximum load. A typical shear stress-strain curve generated from one of these tests is presented in Figure 6. This curve represents data from the material normalized at 1095°C, austenitized at 845°C, and tempered at 200°C resulting in a hardness of R_c 50.

To determine precise strain profiles, four longitudinal scribe marks were drawn onto the gauge sections of each specimen before testing. After testing, shear strain as a function of the position along the specimen axis was calculated from the local angle of the scribe lines relative to the specimen centerline. This was accomplished by measuring the angle (θ) the scribe line made in a toolmaker's microscope and converting to shear strain (γ) through the simple relation: $\gamma = \tan \theta$.

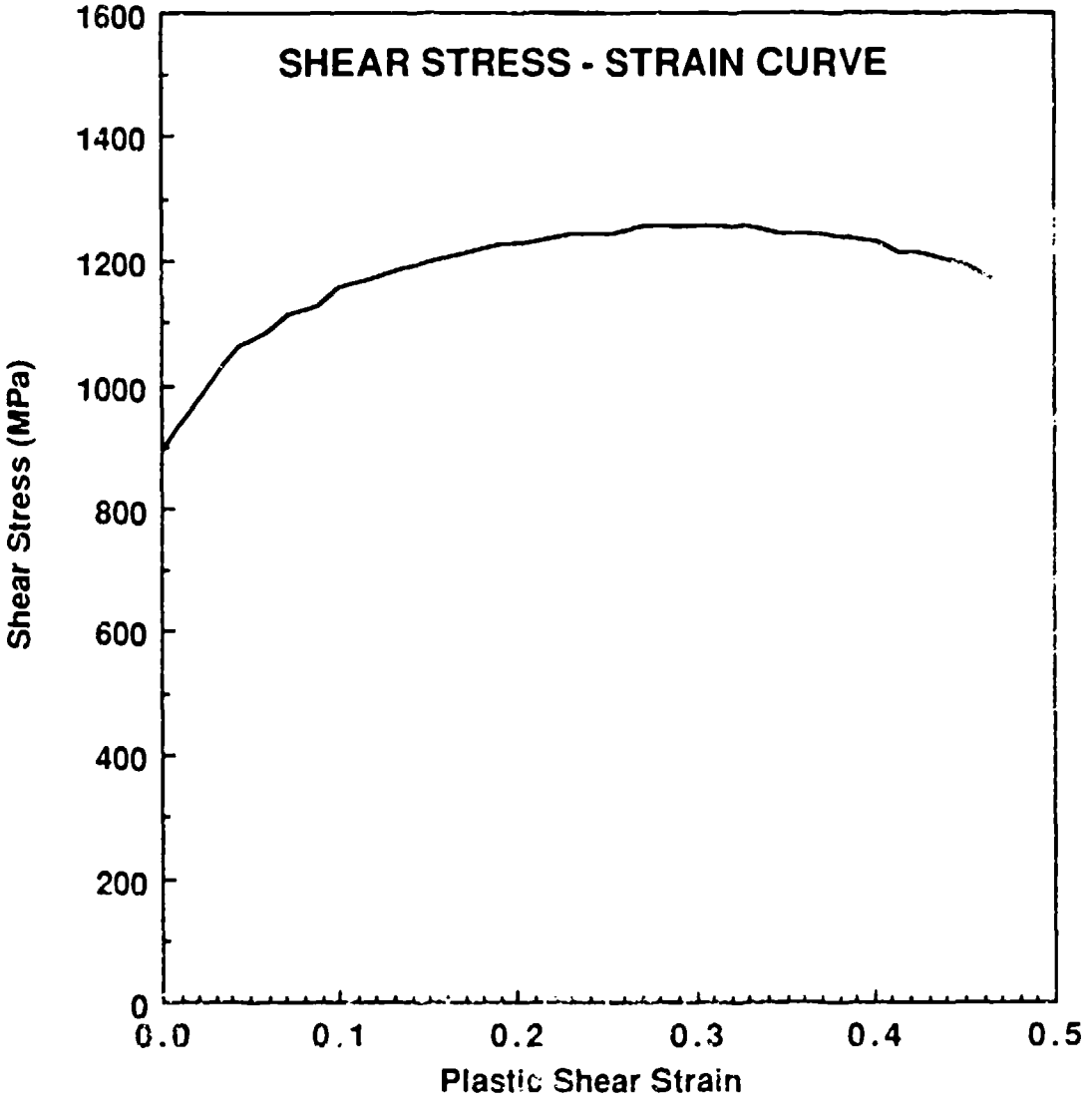

Figure 6. Plastic shear stress-strain curve obtained from a quasi-static linear shear test of VAR 4340 steel normalized at 1095°C, austenitized at 845°C and tempered at 200°C. Shear strain at maximum stress is 33 percent.

Dynamic tests were run to failure, while the quasi-static tests were generally run until sufficient flow localization had occurred to produce a load drop of approximately ten percent.

A typical strain profile obtained from a gauge section of a linear shear specimen tested quasi-statically is presented in Figure 7. This profile is from the same test specimen the shear stress-strain curve was generated from (see Figure 6). Intense strain localization is found adjacent to the gauge section walls. This is consistent with both a hydrocode computer simulation of simple shear of a rectangular body [10] and a finite element stress analysis by Tracey and Perrone [48] of the double linear shear specimen geometry and loading. Note that the shear stain plateau (henceforth defined as the macroscopic shear instability strain) on the strain profile in Figure 7 corresponds with the shear strain at peak stress on the stress-strain curve in Figure 6.

Fracture Toughness Testing

The general test procedures to determine mode I as well as mode II fracture toughness (K_{Ic} and K_{IIc}) are presented in this section. The K_{Ic} tests were performed on standard slow-bend type specimens the K_{IIc} tests were performed using a non-ASTM standardized specimen and test procedure. These tests will be described in more detail following the K_{Ic} test description.

Mode I (Tension) Fracture Toughness Testing

A standard fracture toughness slow-bend specimen as described in ASTM E399-83 [51] was used to determine the critical mode I stress intensity factor (K_{Ic}). The specimen thickness (B) was 10.31 mm, while the specimen depth (W) was 25.45 mm. The crack was formed by fatigue cracking a machined notch to a crack depth a ranging from 13.2

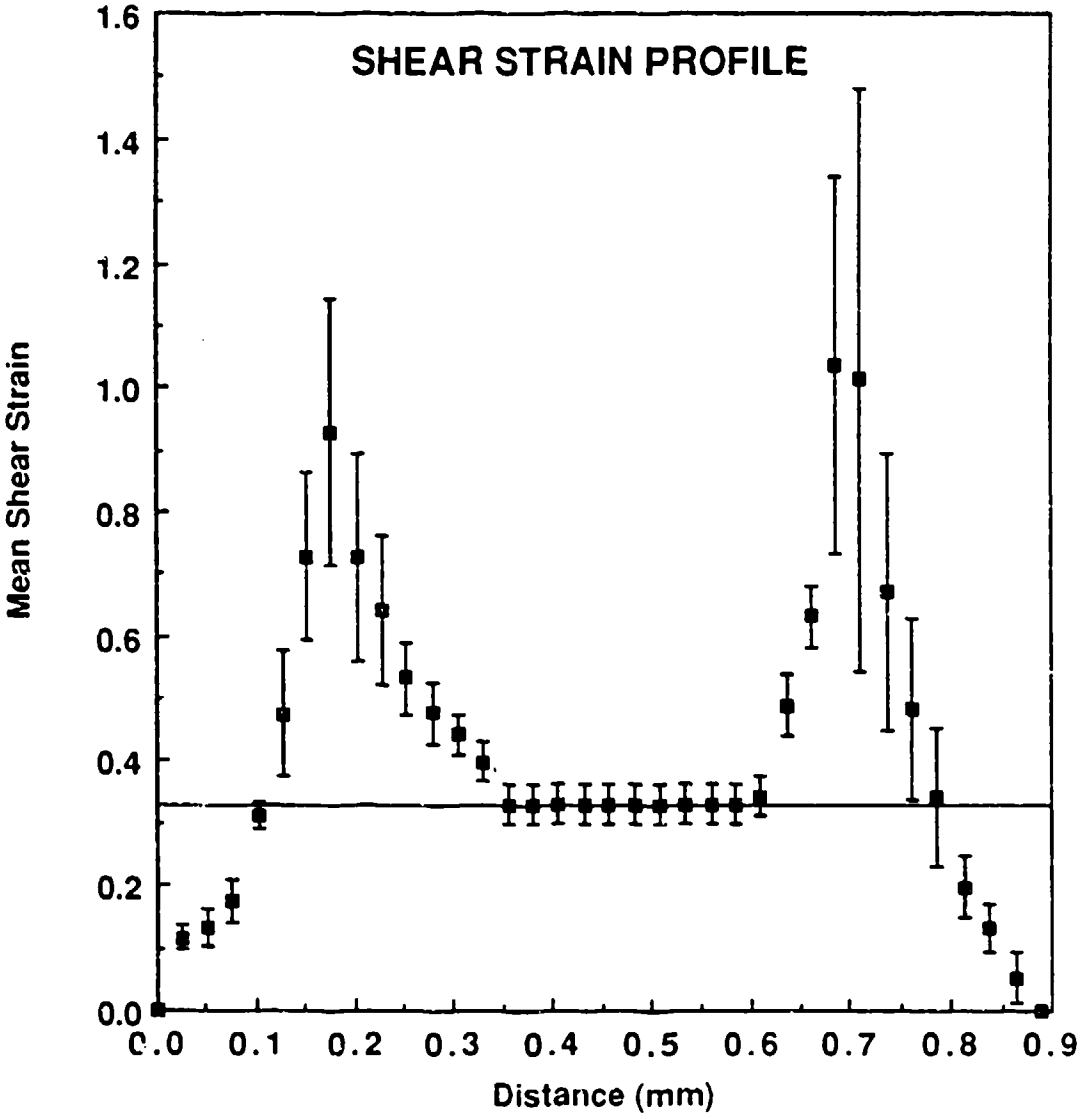

Figure 7. Strain profile obtained from a quasi-static linear shear test of VAR 4340 steel normalized at 1095°C, austenitized at 845°C and tempered at 200°C. The mean plateau strain, defined as the macroscopic instability strain, is 33 percent.

mm to 14.2 mm. The ratio a/W fell within the range of $0.45 < a/W < 0.55$ required by ASTM E399 [51]. Fatigue precracking was conducted at the lowest practical stress level (<20 % of the yield strength) as recommended by Brown and Srawley [52].

The specimens were loaded at 3.8 mm min^{-1} resulting in an average increase of stress intensity of 60.5 $MPa\sqrt{m}$ min^{-1} (33 to 165 is allowable). All specimens were fractured in a stress intensity rate range of 34 to 85 $MPa\sqrt{m}$ min^{-1}. The crack length was measured to the nearest 0.5% at the center of the crack front and midway between the center and the end of the crack front on each side. The average of the three measurements was used as the crack length. The crack length of either surface was within 10% of the average crack length as required by ASTM E399 [51]. The conditional load (P_Q) was determined using either the 5% secant offset load (P_5) or the maximum load (P_{max}) of the load-displacement curve, whichever occurred first. All specimens tested met the critical size (a, B, W) requirements for plane strain conditions along with the requirement that P_{max}/P_Q ratio be greater than 1.10 P_5 [51]. Consequently, these tests were valid fracture toughness tests, *i.e.* $K_Q = K_{Ic}$.

Mode II (Shear) Fracture Toughness Testing

A novel mode II fatigue crack growth and fracture toughness specimen has been developed by Buzzard *et al.* [53], which was named the LeRC (NASA Lewis Research Center) Mode II Specimen. The attributes of this particular specimen are that it contains one single-ended notch and that the mode I component is extremely small.

Prior to the development of the LeRC specimen, several other mode II test specimens had been developed, but had limited success in determining K_{IIC}. A vee-notched specimen type designed by Iosipescu [54] has been used by several investigators, but this specimen does not exhibit the classical mode II stress pattern, *i.e.*, concentric

semiellipses centered at the crack tip when tested with photoelastic material [53]. Another mode II specimen was developed by Richard [55], which produced a very good mode II photoelastic stress pattern [53]. However, at high loads this specimen fails at the grip holes, while at moderate loads the crack propagates from the crack tip toward the tensile-loaded leg of the specimen at an angle of about 70° [53]. A double-notched mode II specimen developed by Jones and Chisholm [56] also exhibited a very good mode II pattern at both crack tips, but at low loads, cracks ran at approximately 70° to the machined notches [53]. Although the double notched specimen exhibited proper behavior, a single-notch specimen with simpler fabrication and testing consideration was preferred. Various other specimen designs were investigated with poor results [53]. The principal failure mode of most of these specimens was a 70° crack moving into the tensile loaded side of the notch, indicative of a mode I failure. These specimen designs are more fully described in the literature [57-59].

The NASA Mode II LeRC specimen design (Figure 8) was tested using photoelastic material which showed a symmetrical mode II pattern at the crack tip [53]. Aluminum specimens tested failed with the fracture path at or near 0° to the machined notch [53]. An experimental compliance calibration was performed on the specimen to provide displacement and stress intensity coefficients over crack length to specimen width ratios (a/W) of 0.5 to 0.9 [60]. Based on the data for larger specimens by Buzzard [60], a fourth order polynomial relating the stress intensity coefficients $f(a/W)$ to the a/W ratio was derived for this study

$$f(a/W) = -2.367 + 20.7725(a/W) - 36.853(a/W)^2 + 23.7226(a/W)^3 - 0.2010(a/W)^4.$$

The above equation and the experimental data fall within a 5% or less error band (Figure 9). The calculated stress intensity coefficient may then be used to determine the mode II

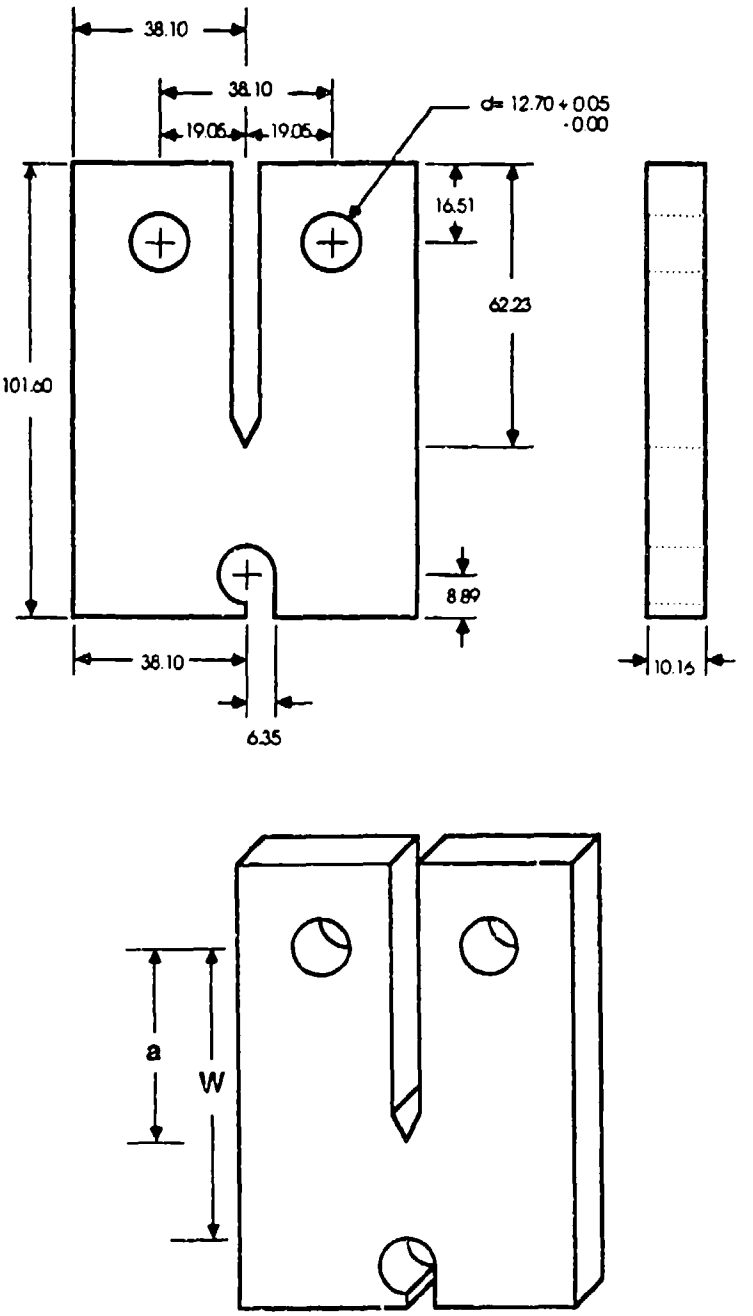

45.72mm < a < 62.87mm

W = 69.85 mm

Figure 8. NASA LeRC mode II (shear) fracture toughness specimen. All dimensions in mm.

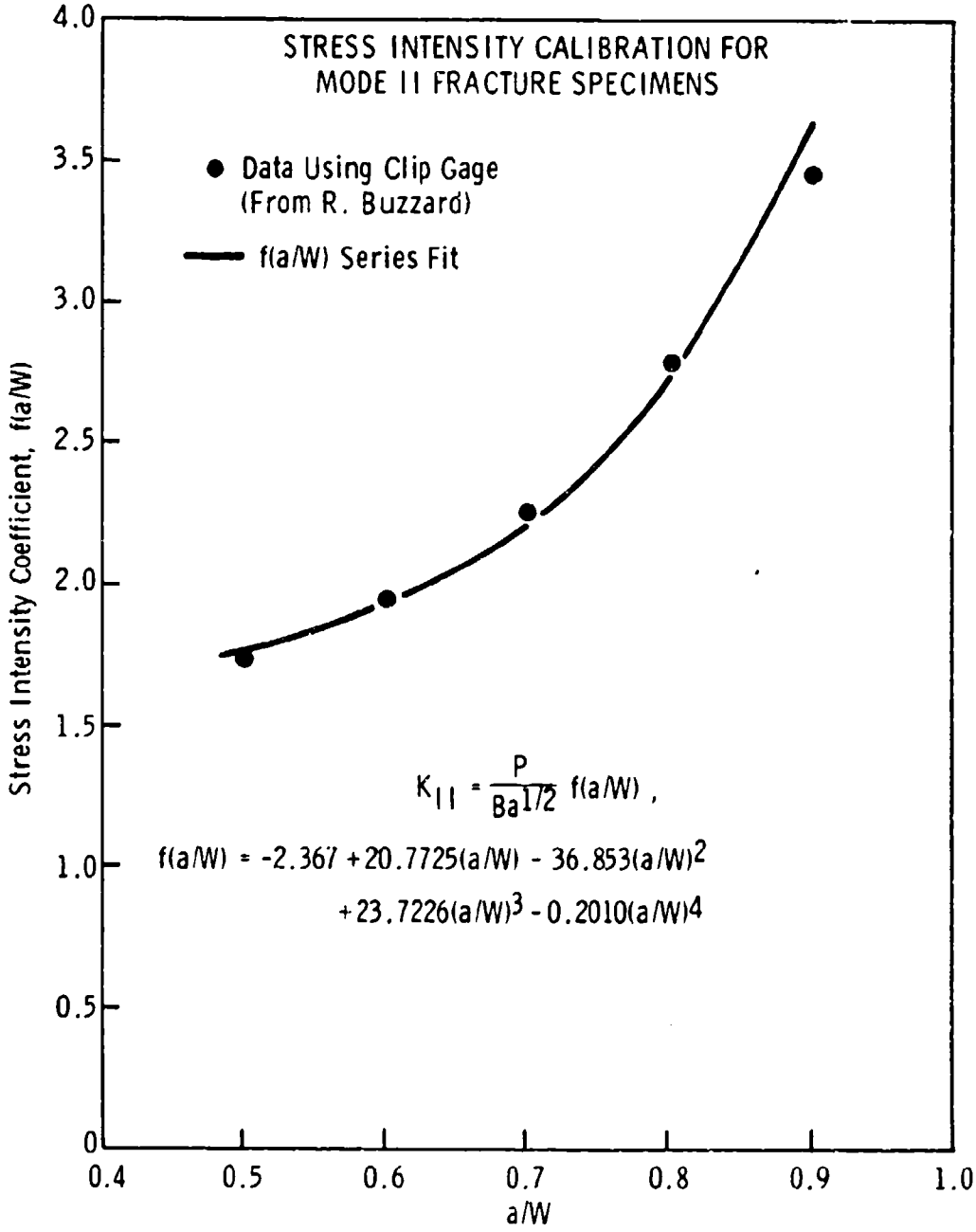

Figure 9. Fourth order polynomial fit of the stress intensity coefficients and a/W for mode II fracture toughness specimen. Based on data for larger specimens obtained by Buzzard [60].

stress intensity factor (K_{II}) in the usual way

$$K_{II} = \frac{P}{B\sqrt{a}} f(a/W).$$

The critical mode II stress intensity factor K_{IIc} was calculated by inserting the conditional load (P_Q) into the above equation. P_Q was determined using either the 5% secant offset load (P_5) or the maximum load (P_{max}) of the load-displacement curve, which ever occurred first. As there are no ASTM guidelines in existence for mode II fracture toughness testing, an assessment of the specimen size requirements could not be made. However, the specimens were machined to the dimensions of the larger specimen set forth by Buzzard *et al.* [53,60]. In addition, the specimen thickness was maximized (B = 10.16 mm) so that the fracture load was just below the maximum capacity of the servohydraulic test machine. The specimen depth (W) was 69.85 mm.

The crack was formed by fatigue cracking (in tension) a machined notch to a depth ranging from 45.72 to 62.87 mm. Initially, the precracking was attempted in shear, but the crack propagated from the crack tip toward the tensile-loaded leg of the specimen at an angle of about 70° to the notch. In order to avoid this problem, fatigue cracking was performed in tension, which was conducted at the lowest practical stress level (< 20% of the yield strength) to avoid influencing the fracture toughness test [52]. In addition, precracking was performed in 'stroke control' which provides a decreasing load with increasing crack opening displacement and crack length.

During the actual fracture test the specimens were loaded very slowly resulting in an average rate of increase of stress intensity of 45 $MPa\sqrt{m}$ min^{-1}. All specimens were fractured in a stress intensity rate range of 37 to 52 $MPa\sqrt{m}$ min^{-1}. The crack length was measured to the nearest 0.5% at the center of the crack front and midway between the center and the end of the crack front on each side. The average of the three measurements

was used as the crack length. The crack length of either surface was within 10% of the average crack length. In addition, the P_{max}/P_Q ratios were greater than 1.10 P_5. The specimen thickness was greater than 5.5 times the calculated plane stress plastic zone size, indicative of a nearly total plane strain condition. It cannot be said that these tests were valid K_{IIc} tests since no standard exists for this type of testing. However, with the possible exception of specimen size requirements, these tests met the validity criteria for mode I fracture toughness tests as defined by ASTM E399 [51].

QUANTITATIVE METALLOGRAPHY RESULTS

The second-phase particle type, size, and distribution were determined as described in the Experimental Procedure section of this study. Table II presents the size and distribution data for each heat treatment. The normalizing temperature varied between 845°C and 1095°C, and two tempering temperatures were used: 200°C and 650°C. One specimen received a 24 hour liquid nitrogen temperature (77°K) refrigeration treatment after normalizing.

The particle count per unit area (N_A) and per unit volume (N_V) along with the geometric mean particle radius (R), volume fraction (f_v), and interparticle spacing (λ) are given for each specimen in Table II. An important dimensionless ratio of the interparticle spacing to the geometric mean radius (λ/R) is also included in Table II.

TABLE II. SECOND-PHASE PARTICLE SIZE AND DISTRIBUTION

Normalizing Temp. (°C)	Tempering Temp. (°C)	Number Per Area, N_A(mm^{-2})	Mean Radius R (nm)	Volume Fraction f_v	Number/ Volume, N_V (mm^{-3})	Interparticle Spacing λ (nm)	λ/R Ratio
845	200	3.26	38.8	0.015	56.2	261	6.73
925	200	3.71	26.6	0.008	97.5	217	8.16
1010	200	4.11	40.5	0.021	70.8	242	5.98
1095	200	8.45	25.2	0.017	178.5	178	7.06
845†	650	11.29	50.8	0.092	159.8	184	3.6
845‡	650	11.36	52.0	0.096	163.0	183	3.5

† Data from SEM of polished and lightly etched surface.
‡ Data from TEM of surface replica.

Two different imaging techniques were used to measure one of the specimen's particles, namely SEM of the polished and lightly etched surface and TEM of two-stage surface replicas. Figures 10-14 illustrate typical electron micrographs of extraction replicas

Figure 10. TEM photomicrograph of an extraction replica of VAR 4340 steel normalized at 845°C, austenitized at 845°C and tempered at 200°C.

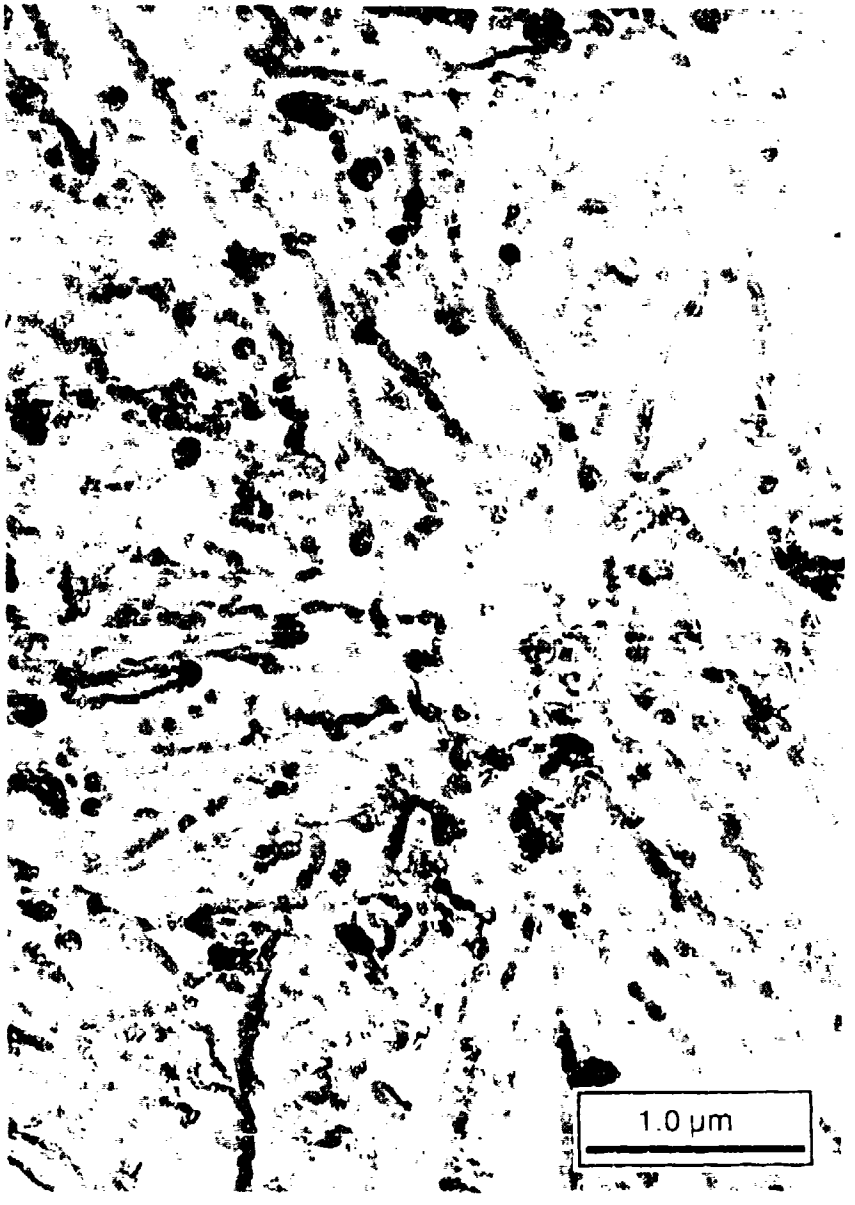

Figure 11. TEM photomicrograph of an extraction replica of VAR 4340 steel normalized at 925°C, austenitized at 845°C and tempered at 200°C.

Figure 12. TEM photomicrograph of an extraction replica of VAR 4340 steel normalized at 1010°C, austenitized at 845°C and tempered at 200°C.

Figure 13. TEM photomicrograph of an extraction replica of VAR 4340 steel normalized at 1095°C, austenitized at 845°C and tempered at 200°C.

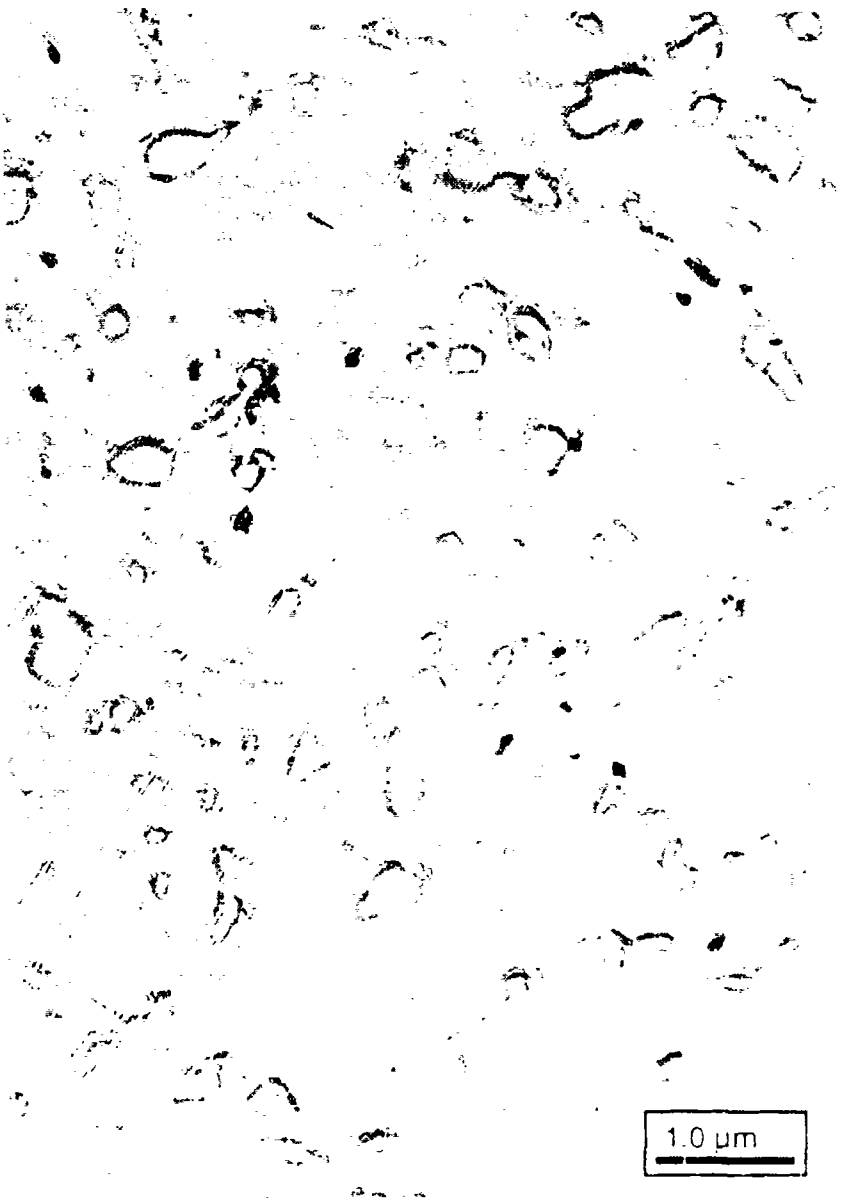

Figure 14. TEM photomicrograph of an extraction replica of VAR 4340 steel normalized at 845°C, austenitized at 845°C and tempered at 650°C.

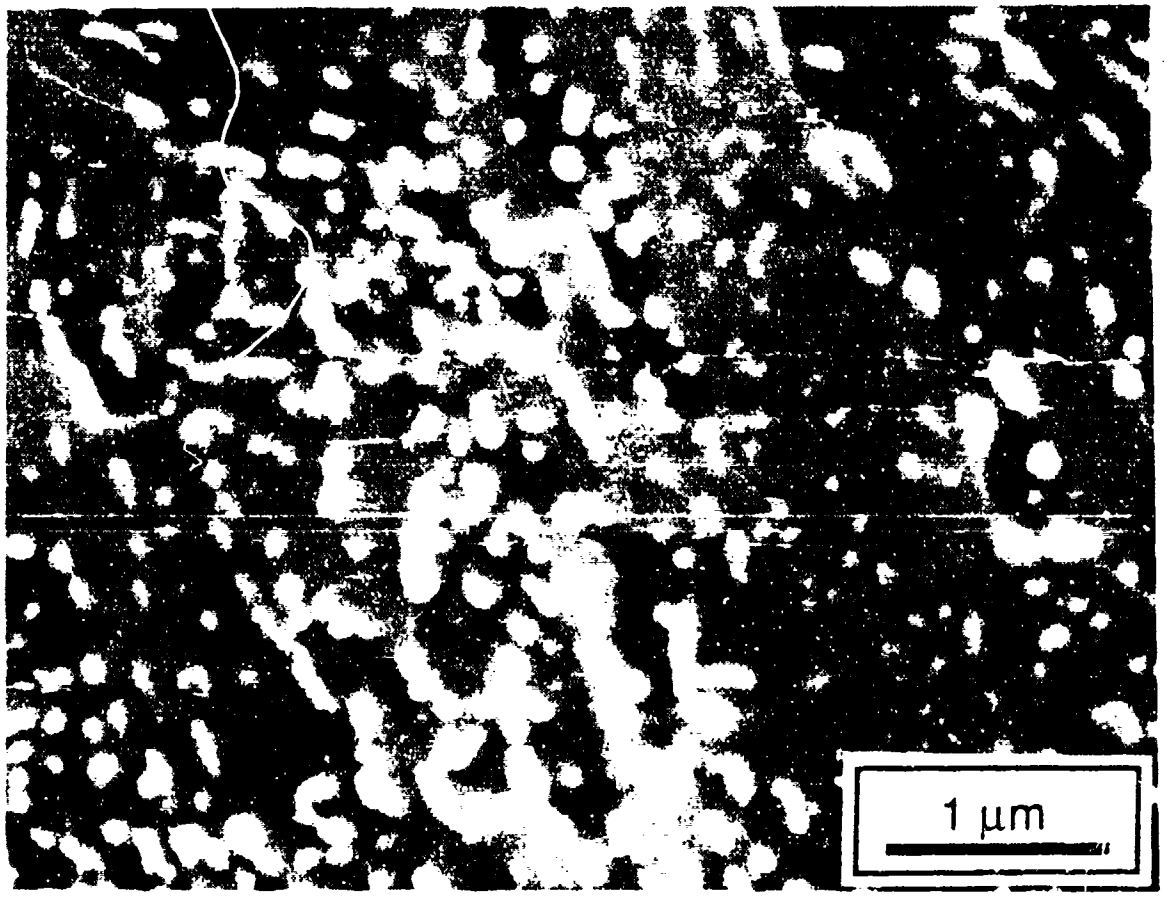

Figure 15. SEM photomicrograph of polished and etched surface of VAR 4340 steel normalized at 845°C, austenitized at 845°C and tempered at 650°C.

taken from each specimen. Figure 15 is an SEM photomicrograph of the specimen tempered at 650°C for comparative purposes (see Figure 14). Log-normal distributions of the particle diameters for each specimen are presented in Figures 16-20. It was observed that a bimodal distribution prevails for all specimens.

Results of the statistical analysis of the geometric mean particle radius data as outlined in detail in the Experimental Procedure section of this study are presented in Table III. Error bands (±) used for the geometric mean particle radius were taken from the 95% confidence limit (95%CL). The percent relative accuracies (%RA) less than or equal to 12 for the geometric mean particle radii are quite satisfactory for this analysis.

TABLE III. STATISTICAL ANALYSIS OF MEAN PARTICLE RADII

Normalizing Temp. (°C)	Tempering Temp. (°C)	Mean Radius, R (nm)	Standard Deviation s	Number, N -	95% Confidence Level	Percent Relative Accuracy
845	200	38.8	20.5	79	4.6	10.6
925	200	26.6	12.5	88	2.7	9.5
1010	200	40.5	19.0	128	3.4	7.8
1095	200	25.2	14.0	80	3.2	12.0
845	650	50.8	42.0	211	5.8	10.9

The error bands were carried through in the calculation of the interparticle spacing (λ) and the λ/R ratio as presented in Table IV. Figure 21 presents the geometric mean particle radius results as a function of the normalizing temperature (all given the same post normalizing heat treatment). Note the minimum at 925°C and the maximum at 1010°C. As will be demonstrated in the following section, the shear properties are influenced by these differences.

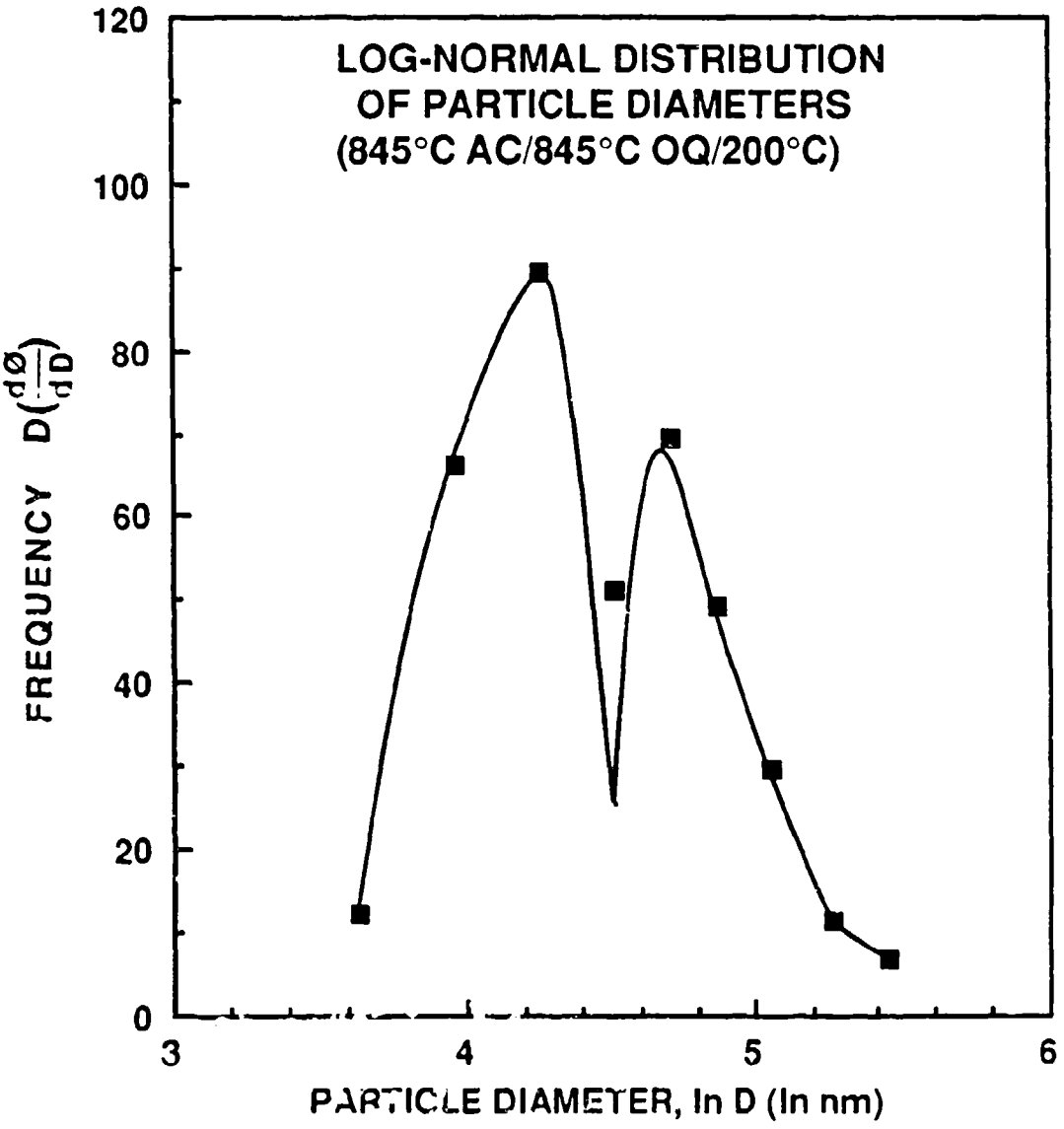

Figure 16. Log-normal distribution of the particle diameters from VAR 4340 steel normalized at 845°C, austenitized at 845°C and tempered at 200°C. The data is plotted as a relative percentage frequency distribution using a natural logarithmic scale for particle diameter.

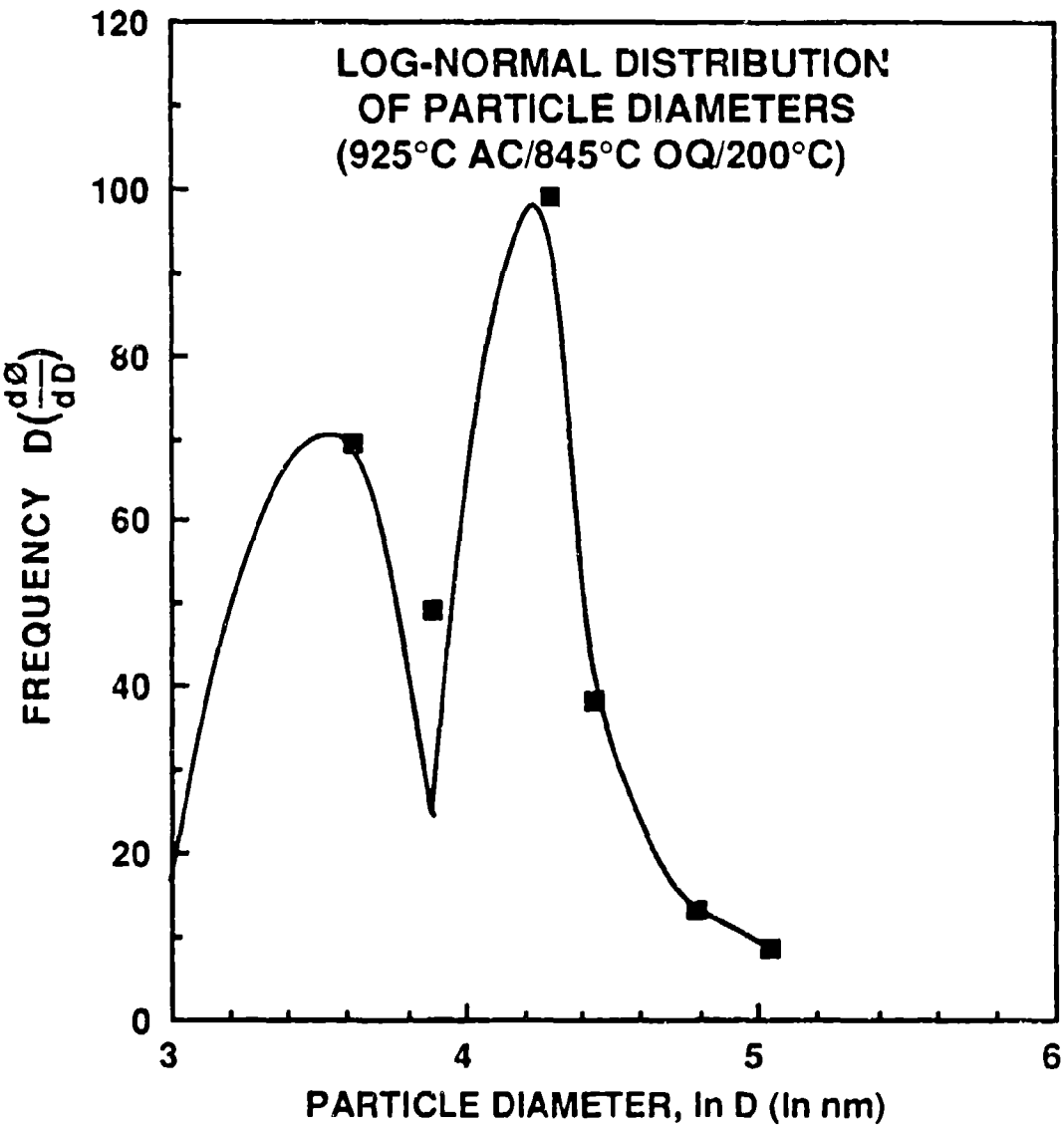

Figure 17. Log-normal distribution of the particle diameters from VAR 4340 steel normalized at 925°C, austenitized at 845°C and tempered at 200°C. The data is plotted as a relative percentage frequency distribution using a natural logarithmic scale for particle diameter.

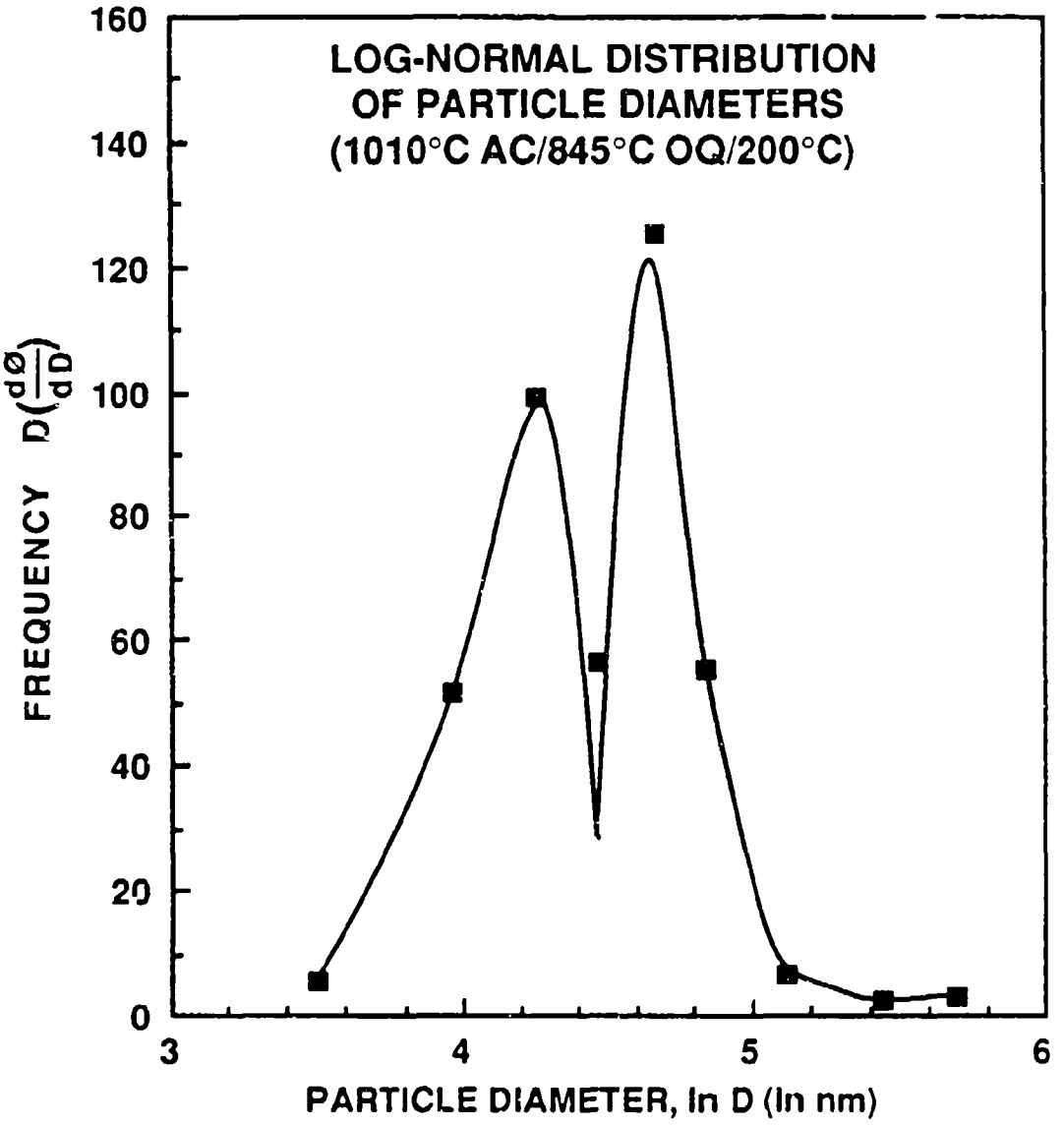

Figure 18. Log-normal distribution of the particle diameters from VAR 4340 steel normalized at 1010°C, austenitized at 845°C and tempered at 200°C. The data is plotted as a relative percentage frequency distribution using a natural logarithmic scale for particle diameter.

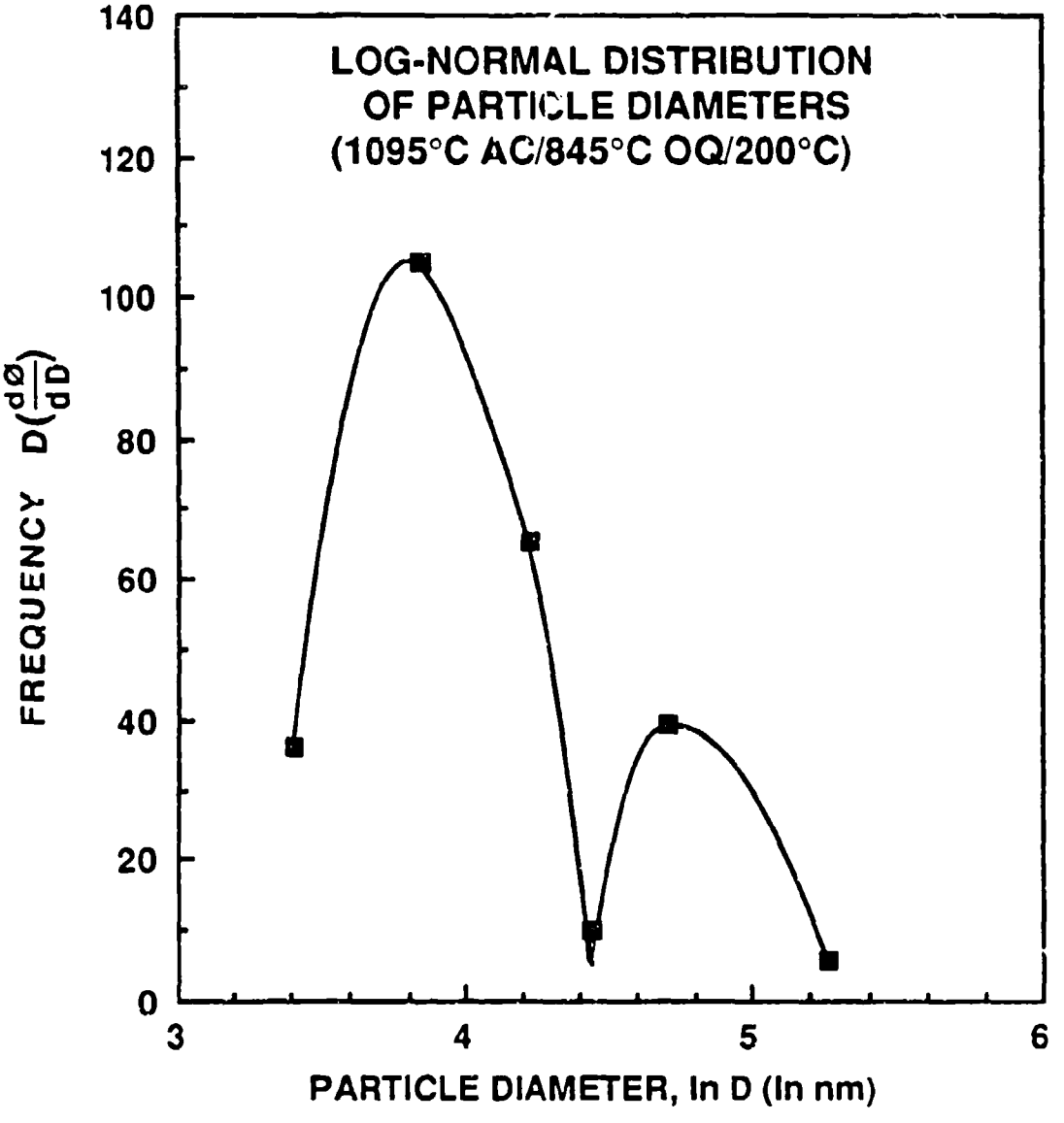

Figure 19. Log-normal distribution of the particle diameters from VAR 4340 steel normalized at 1095°C, austenitized at 845°C and tempered at 200°C. The data is plotted as a relative percentage frequency distribution using a natural logarithmic scale for particle diameter.

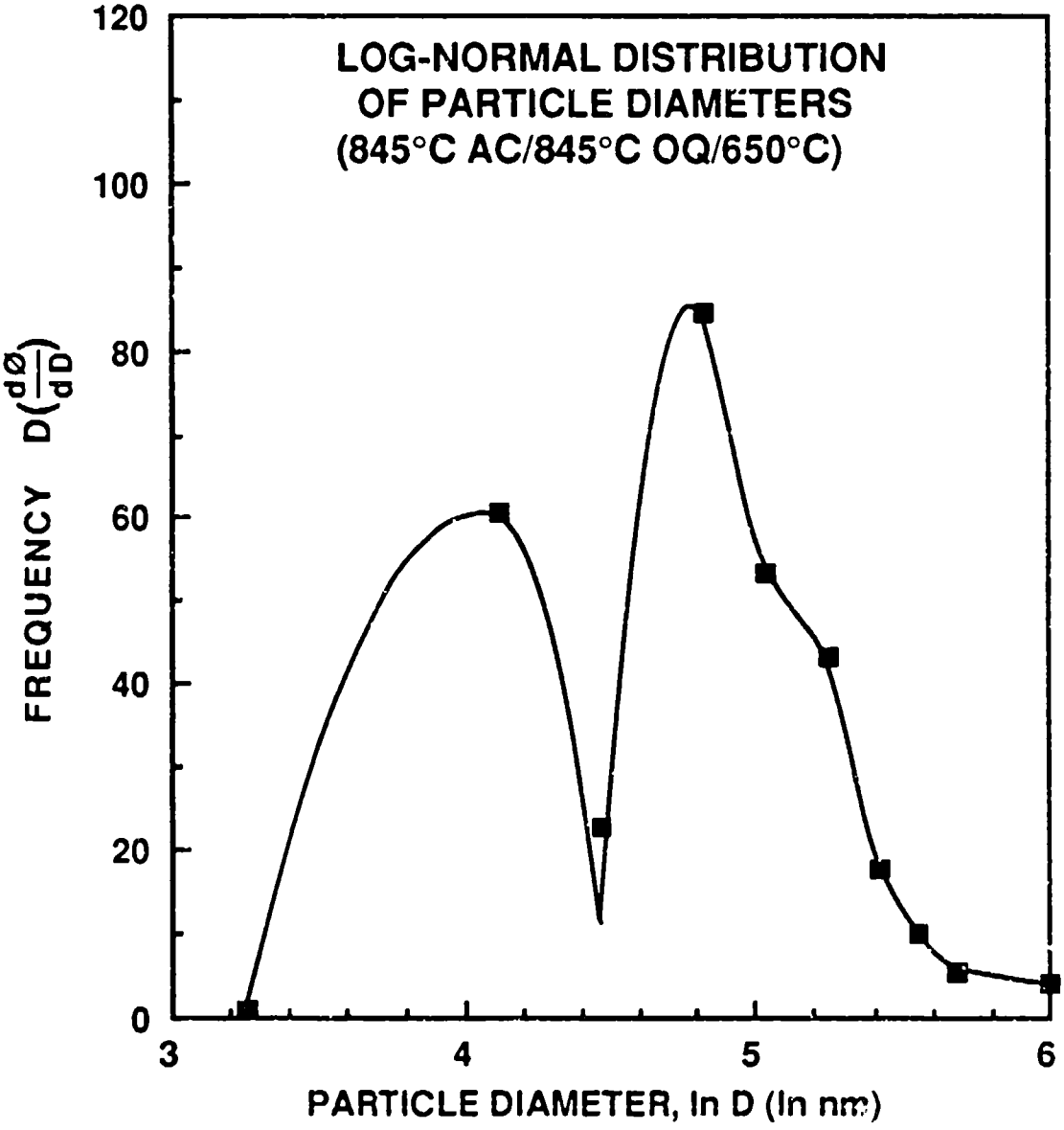

Figure 20. Log-normal distribution of the particle diameters from VAR 4340 steel normalized at 845°C, austenitized at 845°C and tempered at 650°C. The data is plotted as a relative percentage frequency distribution using a natural logarithmic scale for particle diameter.

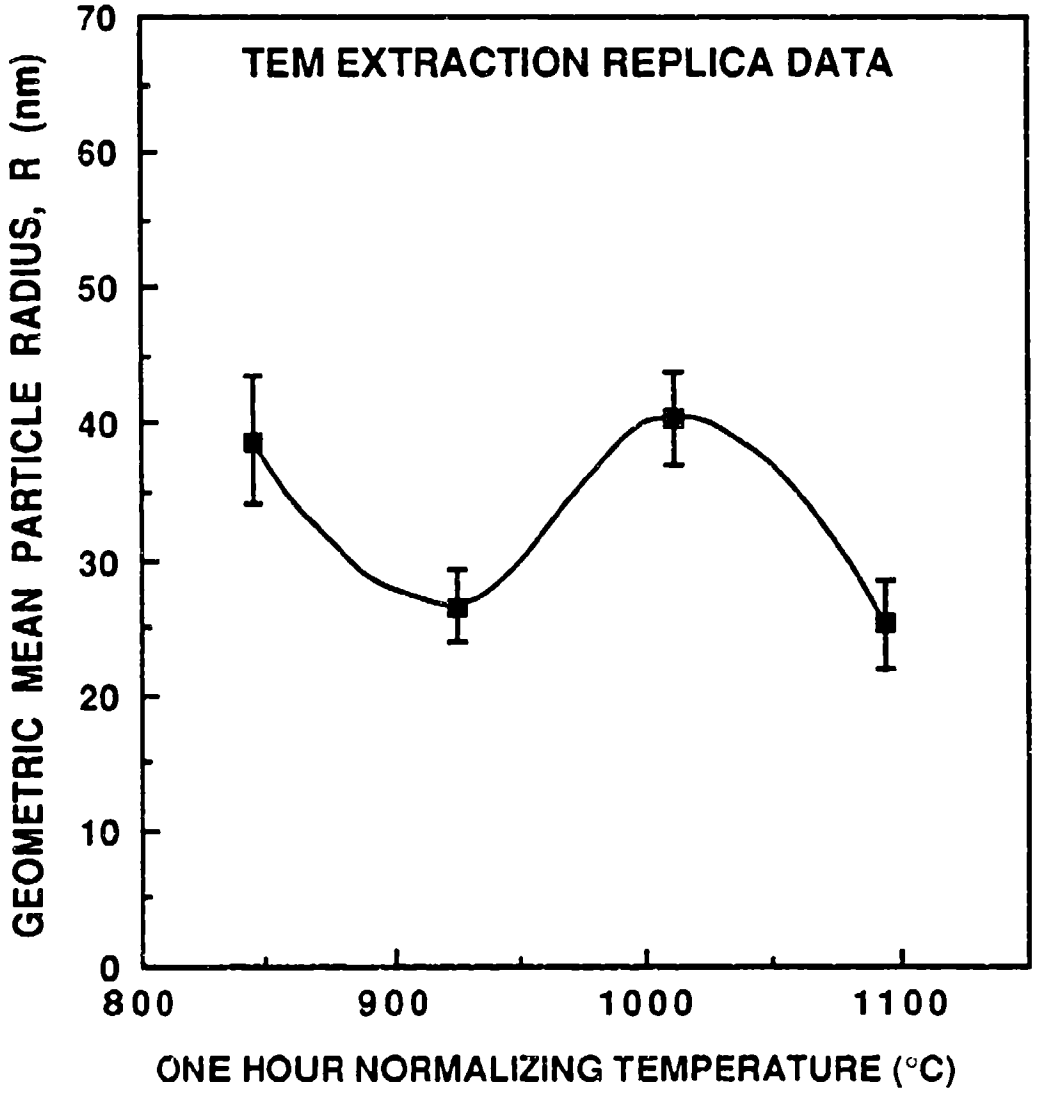

Figure 21. Geometric mean particle radius results as a function of the normalizing temperature.

TABLE IV. ERROR BANDS FOR PARTICLE SIZE AND DISTRIBUTION

Normalizing Temp. (°C)	Tempering Temp. (°C)	Mean Radius, R (nm)	Volume Fraction, f_v	Interparticle Spacing, λ(nm)	λ/R Ratio
845	200	38.8 ± 4.6	0.015 ± 0.005	261±10	6.7±0.4
925	200	26.6 ± 2.7	0.008 ± 0.001	217±7	8.2±0.4
1010	200	40.5 ± 3.4	0.021 ± 0.004	242±7	6.0±0.3
1095	200	25.2 ± 3.2	0.017 ± 0.006	178±11	7.1±0.6
845	650	50.8 ± 5.8	0.092 ± 0.026	183±6	3.6±0.3

The material which was normalized at 1010°C exhibited large, interconnected aluminum nitride particles following along the prior austenite grain boundaries. Surface replicas revealed these AlN particles very nicely (Figure 22). The presence of aluminum nitride particles was verified using a windowless energy dispersive x-ray spectrometer on electropolished specimens in the SEM. The particles actually contained some oxygen, and therefore are more precisely aluminum oxy-nitrides.

The structure of the material tempered at 650°C consists of spherical Fe_3C carbide particles uniformly dispersed in a ferrite matrix (see Figure 15). The high ductility of such a microstructure is directly related to the continuous ductile ferrite phase. A comparison was made between the volume fraction (f_v) of particles measured in this specimen and f_v calculated through stoichiometry. Assuming all the carbon, initially interstitial atoms within the martensitic matrix, goes into the formation of cementite particles when tempered at 650°C for two hours, then f_v can be calculated from stoichiometry and chemical composition. Since the densities of cementite and ferrite are nearly equivalent (ρ_{Fe_3C}/ρ_α = 0.98), it can be assumed that the weight percent cementite is equal to the volume percent cementite (6% for this steel). By adding the volume fraction of second phase particles initially present before tempering (1.5% for the specimen having the same normalizing and austenitizing treatments), a total volume fraction of second-phase particles is determined to be 7.5 ± 0.5%. This result is within experimental error of the measured volume fraction

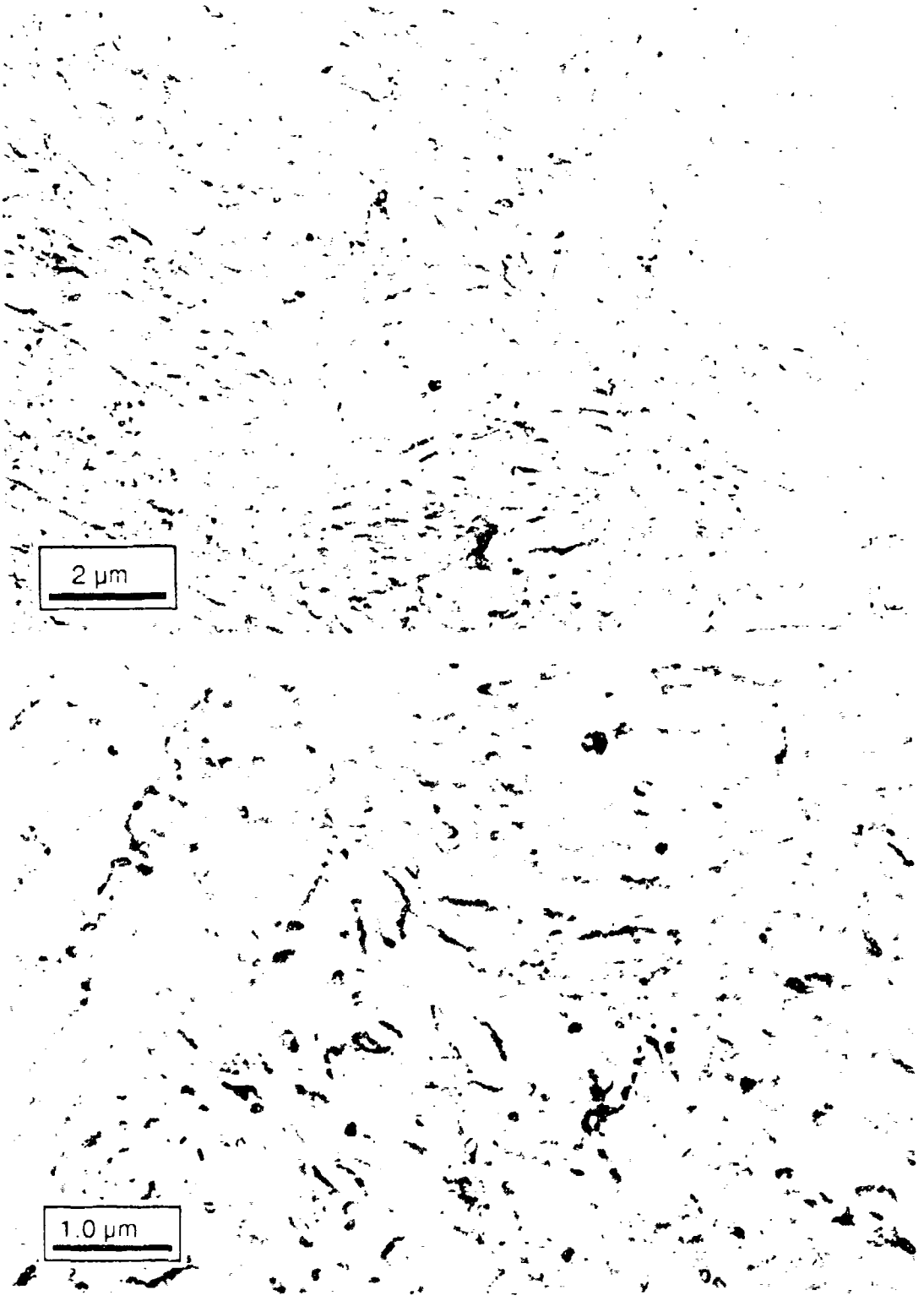

Figure 22. A TEM photomicrograph of a continuous string of aluminum nitride particles observed in the prior austenite grain boundaries. This steel was normalized at 1010°C, the approximate grain coarsening temperature.

for this specimen of 9.2 ± 2.6%. Therefore, based on this comparison and the statistical analysis, the author believes that within experimental uncertainty, the particle size and distribution data are accurate.

The types of second phase particles have been investigated through energy dispersive x-ray (EDX) spectroscopy of individual particles contained within the extraction replicas. Several particles of all sizes were analyzed for each specimen. An energy spectrum was collected for each particle, and numerical atomic percent data were obtained. Elements with atomic numbers less than 11 (Na) could not be detected with the EDX spectrometer due to the fact that their low energy x-rays cannot penetrate the beryllium window. Therefore, three very important elements (carbon, nitrogen, and oxygen) went undetected and are absent from the tabulated data in this study. Table V lists the average uncorrected composition of the particles surveyed for each of the specimens. The relative percent has been normalized to create a 100% total. Consequently, these relative amounts do not reflect the quantity of the elements with atomic numbers less than 11. Particle to particle chemical composition varied somewhat. The most significant observation that was made, was the absence of aluminum in the smaller particles at 1010°C and above.

TABLE V. AVERAGE PARTICLE CHEMICAL COMPOSITIONS (Relative Percent)*

Normalizing Temp. (°C)	Al	Si	P	S	Ca	Fe	Ni
845	8.0	31.2	-	14.8	21.4	23.4	1.2
925	5.2	11.9	3.4	4.7	13.4	60.2	1.2
1010 †	83.1	4.0	-	2.0	4.0	6.8	0.1
1010 ‡	-	53.8	7.2	-	16.3	21.6	1.1
1095	-	37.7	3.2	9.0	16.0	31.3	2.8

* Does not include elements with atomic numbers less than 11.
† Large particles @ 1010°C
‡Small particles @ 1010°C

Iron and nickel are alloying elements which are obvious particle constituents. Calcium, sulfur and phosphorous are undesirable impurities present in all steels in varying quantities. Generally, the lower the impurity content, the better the mechanical properties and the higher the cost. Silicon and aluminum are introduced as deoxidizing agents during the melting practice. In addition to forming oxides which become part of the slag, minute quantities of these elements are dissolved into the melt, which have the desirable function of controlling the austenite grain size. The calcium, aluminum, and silicon generally combine with oxygen to form calcium alumino-silicates ($CaO\text{-}Al_2O_3\text{-}SiO_2$) which appears to be concentrated in the particles observed in this analysis. Wüstite (FeO) is also frequently observed in these steels, and is assumed to be a constituent of the particles containing relatively high concentrations of iron (see Table V).

In addition to forming aluminum oxide, aluminum also has a high affinity for nitrogen creating aluminum nitride (AlN) particles. These particles help restrain austenite grain growth below about 1000°C. Abrupt coarsening occurs in these fine grained steels above this temperature due to the coarsening and dissolution of AlN particles which is sometimes referred to as "secondary recrystallization." On the contrary, coarse grained steels are deoxidized with silicon, a practice which does not produce particle dispersions effective in inhibiting austenite grain growth.

Gladman [61] developed a relationship between aluminum content and the grain coarsening temperature in low carbon steels. The aluminum content of the steel employed in this investigation is 0.031 wt.% (see Table I) and a nitrogen content of 0.005 wt.%. Using Figure 23 [61] and the aluminum content, 1010°C is found to be the approximate grain coarsening temperature for this heat of steel. The reaction Al + N = AlN is reversible and at high temperatures some of the AlN particles dissolve which permits grain coarsening.

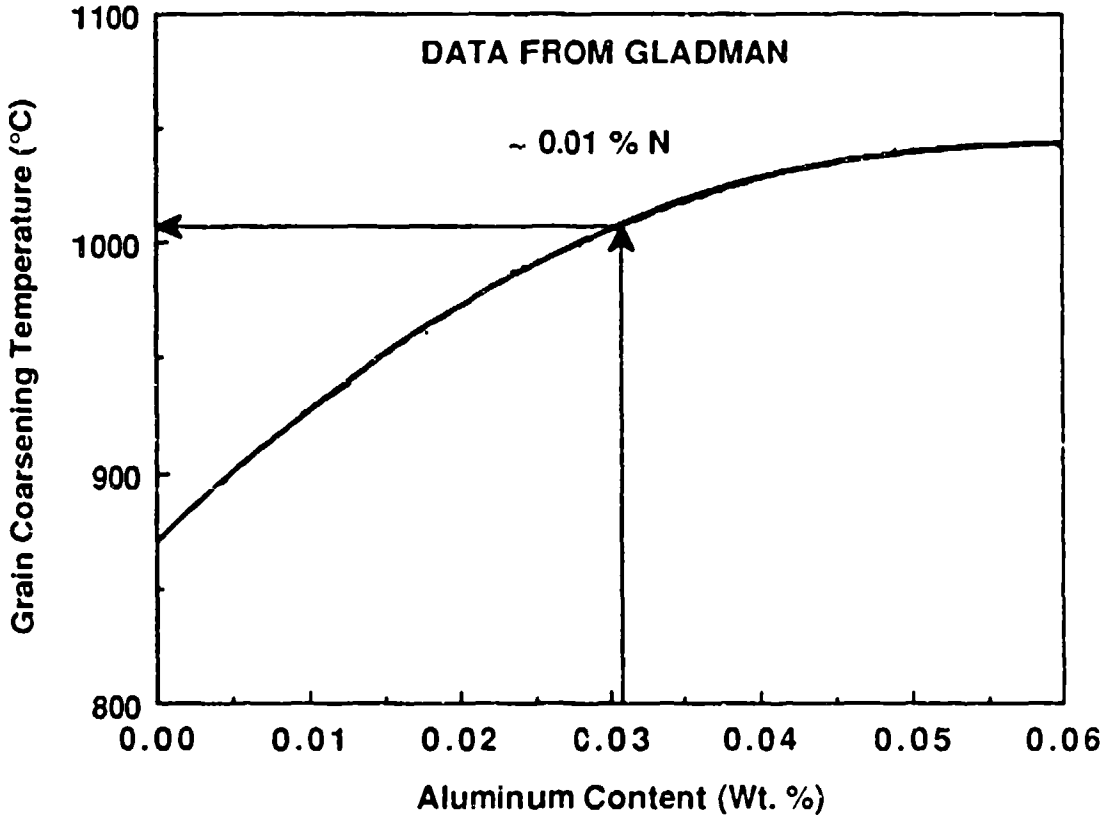

Figure 23. Grain coarsening or secondary recrystallization temperature as a function of aluminum content in low carbon steels. Data from Gladman [61]. Vertical arrow indicates the aluminum content in the steel employed in the present study. The horizontal arrow indicates the grain coarsening temperature.

An austenite grain coarsening study was performed in order to determine the grain growth response to temperature. The prior austenite grain size was determined using the method outlined in ASTM E112-63 [62] for one hour solutionizing treatments over a temperature range from 800°C to 1200°C at 25°C increments. Figure 24 illustrates this relationship between austenite grain size and temperature for both VAR and air melted (AM) 4340 steel. The AM 4340 data points were added for comparison purposes. Since AM steel contains somewhat more impurities than VAR steels, by the nature of the refining practice, the AM 4340 steel exhibited less grain growth over the temperature range. A note of interest; this is the same heat of steel used in the recent study of microvoid nucleation by Cowie *et al.* [2].

A significant observation may be made concerning Figure 24, that is a change in slope occurs between 1000°C and 1050°C for the VAR 4340 steel. This indicates a change in the grain growth kinetics and therefore suggests a coarsening and dissolution of aluminum nitride particles around this temperature range. Grain growth is more rapid above 1050°C and somewhat slower below 1000°C. Since this particular steel contains both aluminum and silicon particles, the grain growth response can be considered a combination of that which fine grained steels (aluminum deoxidized) and coarse grained steels (silicon deoxidized) experience [63].

Nevertheless, evidence of aluminum particle coarsening in the prior austenite grain boundaries (Figures 21, 22 and Table II), aluminum particle dissolution (Table V), and accelerated grain growth (Figures 23 and 24) were observed at 1010°C. The combination of these results clearly indicates an aluminum nitride particle dissolution and coarsening responsible for grain coarsening above 1010°C. Processing at this temperature, aluminum nitride embrittlement can occur, significantly reducing toughness and ductility.

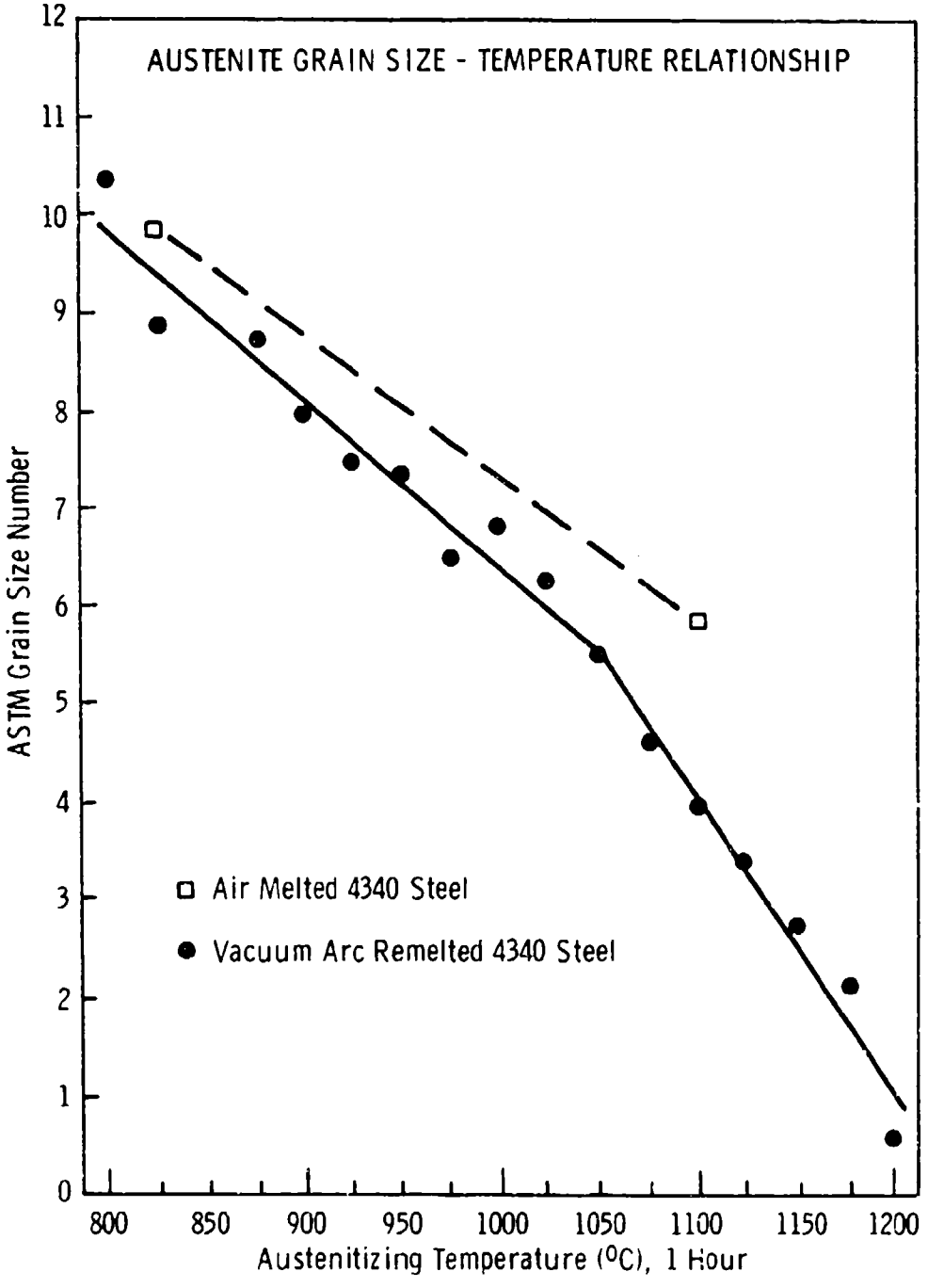

Figure 24. Austenite grain size as a function of temperature for both VAR and AM 4340 steel. The slope change for the VAR steel at approximately 1000°C indicates aluminum nitride dissolution and subsequent grain coarsening.

SHEAR TEST RESULTS

Results are presented for shear test experiments aimed at determining the following effects on shear properties: normalizing temperature, cryogenic treatment, strain rate, and hydrostatic pressure. As was demonstrated previously in Figure 21 and Table II, the normalizing temperature affects the particle size and distribution, and since it was strongly suggested that strain localization in UHS 4340 steel under simple shear loading conditions is controlled at 100 nm scale second-phase particles [2], the effect of normalizing temperature on shear properties was investigated. In addition, differences in amounts of retained austenite may also influence the shear properties. Therefore, the effect of a post-normalizing cryogenic refrigeration treatment on shear strain was studied. The effect of hydrostatic pressure during shear testing was investigated since it was hypothesized that the pressure would delay microvoid nucleation and therefore, postpone strain localization. Verification of the effect of strain rate discussed in the literature [2,10,11] was also performed.

Effect of Normalizing Temperature

A test of the influence of second-phase particles on shear localization can be made by raising the normalizing temperature to dissolve these particles. Gore *et al.* [64] has demonstrated that raising the austenitizing temperature in the same heat of 4340 steel examined in this study, dissolves the second-phase particles from a volume fraction of 0.44% at 870°C to 0.05% at 1200°C. Such a change in the amount of undissolved dispersions can be expected to significantly alter the critical strain for microvoid nucleation softening. This should be most pronounced in Stage I tempered material where the ultrafine ε–carbides precipitated during tempering should not contribute to microvoid nucleation, and the influence of undissolved particles would thus be greatest. An

investigation [64] into the effect of austenitizing temperature in the range of 870°C to 1200°C on the instability strain in the VAR 4340 steel tempered at 200°C has shown a slight monotonic decrease with increasing austenitizing temperature. The effect has been attributed to a combination of crystal-plasticity-based strain softening mechanisms which may be promoted by grain coarsening [64]. As mentioned in the previous section and illustrated in Figure 24, VAR 4340 steel develops significant grain coarsening over the temperature range investigated by Gore *et al.* [64], especially at 1200°C where the volume fraction of second-phase particles is a minute 0.05%.

Since it has been shown that the prior austenite grain size affects the shear instability strain [64], it was proposed that a study of the influence of particle size and distribution on the shear properties be performed at a constant austenite grain size. This was accomplished by varying the normalizing temperature from 845°C to 1100°C and then austenitizing for a short time (15 min) at a single low temperature (845°C). The one hour normalizing treatment determines the size and distribution of the second-phase particles. Although some particles are nucleated at the low temperature austenitizing treatment, the tendency for particle growth is limited by both the short time (15 min) exposure and low austenitizing temperature, thereby lowering the total amount of diffusion. The final cycle above the a_3 temperature controls the prior austenite grain size. Since all specimens received the same final solutionizing treatment, the grain sizes were approximately equal as shown in Appendix A. The ASTM prior austenite grain size number for each of the test conditions ranged from 11.5 to 12.5. These ASTM grain size numbers are equivalent to 'calculated' mean grain diameters of 66.7 μm and 47.2 μm respectively [62].

Shear deformation tests were performed. The data generated from each test included plastic shear stress-strain records (Figure 6), shear strain profiles (Figure 7), and a mean instability strain (γ_i). Shear stress-strain curves for the four normalizing

temperatures are presented in Figure 25. The points on these curves correspond to their respective peak stresses and instability strains. These instability strains were plotted as a function of the normalizing temperature in Figure 26. Notice that the maxima and minima of γ_i correspond to the minima and maxima of the geometric mean particle radius (R) respectively (see Figures 21 and 26). However, a non-linear relationship exists between γ_i and R as illustrated in Figure 27. A better relationship exists between γ_i and the volume fraction (f_v) (Figure 28), but gives no information concerning the spatial relationships of the particles. Therefore, the best method for graphically describing γ_i in terms of the particle size and distribution is through use of the dimensionless term; the interparticle spacing to geometric mean particle radius (λ/R) ratio introduced by Argon *et al.* [32]. A good fit of the experimental data for γ_i versus λ/R is presented in Figure 29. Linear regression was used to fit a straight line through the data, which also passed through the point $\gamma_i=0$, $\lambda/R=2$. The physical significance of this point being zero strain localization resistance while the particles are in intimate contact with one another. The observed increase in γ_i with increasing λ/R gives support to the theory that microvoid nucleation softening is responsible for flow localization in this material.

The fact that the interparticle spacing is important to shear instability, is indicative of particle stress field interaction as defined by Argon *et al.* [32], and analyzed by Tracey and Perrone [65] through an elastic-plastic finite element investigation of the three dimensional strain fields near pairs of interacting particles. The interactions enhance the interfacial stress and hasten void nucleation [65]. Given the same volume fraction (i,e the same λ/R ratio), small, evenly distributed particles permit larger strains prior to void nucleation. Conversely, large or unevenly distributed particles nucleate voids at relatively small strains, and ultimately degrade the material's ductility [33].

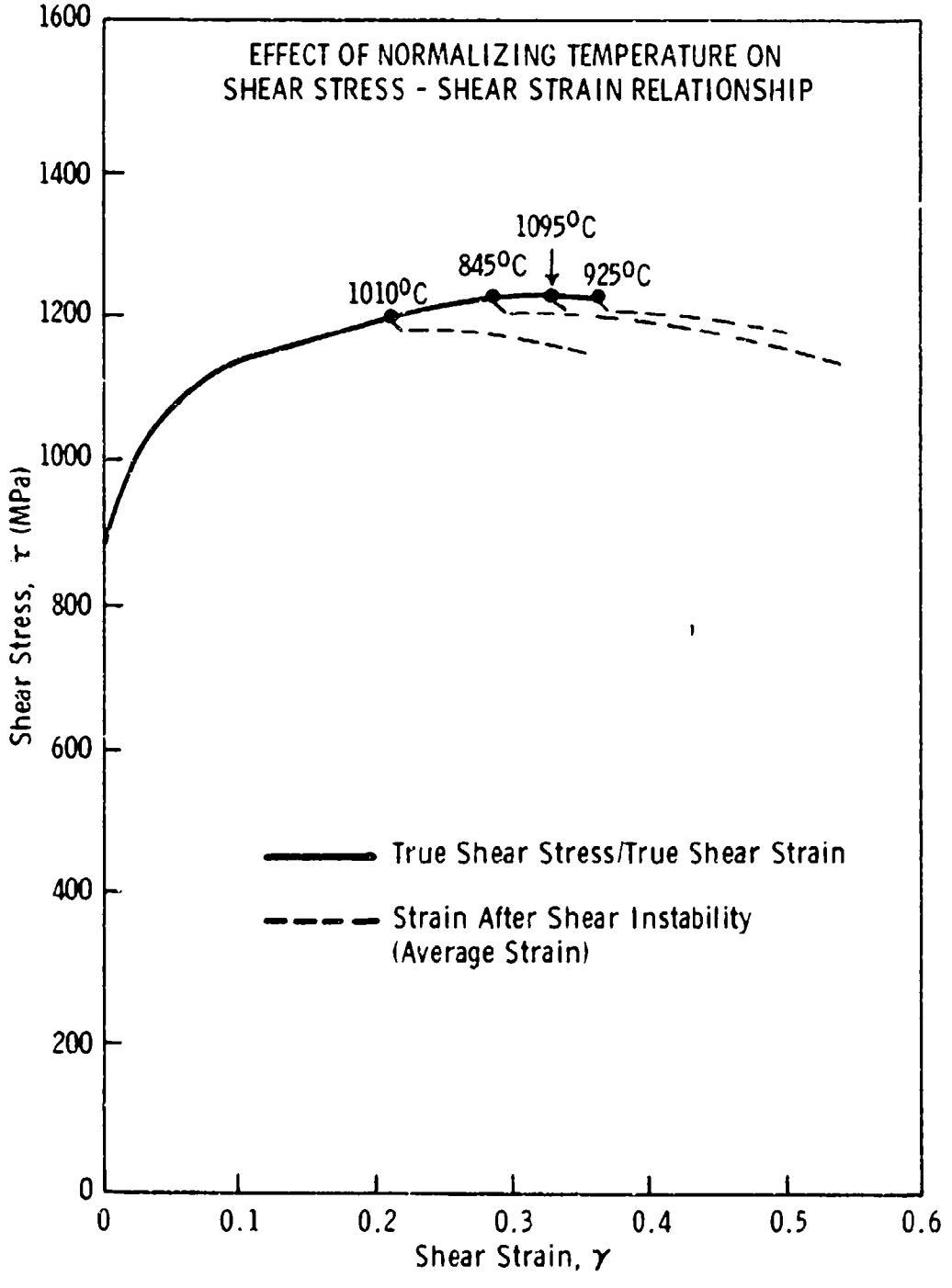

Figure 25. Shear stress-strain curves for four differently normalized material. The points on the curves correspond to their respective peak stresses and instability strains.

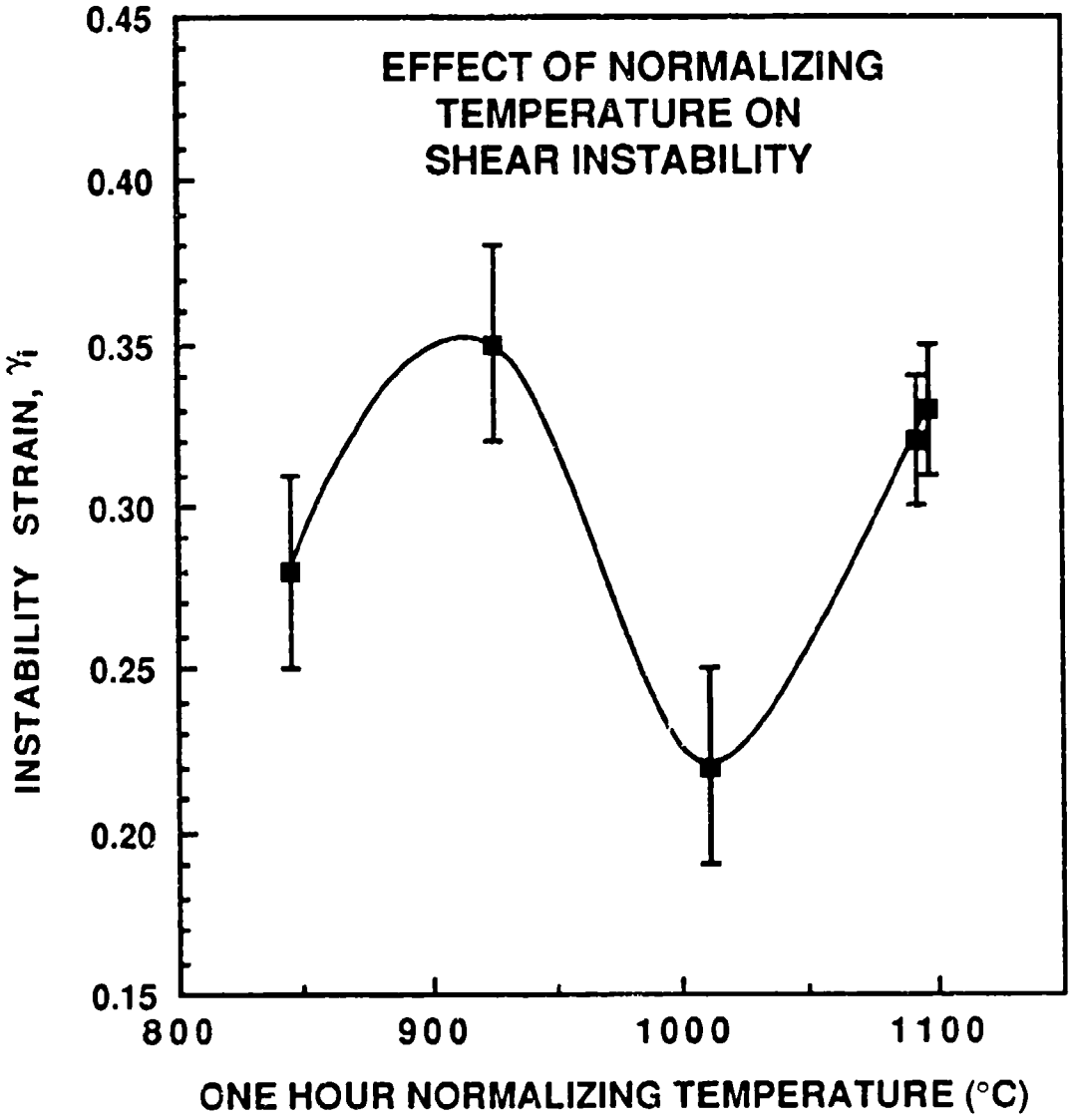

Figure 26. Instability strains plotted as a function of normalizing temperature. Notice that the maxima and minima of γ_i correspond to the minima and maxima of the mean particle radius R respectively (Compare with Figure 21).

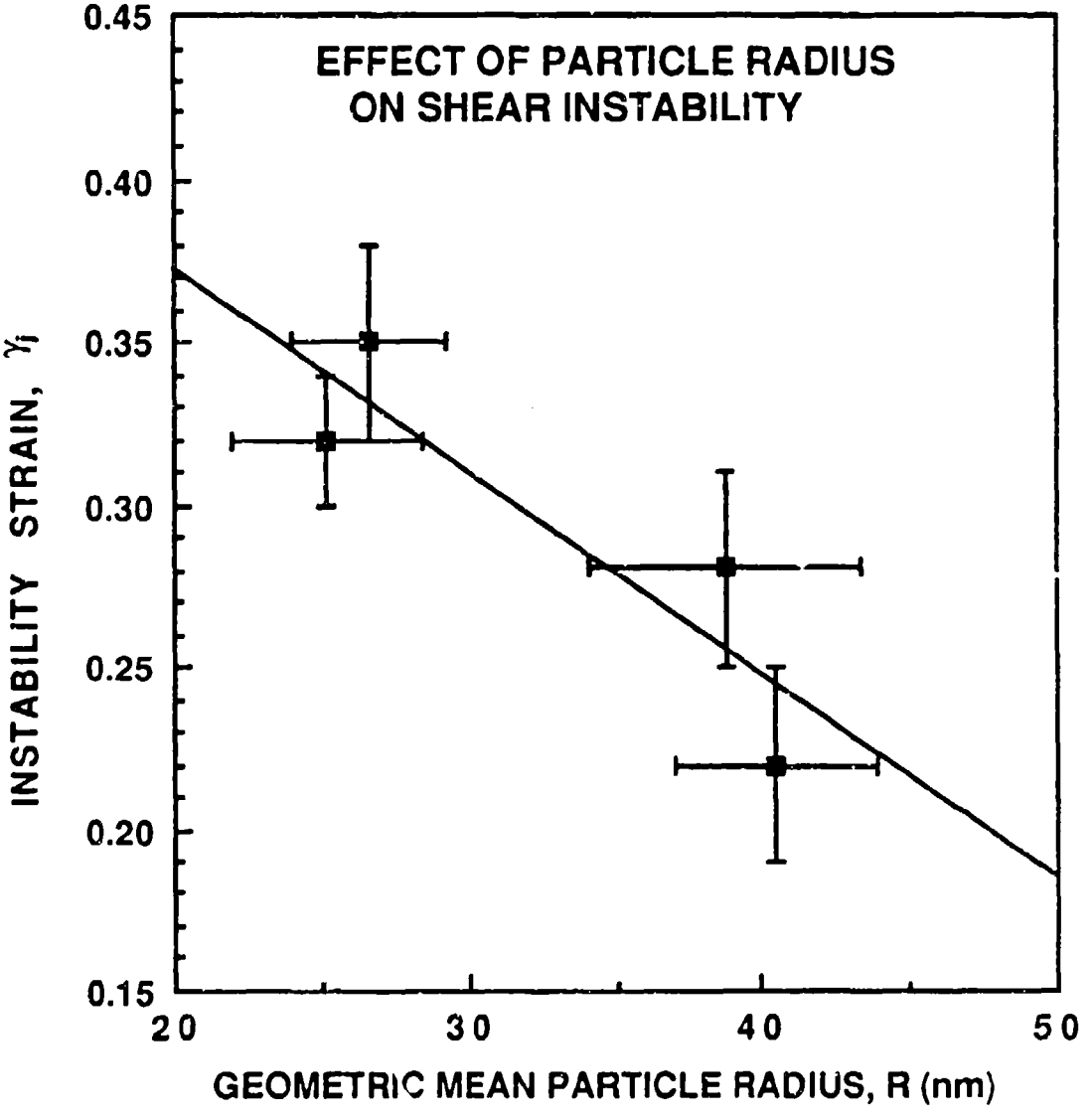

Figure 27. A poor relationship exists between shear instability strain and the geometric mean particle radius.

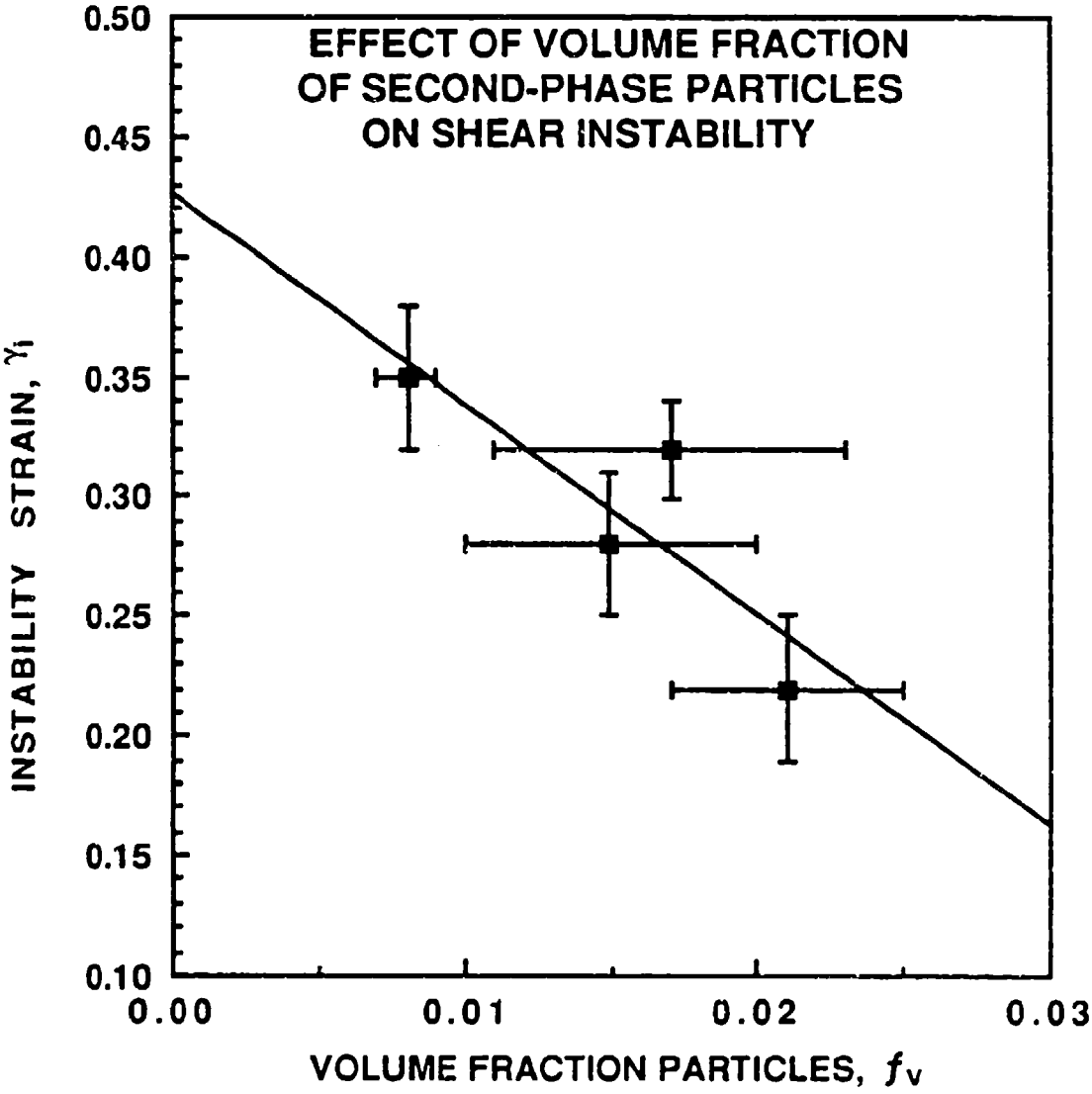

Figure 28. A linear relationship holds true between shear instability strain and volume fraction of second-phase particles.

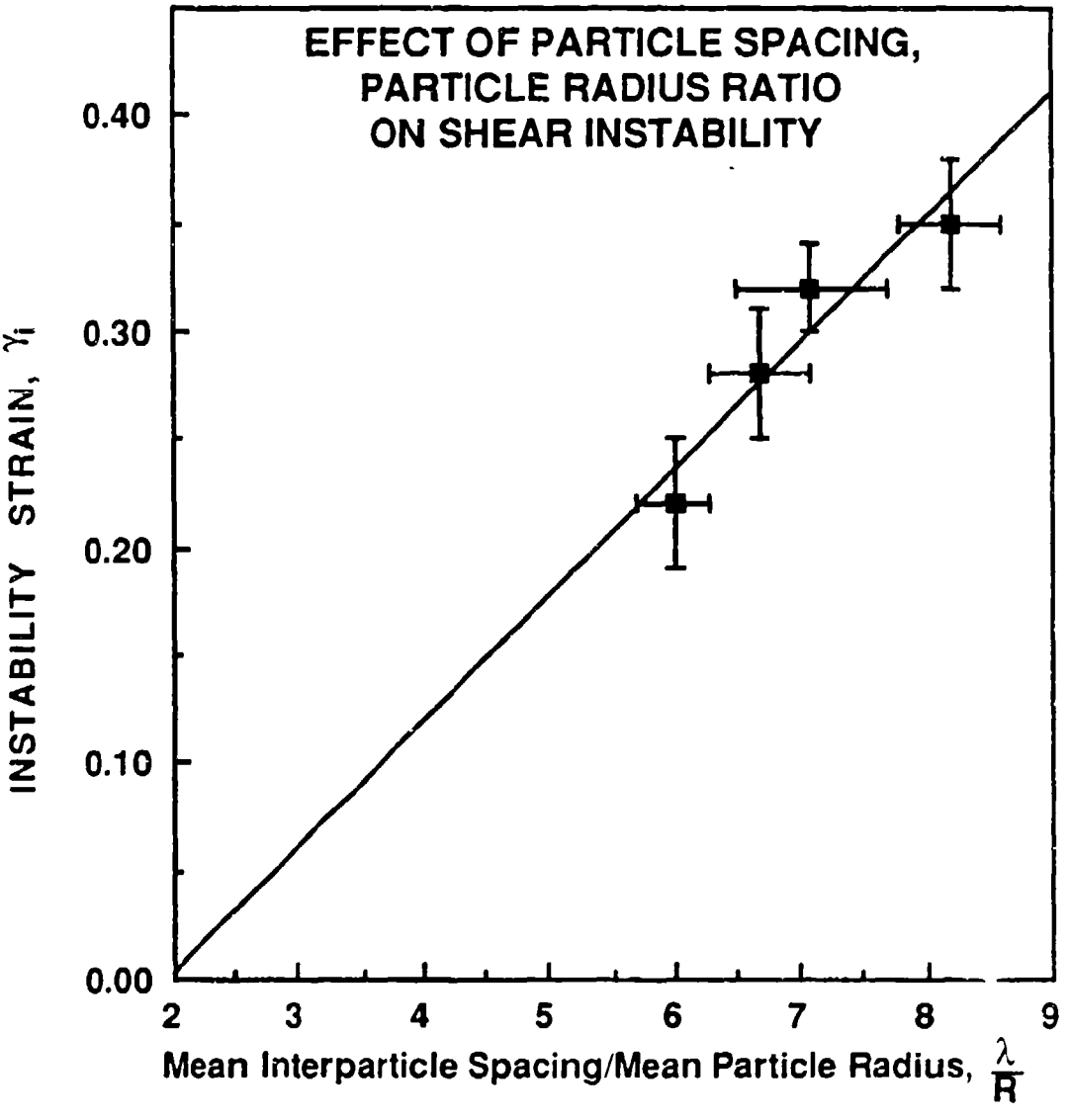

Figure 29. Linear regression was employed to fit a straight line through the experimental data of instability strain and λ/R dimensionless spatial relationship term.

The steel which was normalized at 1010°C, near the secondary recrystallization temperature, exhibited the poorest ductility. As detailed previously in the Quantitative Metallography Results section, a continuous string of coarsened aluminum nitride particles were observed in the prior austenite grain boundaries in this material. Although, the intergranular precipitation of aluminum nitrides is most closely tied to intergranular fracture in cast steels, aluminum nitride particles have also been observed in wrought 4340 steel by Materkowski [66].

Effect of Cryogenic Treatment

It was theorized that normalizing at different temperature would produce retained austenite contents; higher temperatures yielding more retained austenite. Furthermore, it was thought that these differences in retained austenite could potentially affect the shear instability strain by a transformation induced plasticity effect. In order to separate the effects of particles from the effect of retained austenite, the following study was performed.

The instability strains and retained austenite contents were compared for the specimens normalized at 845°C, 1095°C, and for a specimen given a post-normalization (1095°C) liquid nitrogen refrigeration treatment (77°K) for 24 hours. This was performed in order to transform some of the retained austenite to martensite. The retained austenite contents were measured using x-ray diffraction as outlined in Appendix B. Table VI summarizes the retained austenite measurements along with the shear instability strains. Within experimental error, all three specimens contained equivalent quantities of retained austenite (*i.e.*, 3%). This result indicates that the last cycle above the a_3 temperature (austenitizing treatment in this case) controls the retained austenite content.

TABLE VI. RETAINED AUSTENITE AND SHEAR INSTABILITY

Normalizing Temp. (°C)	Liquid Nitrogen Refrig. (77°K)	Austenitizing Temp. (°C)	Tempering Temp. (°C)	Retained Austenite (Vol. %)	Instability Strain γ_i
845	0	845	200	2.9±1.2	0.28
1095	24 hours	845	200	3.0±0.6	0.32
1095	0	845	200	3.2±0.8	0.33

Even though the retained austenite contents were essentially equivalent, the instability strains for the three materials differed. The two materials normalized at 1095°C have shear stress-strain curves (Figure 30) and strains which are essentially equivalent. The material normalized at 845°C has a lower instability strain than the materials normalized at 1095°C. These results indicate that the instability strain is a stronger function of the normalizing temperature, and particle size and distribution, than the retained austenite contents.

Effect of Pressure

In order to verify the pressure dependent behavior previously reported in lower strength steels [11] and in UHS 4340 steels [2], shear specimens were tested quasi-statically with a superimposed axial compressive load. Finite element calculations indicate that the stress component arising from this axial load reasonably approximates uniaxial stress once plastic shear deformation is underway [50].

During testing, a mean axial compressive stress equal to 1/4 the material's tensile yield stress was used. The small deviatoric stress associated with the axial stress was not accounted for in the stress-strain curves. However, it was calculated to be less than 1% of the total effective stress during plastic deformation.

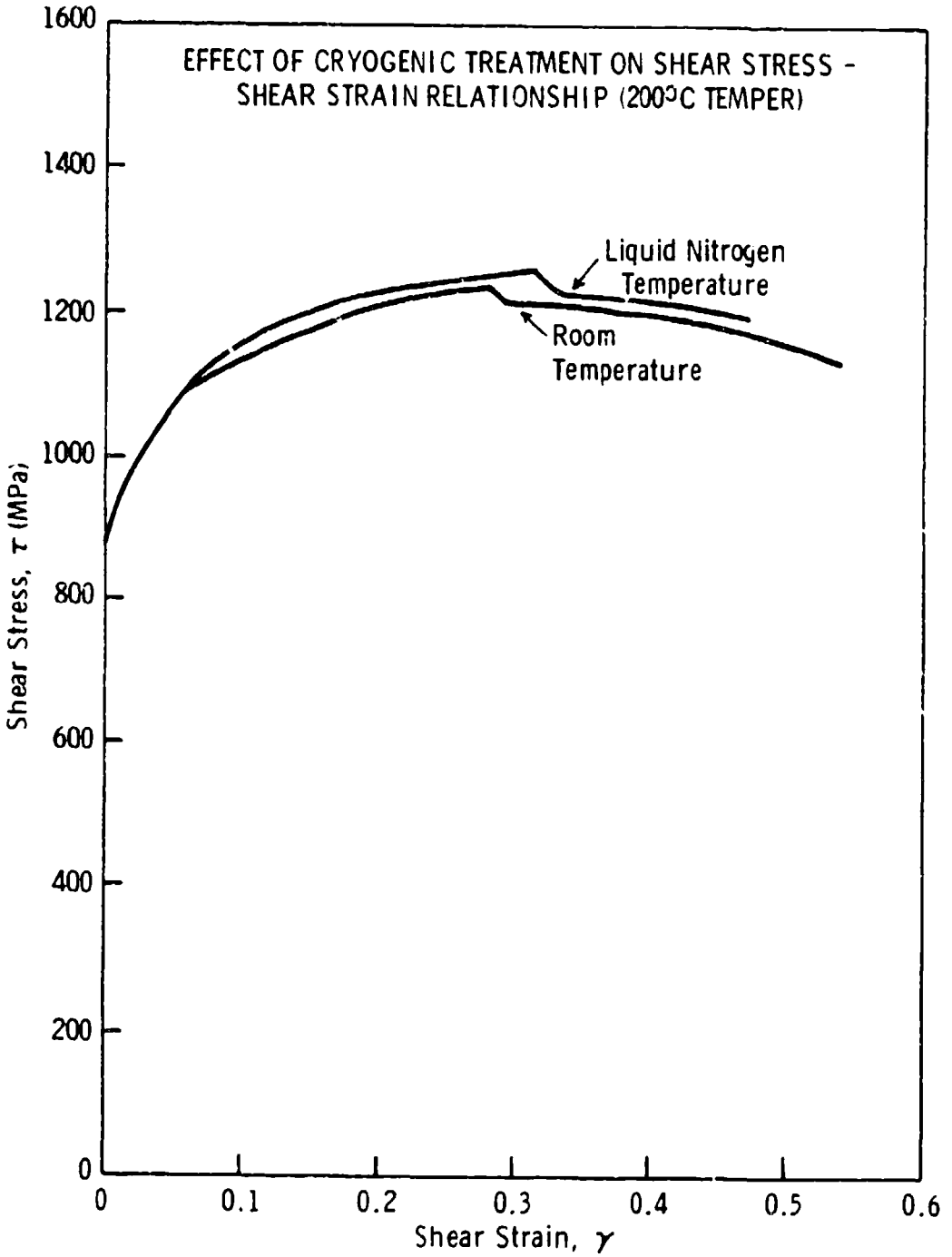

Figure 30. Shear stress-strain curves for two materials normalized at 1095°C, austenitized at 845°C and tempered at 200°C. One of the specimens was given a 24 hour liquid nitrogen temperature refrigeration treatment after normalizing. There is little effect of this cryogenic refrigeration treatment.

The stress-strain results clearly show pressure dependent behavior for both R_c 54 (Figure 31) and R_c 29 (Figure 32). As the axial stress is increased from 0 to 1/3 the yield stress, the instability stain is increased for both hardness levels as illustrated in Figures 33 and 34. Air melted instability strain data are included in Figures 33 and 34 from reference [2]. In the case of the lower strength (R_c 29) material, the VAR 4340 produced significantly higher instability strains than the AM 4340, probably owing to the lower inclusion content of VAR steels. For the UHS 4340 steel (R_c 54), the instability strains for both AM and VAR steels were approximately equivalent.

The stress-strain curves (Figures 31 and 32) for these two hardness levels show greater ultimate shear strengths with an applied compressive axial load normal to the shear plane. This result indicates that a hydrostatic compressive stress field produced by the axial load must be overcome by the shear stress in order to attain particle decohesion, and ultimately microvoid nucleation softening.

Summarizing, the pressure dependent behavior of the instability strain can be attributed to the stress required to debond the second-phase particles from the matrix and form microvoids. This interpretation is supported by the recent analysis by Fleck *et al.* [67] on microvoid nucleation softening as a basis for shear instability.

Effect of Strain Rate

Shear tests were performed under dynamic conditions; shear strain rate approximately equal to $10^4\ s^{-1}$. Both the low hardness (650°C temper) and high hardness (200°C temper) materials were tested and compared with their counterparts tested quasi-statically at $10^{-3}\ s^{-1}$. Figures 35 and 36 illustrate the stress-strain behavior for these two materials with strain rates seven orders of magnitude apart. Clearly, from the stress-strain curves and from the strain profile measurements presented in Table VII, it can be observed

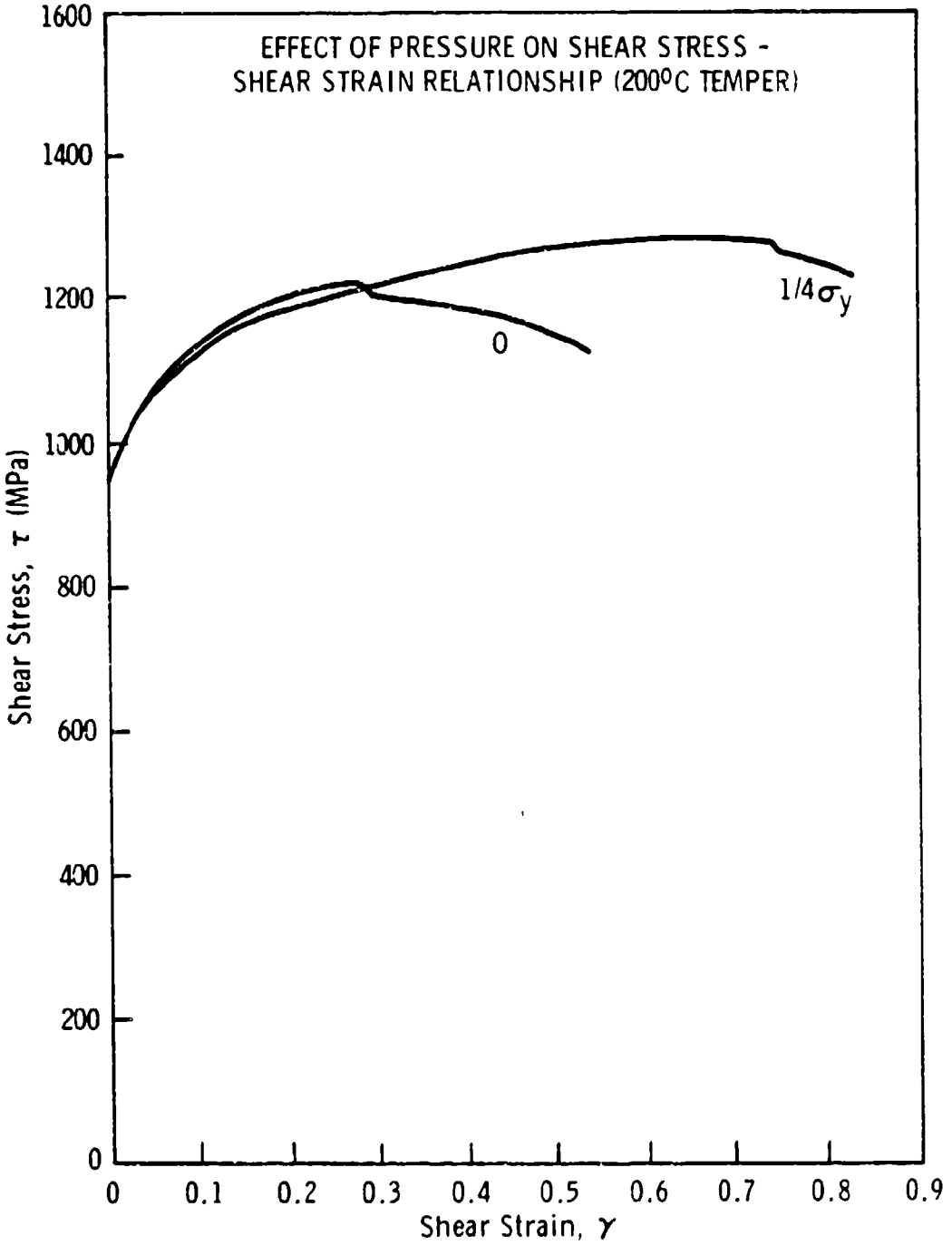

Figure 31. Shear stress-strain curves for the same material (normalized at 845°C, austenitized at 845°C and tempered at 200°C) tested with and without a superimposed load equal to 1/4 the tensile yield stress normal to the shear plane. The instability strain is favorably affected by the resulting hydrostatic compression.

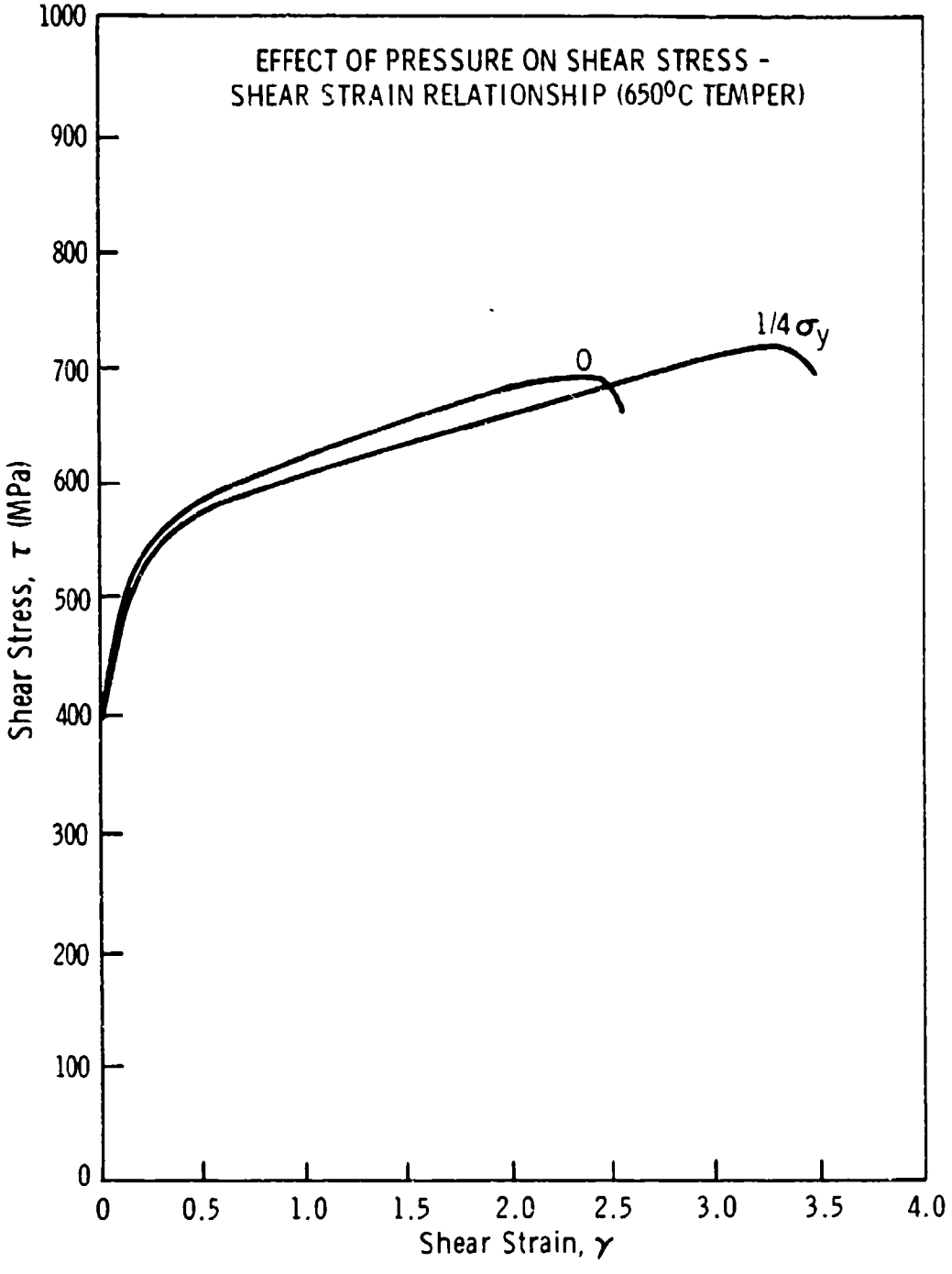

Figure 32. Shear stress-strain curves for the same material (normalized at 845°C, austenitized at 845°C and tempered at 650°C) tested with and without a superimposed load equal to 1/4 the tensile yield stress normal to the shear plane. The instability strain is favorably affected by the resulting hydrostatic compression.

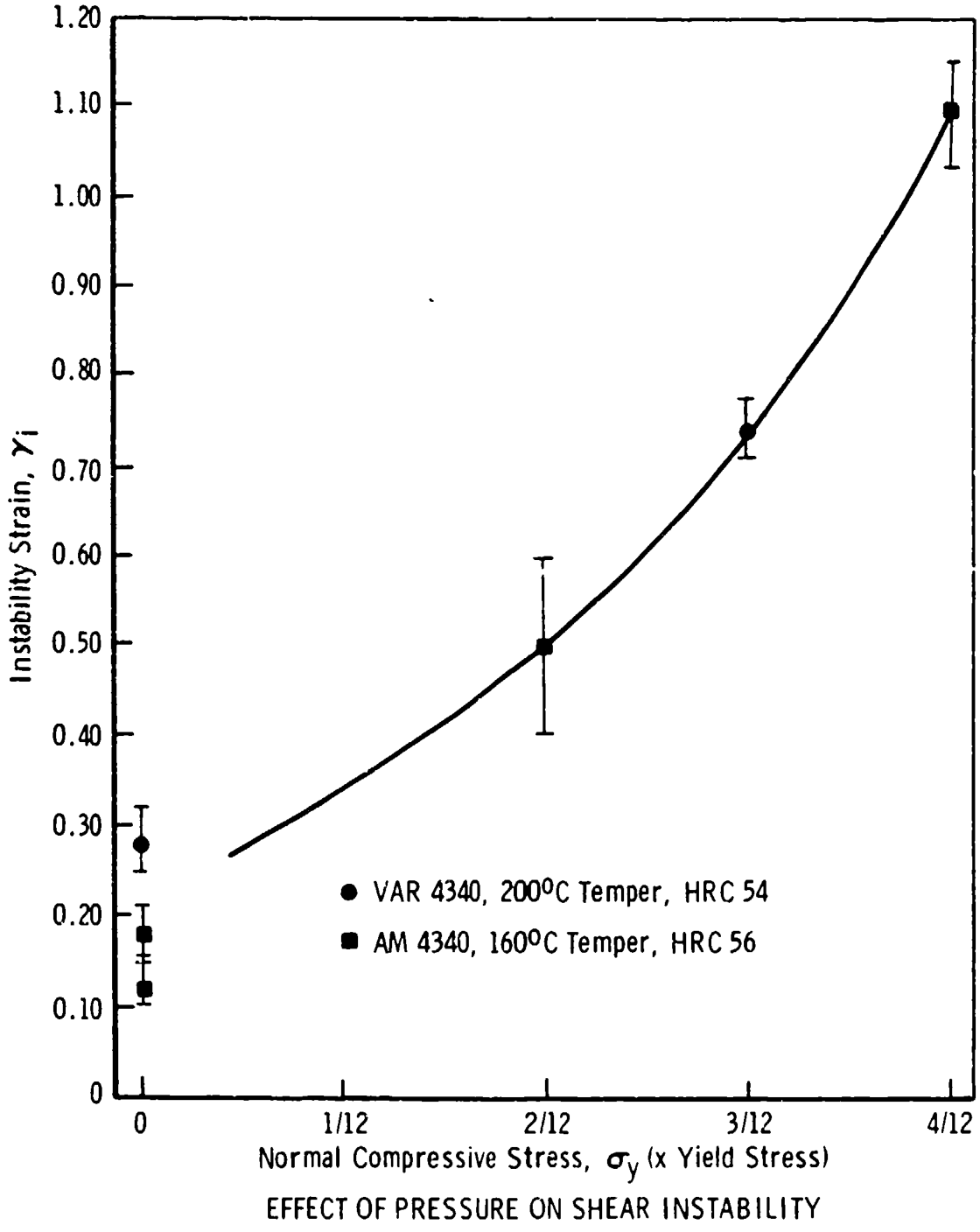

Figure 33. Instability strain plotted as a function of superimposed pressure normal to the shear plane for the 200°C tempered material. Air melted material data from reference [2].

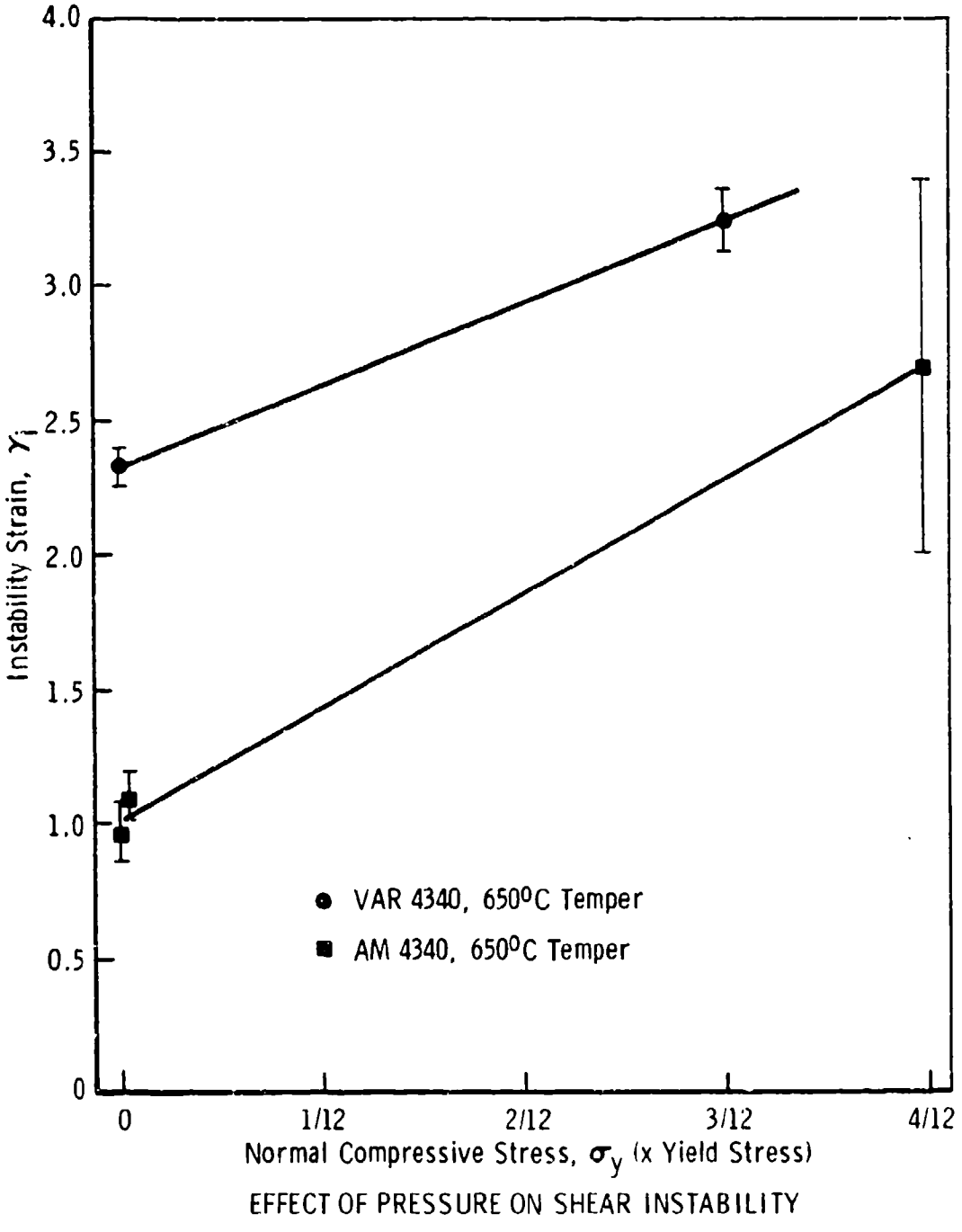

Figure 34. Instability strain plotted as a function of superimposed pressure normal to the shear plane for the 650°C tempered material. Air melted material data from reference [2].

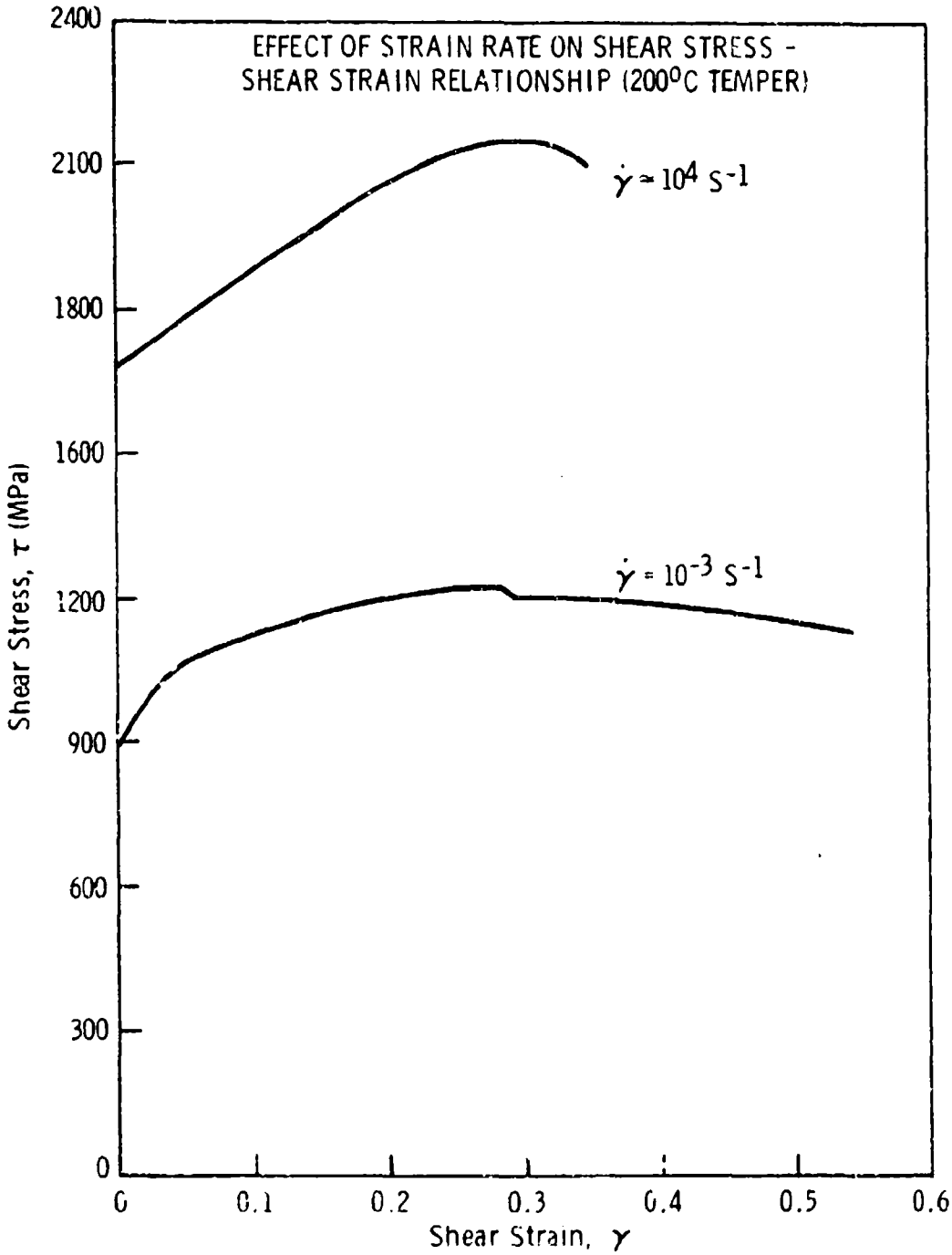

Figure 35. Shear stress-strain curves for the same material (normalized at 845°C, austenitized at 845°C and tempered at 200°C) tested at high and low strain rates. There was little effect of strain rate on the instability strain.

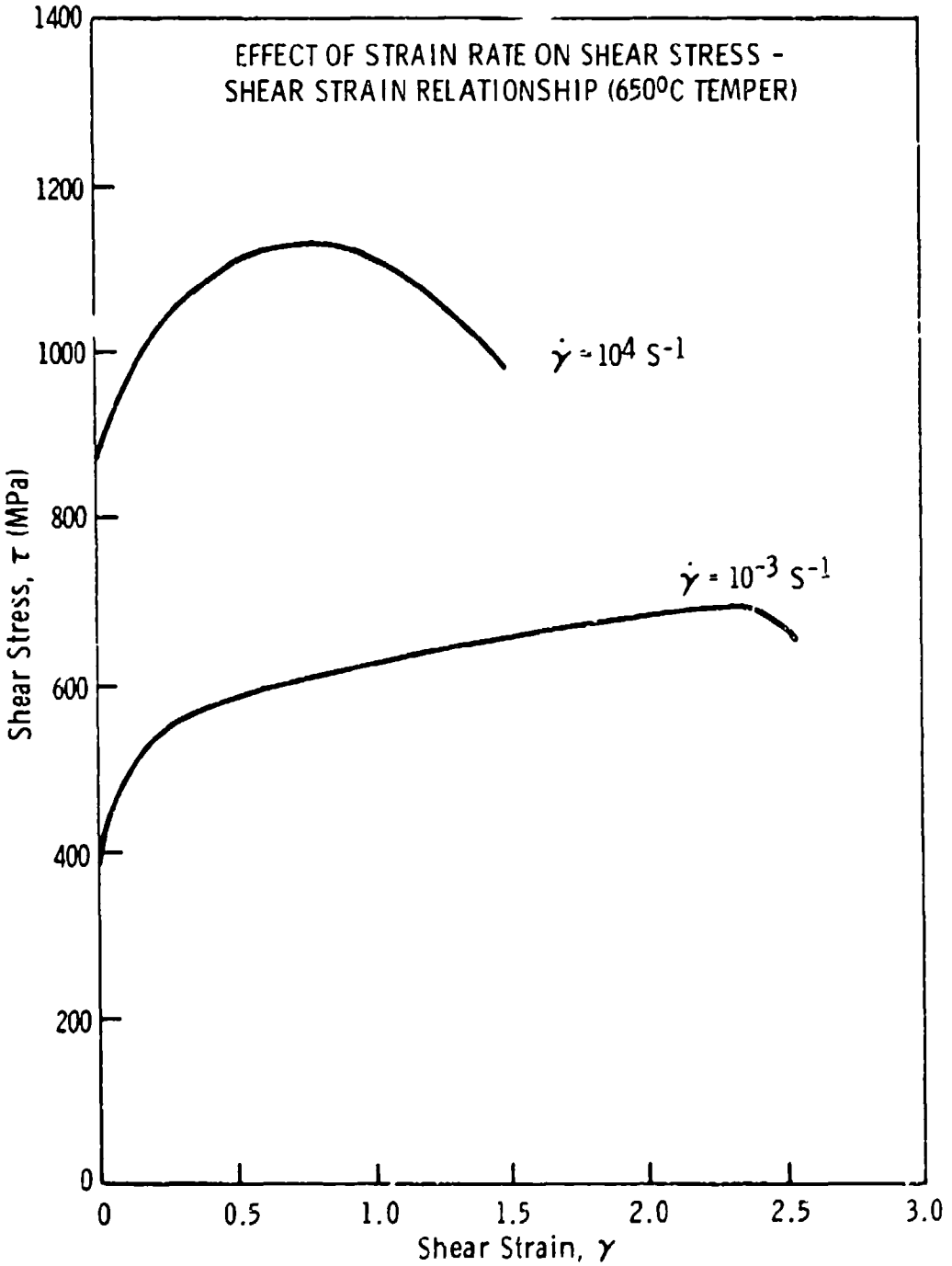

Figure 36. Shear stress-strain curves for the same material (normalized at 845°C, austenitized at 845°C and tempered at 650°C) tested at high and low strain rates. Higher strain rates produced somewhat lower instability strains for this lower strength material.

that strain rate has little effect on the instability strain for the UHS material (R_c 52). For the R_c 29 material, the instability strain decreased with increasing strain rate. The flow stress for both materials increased with strain rate, and the effect at constant strain can be approximated by

$$\sigma = C\,\dot{\varepsilon}^{m}$$

where σ is the flow stress, C is a strength constant, $\dot{\varepsilon}$ is strain rate, and m is the strain rate sensitivity of the flow stress. Assuming von Mises yield criteria holds, *i.e.*, $\sigma = \sqrt{3}\,\tau$ and $\dot{\varepsilon} = \sqrt{3}\,\dot{\gamma}$, then

$$\tau = C\,\dot{\varepsilon}^{m}$$

where τ is the shear flow stress, and $\dot{\gamma}$ is the shear strain rate. The magnitudes of the strain rate sensitivities for both materials are presented in Table VII, and are low (< 0.05) as expected for metals at room temperature [68].

TABLE VII. EFFECT OF STRAIN RATE

Normalizing Temp. (°C)	Austenitizing Temp. (°C)	Tempering Temp. (°C)	Strain Rate, $\dot{\gamma}$ (s^{-1})	Instability Strain, γ_i	Strain Rate Sensitivity, m
845	845	200	10^{-3}	0.28	0.036
845	845	200	10^{4}	0.30	0.036
845	845	650	10^{-3}	2.33	0.040
845	845	650	10^{4}	0.85	0.040

For the ultrahigh strength steel (200°C temper), the instability strain was not affected by the nearly 100% adiabatic condition ($\dot{\gamma} = 10^{4}$ sec^{-1}). This fact implies that there

is little or no effect of deformation heating produced thermal softening influencing instability, the point at which shear localization or "adiabatic shear" begins. Shear bands which form during strain localization are the thin white etched bands often mentioned in the literature [4-6]. It is believed that shear bands are the result of a combination of intense strain and a thermal effect associated with high strain rate deformation. Thermal softening only becomes the dominant softening mechanism once strain localization has occurred. The results further suggest that there must be some sort of microstructural, destabilizing influence responsible for producing the instability, which is further investigated in the following section on microvoid nucleation at second phase-particles.

Microvoid Observations

The fine 100 nm scale of microvoid formation makes microscopy observations difficult compared to the more familiar problem of >100 nm scale 'primary' void formation which has been well studied by light microscopy. A study was undertaken to photograph these fine scale microvoids. Transmission electron microscopy was performed on thin foil specimens of both strained and unstrained UHS 4340 steel. The microstructure of the unstrained material shown in Figure 37 consists of a martensitic lath matrix with a fine dispersion of ε-carbides. In addition, there are submicron sized second-phase particles which act as grain refiners. These second phase particles have been identified in the Quantitative Metallography section of this study as (Fe, Si, Ca, and Al) oxides, nitrides and carbides (see Table V).

During straining, the strain fields of these particles interact [65] leading to cooperative microvoid nucleation. Figure 38 presents a TEM photomicrograph of strained material illustrating a pair of particles linked by microvoids. The photograph was taken in a rather thick region of the thin foil, since the particles would have fallen out if additional thinning were performed. This thin foil specimen was removed from the gauge section of a

Figure 37. TEM photomicrograph of the microstructure of unstrained 4340 steel (Rc 52) consists of a heavily dislocated martensitic lath matrix with a dispersion of submicron sized second-phase particles.

Figure 38. TEM photomicrograph of microvoid nucleation around a pair of second-phase particles.

linear shear specimen which was strained to instability. The micrograph was taken in the region which received only uniform deformation which ceased straining once instability had occurred. Many particles were observed to exhibit this type of behavior. The directions of the void growth appear aligned in the direction of the principal stress (σ_1). Shear cracks linked void pairs predominantly along the direction of the imposed shear stress direction, approximately 45° to (σ_1). These experimental results are consistent with the analytical calculations of interacting void pairs by Tracey and Perrone [65].

Although specimen preparation by electropolishing may have enlarged the voids, no such voids were observed in identically prepared foils taken from the unconstrained specimen. Additionally, the fracture surface of a shear specimen tested to fracture contained microvoids having a mean diameter approximately equal to the interparticle spacing, indicative of a microvoid sheet type fracture mechanism, as illustrated in Figure 39. It can be concluded that the voids observed in the strained thin foil specimens were genuinely produced by the plastic deformation.

An earlier study [2] on high strength AM 4340 steel showed SEM photographs taken from interrupted shear tests. Microvoid profusion was observed at peak stress The abrupt appearance of microvoids supports a nucleation-controlled rather than growth-controlled softening mechanism as described in the literature [67].

Chi [69] experimentally measured the microvoid nucleation strains in the same heat of steel investigated in this study. Measurements were taken of the local strains at various points along the axes of notched tensile specimens. The specimens were then cross-sectioned and the void area fraction (N_A) was measured along the length of the specimen using an SEM. Chi states that *"voids were observed to initiate at submicron carbide particles, and accordingly, the percentage of submicron particles associated with voids was*

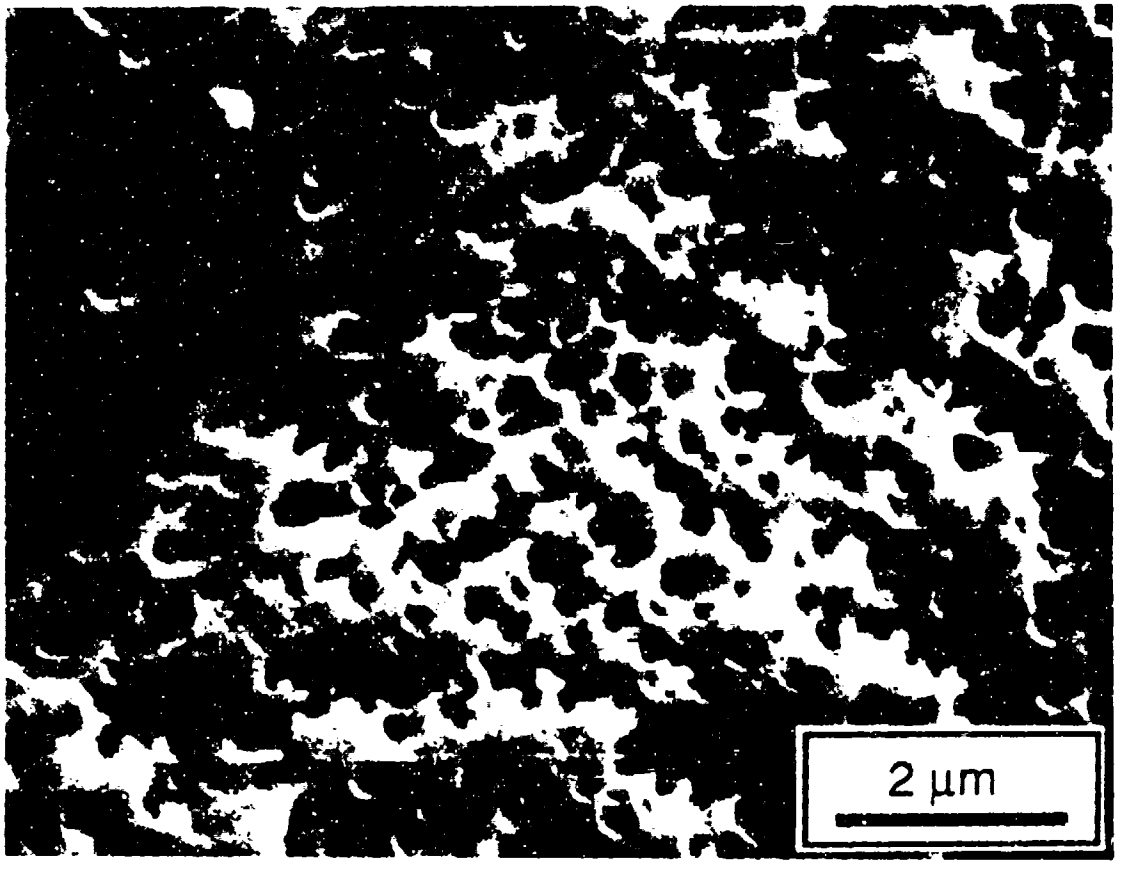

Figure 39. SEM fractograph of a shear specimen tested to failure. The specimen failed by a microvoid sheet type fracture mechanism. The void diameters scale with the interparticle spacing.

measured" [69]. N_A was quantitatively related to the strain measurements. The void nucleation strain (ε_v) was taken as the greatest strain (ε) having no voids.

Chi's study [69] employed the identical material, austenitizing treatment, quenching medium, and tempering treatment. However, the normalization treatment was performed at 900°C. By interpolating the instability strain (γ_i) at 900°C from Figure 26 (normalizing temperature versus instability strain), γ_i equals 0.328, which can be assumed to be the void nucleation shear strain. Assuming von Mises yield criteria holds true, *i.e.*, $\gamma = \sqrt{3}\,\varepsilon$, then ε_v=0.17 measured by Chi [69] can be converted to γ_i = 0.294. This results in a relative difference of only 10% between Chi's instability strain (γ_i =0.294) and this study's instability strain (γ_i =0.328). These results compare very nicely considering the completely different experimental approaches.

FRACTURE TOUGHNESS - SHEAR INSTABILITY CORRELATIONS

Results of standard Charpy tests performed at both room temperature and at -40°C for five different normalizing temperatures are presented in Figure 40. As could be predicted by the shear instability results as a function of normalizing temperature, the blunt-notch toughness decreases dramatically at approximately 1000°C, the approximate grain coarsening temperature for this material. Likewise, the sharp-crack fracture toughness (K_{Ic}) results, again plotted as a function of normalizing temperature, exhibited the same behavior (Figure 41). The drop in K_{Ic} at 1000°C is precipitous. As previously reported, this material experiences aluminum nitride embrittlement around this temperature which is reflected in both K_{Ic} and Charpy test data.

The square root of the second-phase particle spatial relationship term ($\sqrt{\lambda/R}$) multiplied by the square root of the interparticle spacing ($\sqrt{\lambda}$, herein defined as the critical distance ($\lambda/\sqrt{R}$), displayed a relatively good linear relationship with toughness (K_{Ic}), illustrated in Figure 42. The K_{Ic} - $\lambda/\sqrt{R}$ linear relationship can be extrapolated back to zero toughness (K_{Ic}= 0) at zero particle spacing ($\lambda/\sqrt{R}$ = 0) making excellent physical sense.

Mode I Fracture Toughness Model

Inspired by the K_{Ic}- $\lambda/\sqrt{R}$ (Figure 42) relationship, a simple fracture toughness model was derived. Employing the classic work by Hutchinson [70], Rice and Rosengren [71] on a tensile crack in a power-law hardening material

$$\sigma_{ij}\,\varepsilon_{ij} = \frac{J}{2\pi\, r}$$

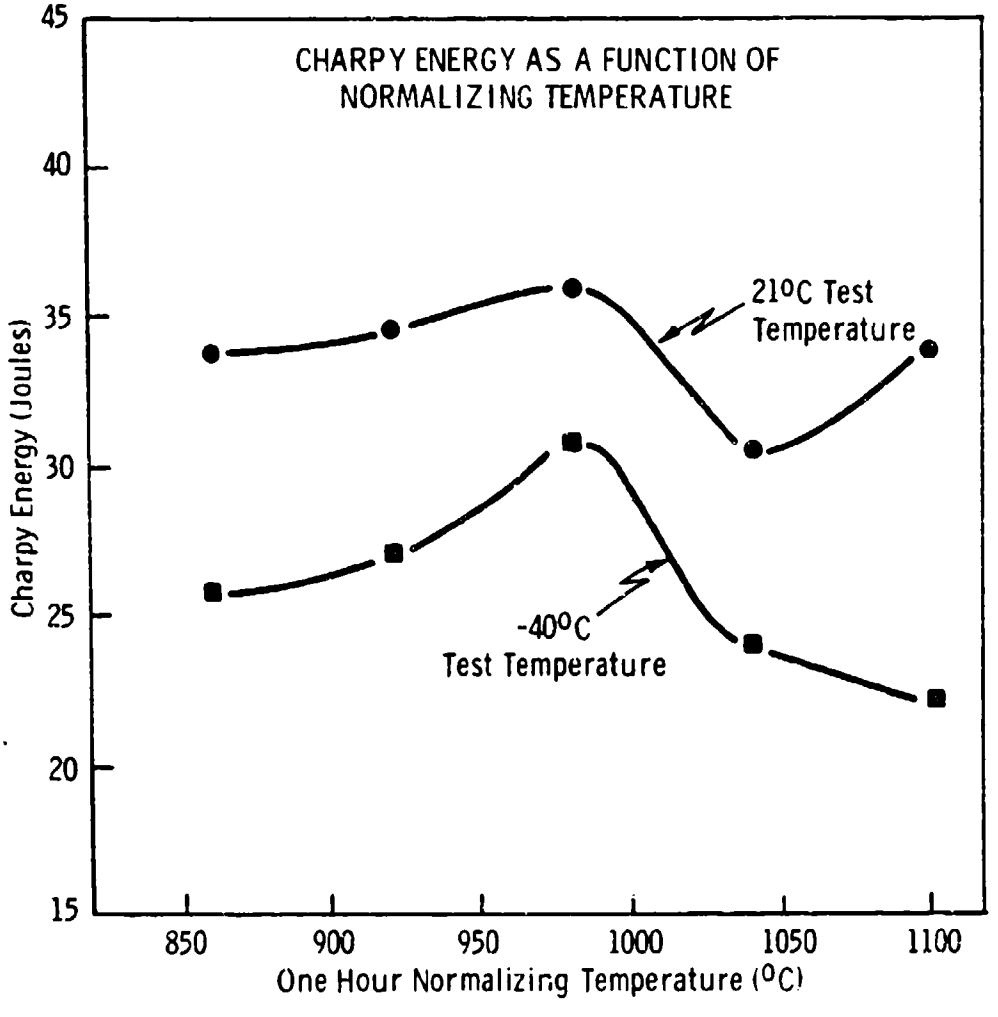

Figure 40. Charpy Vee-notch impact toughness plotted as a function of normalizing temperature. A minimum Charpy energy exists at approximately 1000°C, the aluminum nitride embrittlement temperature. All specimens austenitized at 845°C and tempered at 200°C.

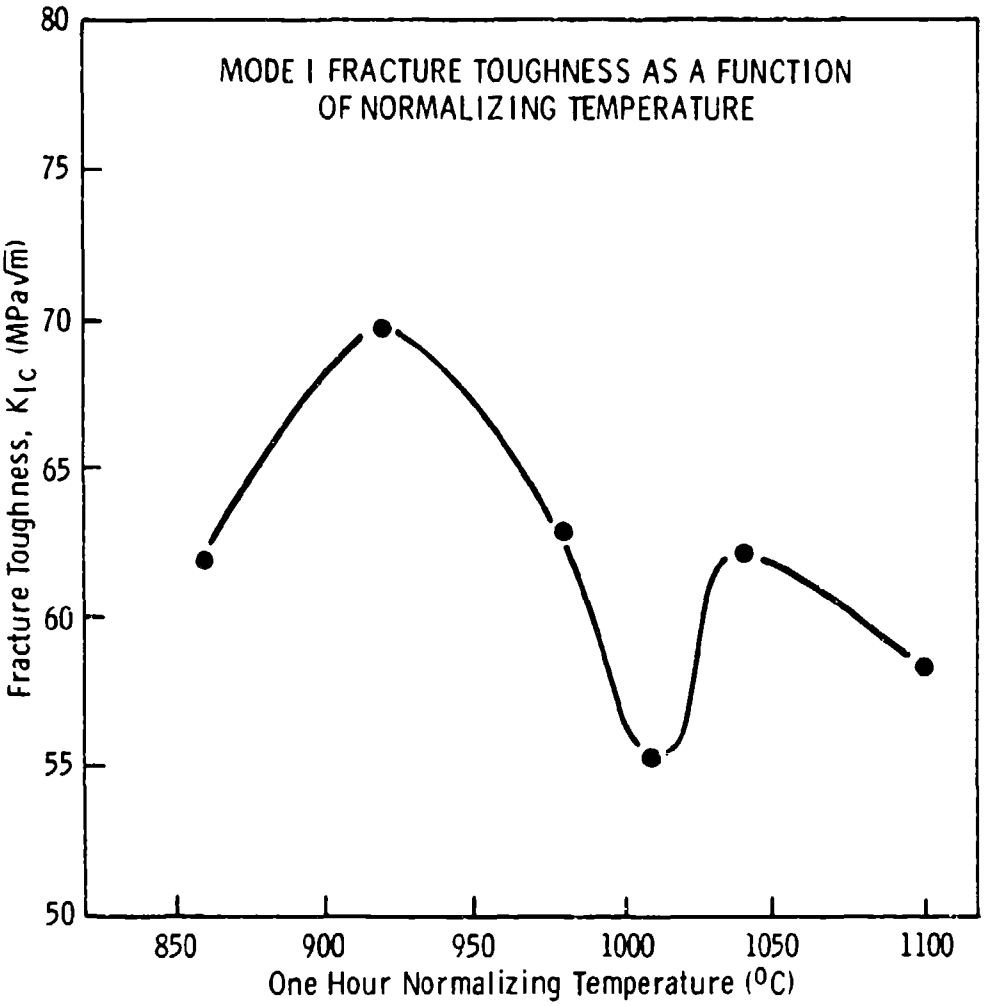

Figure 41. Sharp-notch fracture toughness K_{Ic} plotted as a function of normalizing temperature. A minimum in toughness exists at approximately 1000°C, the aluminum nitride embrittlement temperature. All specimens austenitized at 845°C and tempered at 200°C.

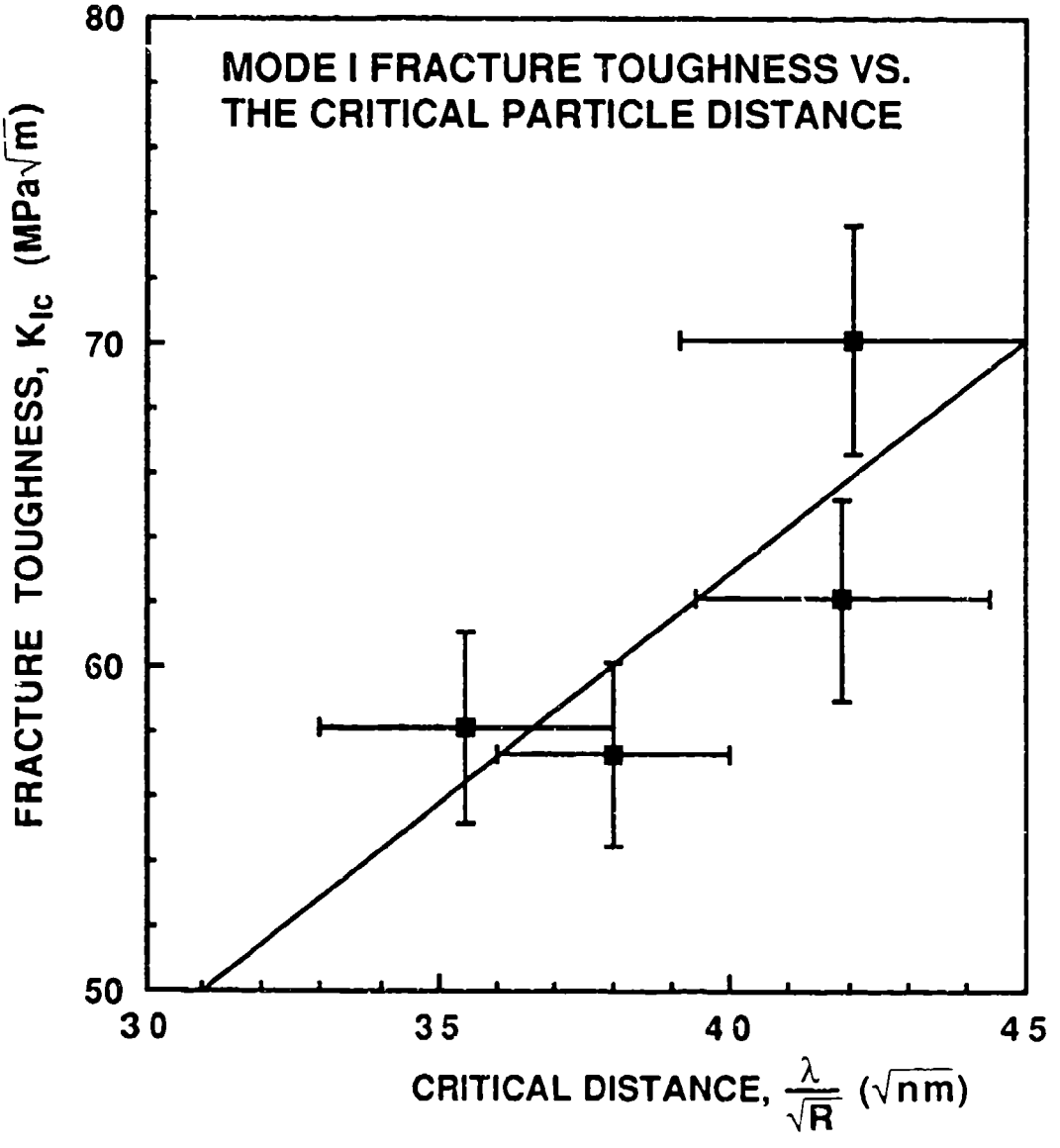

Figure 42. Critical stress intensity factor K_{Ic} plotted as a function of the critical particle distance $\lambda/\sqrt{R}$.

where σ is stress, ϵ is strain, r is the distance from the crack tip, and J is the integrated release of crack driving energy. When linear elastic fracture mechanics (LEFM) applies, $J = G$, and

$$\sigma\epsilon = \frac{G}{2\pi r}$$

Tetelman and McEvily [72] first introduced the concept that critical mode I crack extension force (G_{Ic}) is reached when the critical strain (ϵ^*) is attained some critical distance (r^*) from the crack tip, schematically illustrated in Figure 43. Also, σ_N is defined as the microvoid nucleation stress. Toughness can then be related to these critical parameters

$$G_{Ic} = 2\pi r^* \epsilon^* \sigma_N$$

Upon conversion of G_{Ic} to K_{Ic} the LEFM plane strain relationship can be employed

$$K_{Ic} = \sqrt{\frac{G_{Ic}E}{(1-\upsilon^2)}}$$

where E is Young's Modulus of elasticity and υ is Poisson's ratio. K_{Ic} becomes

$$K_{Ic} = \sqrt{\frac{2\pi r^* \epsilon^* \sigma_N E}{1-\upsilon^2}}$$

For void nucleation to occur, it is assumed that the critical distance (r^*) is equal to the interparticle distance (λ) multiplied by the λ/R dimensionless spatial parameter. This λ/R term is included as a critical distance multiplier because particle interactions enhance the interfacial stress and hasten particle-matrix decohesion [33]. The critical stress to void nucleation varies with the size and distribution of particles. Larger values of λ/R help to delay particle interaction, promoting greater toughness. Consequently, the number of

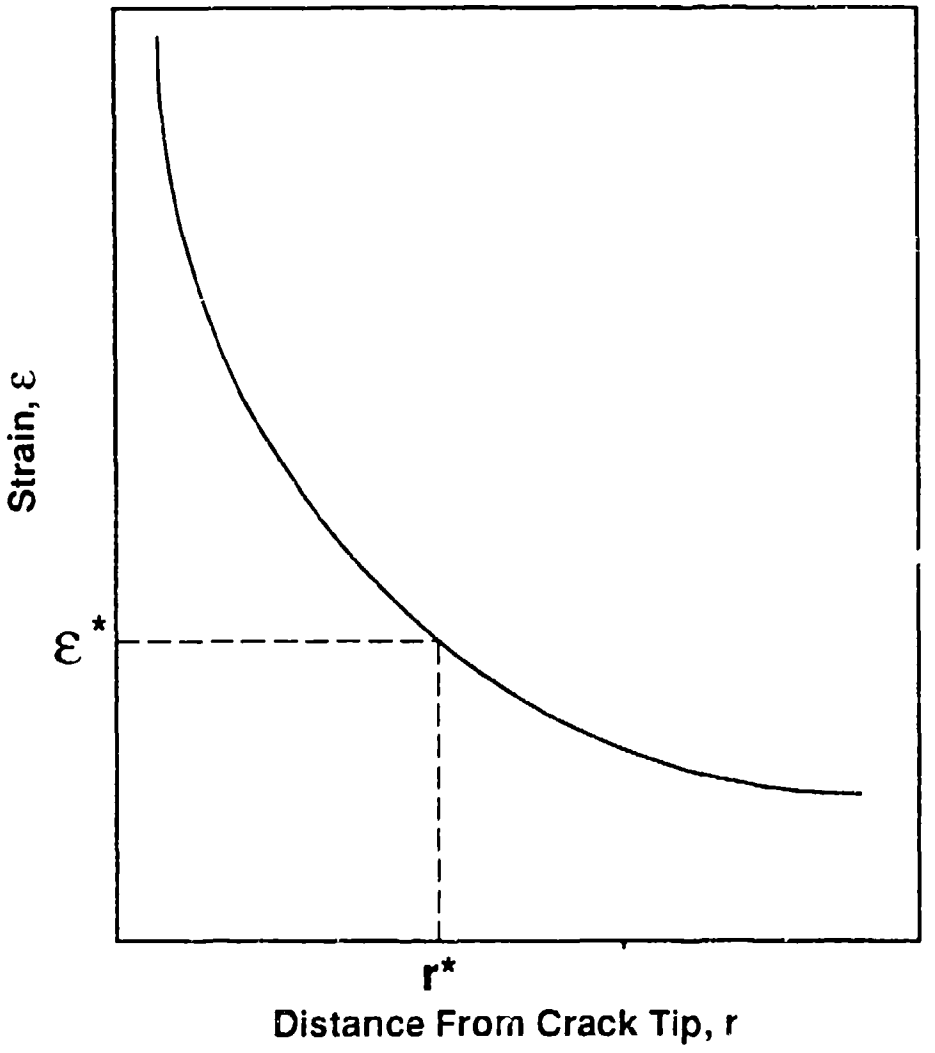

Figure 43. Schematic representation of the strain field in front of a sharp crack under a tensile load. A critical strain ε^* is found to exist a critical distance r^* from the crack tip. From reference [72].

nucleated voids is a direct function of the λ/R term. Fracture toughness can now be written as

$$K_{Ic} = \sqrt{\frac{2\pi}{(1-\upsilon^2)} \left(\frac{\lambda}{R}\right) \lambda \, \varepsilon^* \, \sigma_N \, E}$$

Further, the critical strain (ε^*) can be assumed to occur at the onset of void nucleation or at shear instability

$$\varepsilon^* = \sqrt{3}\,\gamma_i$$

The void nucleation stress is derived within the framework for progressively cavitating solids introduced by Gurson [73,74]. Void nucleation was shown to be strongly dependent on the hydrostatic stress (σ_H) as well as the effective stress (σ_E). Needleman [75] proposed that nucleation stress (σ_N) can be thought of in terms of a combination of σ_H and σ_E

$$\sigma_N = \sigma_E + c\,\sigma_H$$

where c is the hydrostatic coefficient. In one set of Needleman's calculations, c was chosen so that the average nucleation stress (σ_N) was the same for all cases investigated. In the present study, an average c was arrived at using the experimental data. This average c is 0.5, which is physically reasonable. Needleman [75] states that *"values of c less than unity in $\sigma_N = \sigma_E + c\sigma_H$ can be thought of as due in part to the remote hydrostatic stress being 'converted' to local shearing stresses around the inclusion, the magnitude of which are limited by the work hardening capacity of the material."* In Needleman's [75] concluding remarks, he states that *"this critical nucleation stress depends linearly on the hydrostatic tension, but with a coefficient that is less than unity."*

In the case of the steel normalized at 1010°C, which suffers from aluminum nitride embrittlement, a different hydrostatic coefficient was used. Brittle interfaces associated with larger or poorly bonded particles are characterized by a more strongly hydrostatic stress dependent nucleation stress [75]. The value of c for this material is unity reflective of its brittle particle interfaces [75]. For the lower strength steel tempered at 650°C, the cementite responsible for microvoid nucleation is in the form of large particles that are poorly bonded with the matrix. Consequently, c is also equal to unity for this material. The calculated fracture toughness (K_{Ic}= 94 MPa$\sqrt{m}$) for this lower strength steel is nearly equal to fracture toughness measured by Hickey and Thomas using the same heat of steel (K_{Ic}= 99 MPa$\sqrt{m}$) [76].

The final form of the fracture toughness equation relating the critical mode I stress intensity factor to experimentally derived parameters is written

$$K_{Ic} = \sqrt{\frac{2\pi}{(1-\upsilon^2)} \left(\frac{\lambda}{R}\right) \lambda \, \varepsilon_i \, E \, (\sigma_E + c \, \sigma_H)}$$

For pure mode I crack extension, σ_E and σ_H are equal to each other (see Appendix C). Table VIII presents the experimental data used in the calculation of K_{Ic}. The predicted K_{Ic} value from the above equation is compared with experimentally determined K_{Ic} value in Figure 44 and Table IX.

Excellent agreement exists between the measured and calculated K_{Ic} values. It can be concluded that the derived relationship between fracture toughness and its material parameters is valid for these particular steels and this fracture mode. It is believed that this model is valid for other materials that fail by a microvoid nucleation controlled shear instability type failure mechanism.

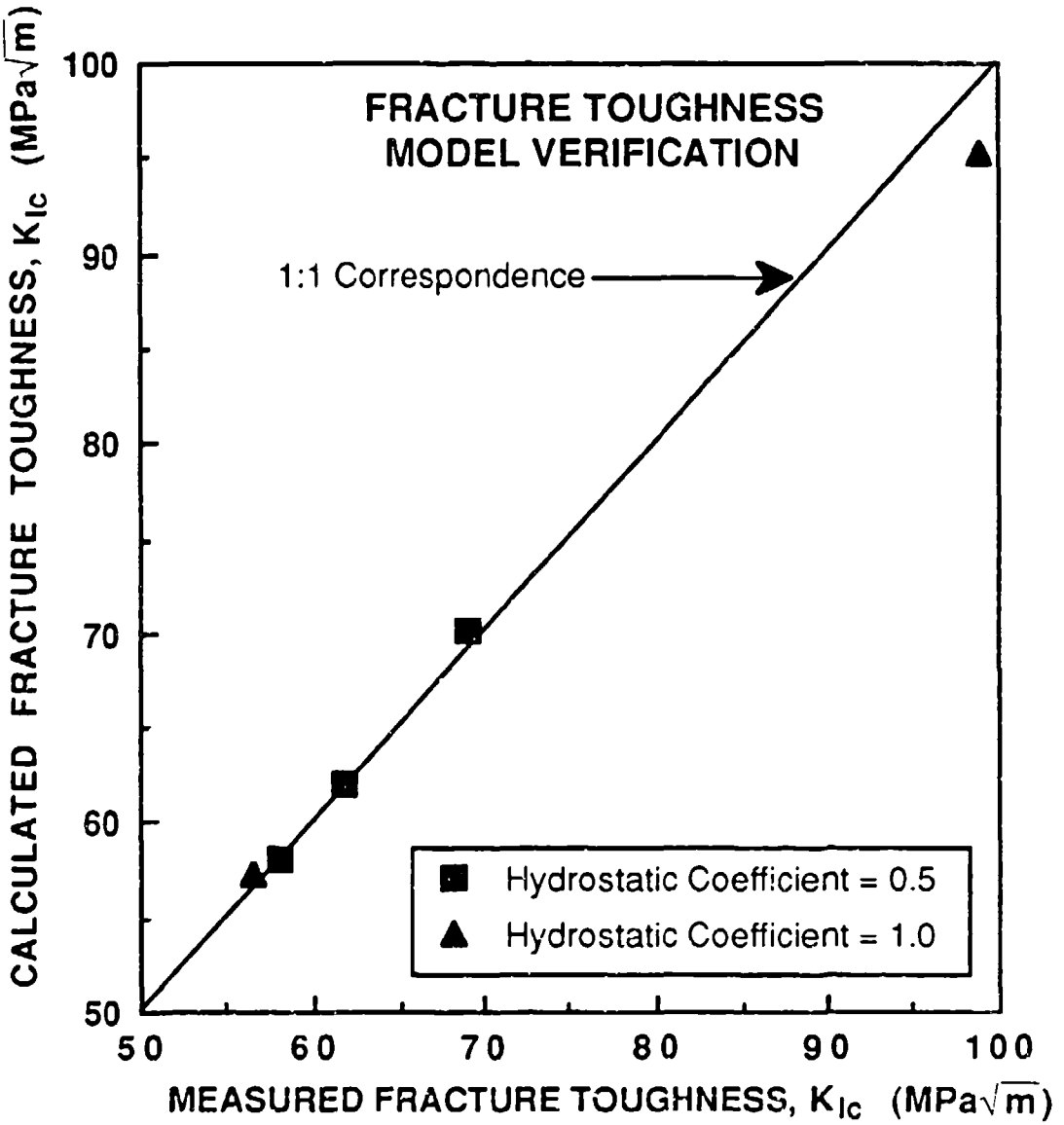

Figure 44. Fracture toughness model verification curve. The calculated K_{Ic} from the model is plotted versus the experimentally measured K_{Ic}. The line represents an ideal relationship. Deviation from the ideal is 4% or less.

TABLE VIII. FRACTURE TOUGHNESS MODEL VERIFICATION

Normalizing Temp. (°C)	Tempering Temp. (°C)	Interparticle Spacing, λ (nm)	λ/R Ratio -	Instability Strain $\varepsilon_i=\sqrt{3}\,\gamma_i$	Effective Stress, σ_E (MPa)	Hydrostatic Coefficient c
845	200	261	6.7	0.485	2120	0.5
925	200	217	8.2	0.606	2127	0.5
1010	200	242	6.0	0.381	2075	1.0
1095	200	178	7.1	0.572	2179	0.5
845	650	183	3.6	4.040	1195	1.0

$\nu = 0.3$ and $E = 206850$ MPa

TABLE IX. FRACTURE TOUGHNESS COMPARISON

Normalizing Temp. (°C)	Tempering Temp. (°C)	Calculated K_{IcC}(MPa$\sqrt{m}$)	Measured K_{IcM}(MPa$\sqrt{m}$)	K_{IcC}/K_{IcM} Error (Δ %)
845	200	62.1	61.8	-0.5
925	200	70.1	69.1	-1.4
1010	200	57.3	56.4	-1.6
1095	200	58.1	58.1	0.0
845	650	95.3	99.0 ‡	+3.9

‡ From Hickey and Thomas [76]

Mode I - Mode II Fracture Toughness Comparisons

Mode II (shear) fracture toughness tests were performed as described in the Experimental Procedure section of this study. Two tests were performed for each material. The mean K_{IIc}'s as well as the standard deviations are reported in Table X. The square root of the second-phase particle spatial relationship term ($\sqrt{\lambda/R}$) multiplied by the square root of the interparticle spacing ($\sqrt{\lambda}$), defined as the critical distance ($\lambda/\sqrt{R}$), displayed a relatively good linear relationship with toughness (K_{IIc}), as illustrated in Figure 45. The K_{IIc} - $\lambda/\sqrt{R}$ linear relationship can be extrapolated back to zero toughness ($K_{IIc}= 0$) at zero particle spacing ($\lambda/\sqrt{R} = 0$) making excellent physical sense.

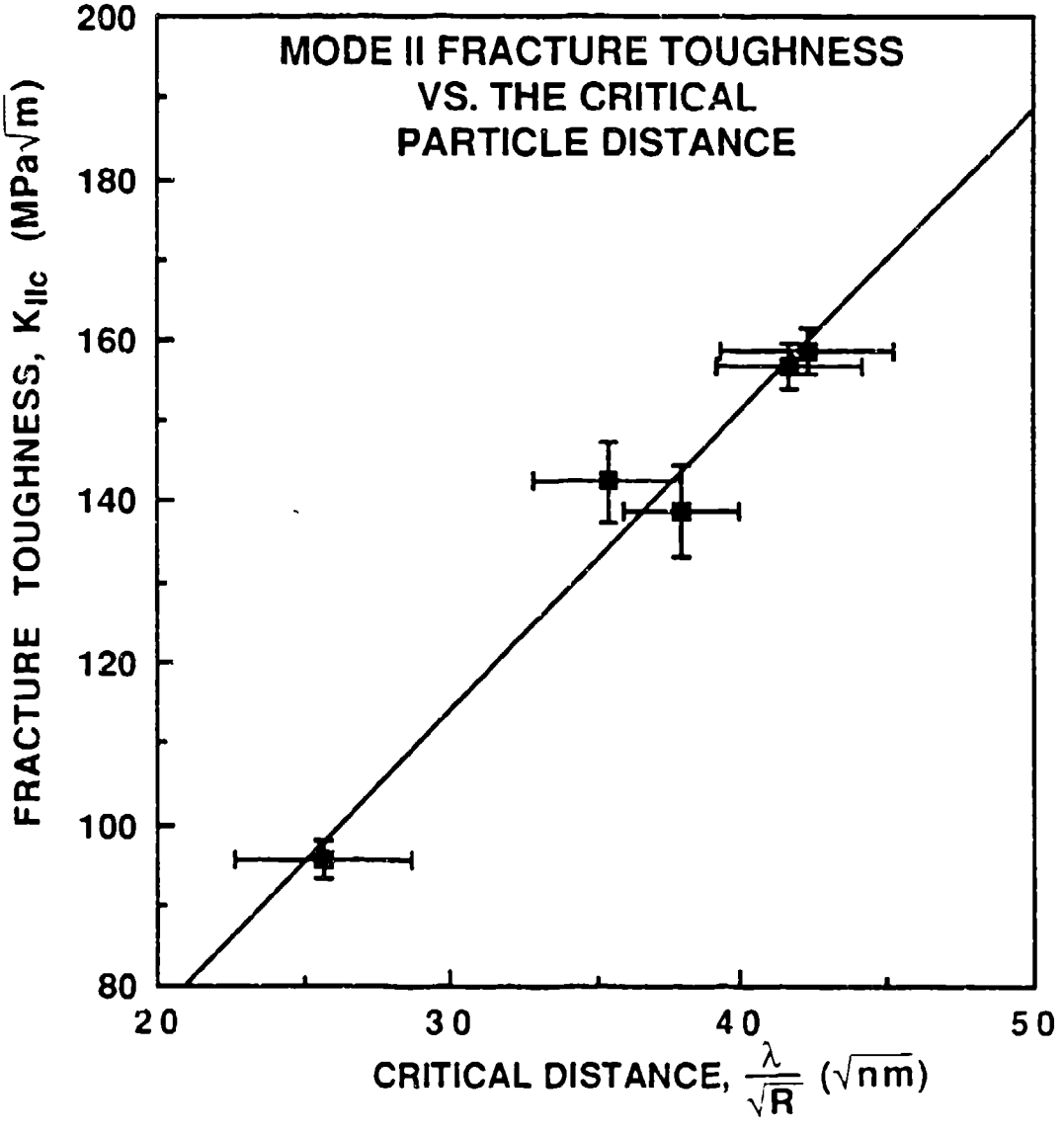

Figure 45. Critical stress intensity factor K_{IIc} plotted as a function of the critical particle distance $\lambda/\sqrt{R}$.

The mode II critical stress intensity factors are much greater than those for mode I (tension) by an average factor of about 2.5 for the UHS steels. This helps explain why the crack prefers to propagate under a tensile stress rather than shear stress even when the applied loading configuration is shear. Figure 46 shows a crack which ran 70° off the initial crack plane toward the tensile leg of the shear fracture specimen. Constraint is critical when fracturing in mode II. For the lower strength material (650°C temper), the K_{IIc}/K_{Ic} ratio is unity, owing to the large amount of void growth and coalescence during mode I fracture, raising the apparent fracture toughness.

TABLE X. MODE II (SHEAR) FRACTURE TOUGHNESS

Normalizing Temp. (°C)	Tempering Temp. (°C)	K_{IIc} (MPa $\sqrt{m}$)	K_{IIc}/K_{Ic} Ratio
845	200	156.8 ± 1.7	2.5
925	200	158.6 ± 2.7	2.3
1010	200	139.0 ± 5.7	2.5
1095	200	142.4 ± 5.0	2.5
845	650	95.5 ± 2.2	1.0

A fractographic analysis was performed on modes I and II fracture surfaces. In general, the mode II fracture mechanism was microvoid sheeting, whereas the mode I fracture mechanism was also microvoid sheeting but with some void growth at the larger particles. Some intergranular cleavage was also observed on the mode I fracture surfaces which would tend to lower K_{Ic}. Figures 47 through 50 compare the fracture morphologies for each material and fracture mode. From the mode II fracture surfaces, it was observed that the microvoid diameters scale with the interparticle spacing. Specimens with large interparticle spacings have large microvoid diameters, and the contrary is also true.

Figure 46. A mode II fracture specimen which failed by a crack running 70° off the initial crack plane toward the tensile leg of the specimen.

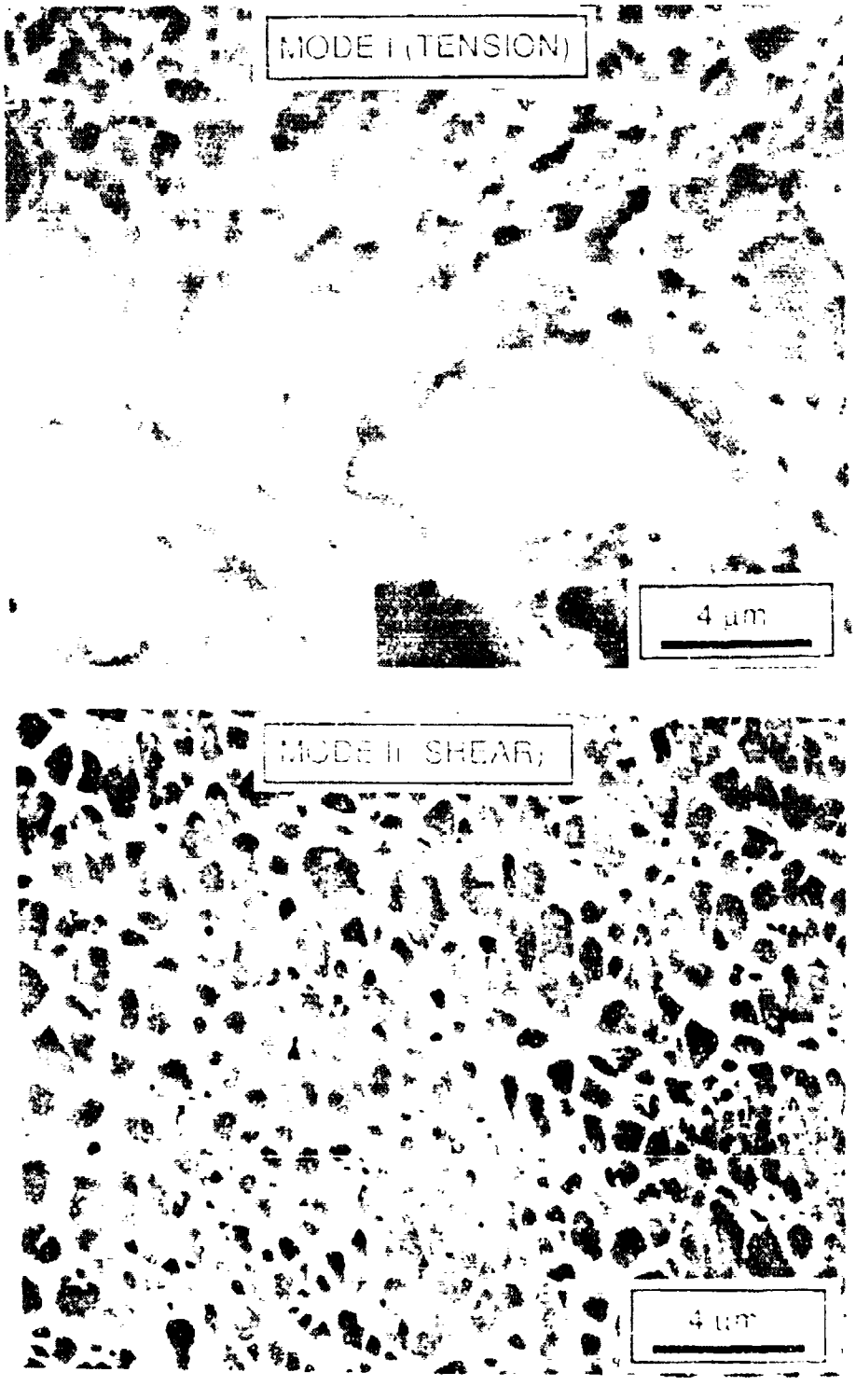

Figure 47. SEM photographs of the fracture surfaces created by mode I and mode II fracture specimens. The material is VAR 4340 steel normalized at 845°C, austenitized at 845°C and tempered at 200°C.

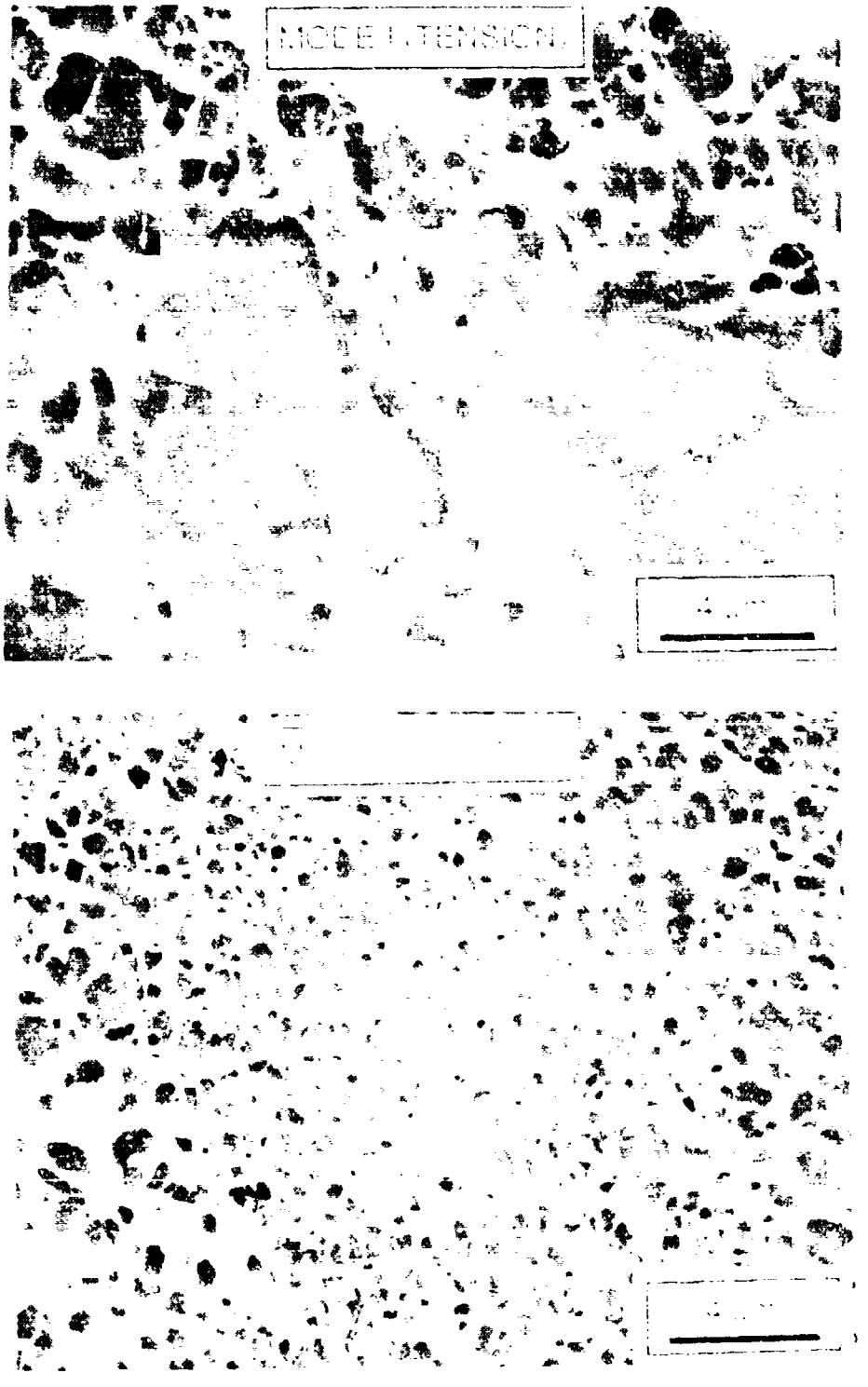

Figure 48. SEM photographs of the fracture surfaces created by mode I and mode II fracture specimens. The material is VAR 4340 steel normalized at 925°C, austenitized at 845°C and tempered at 200°C.

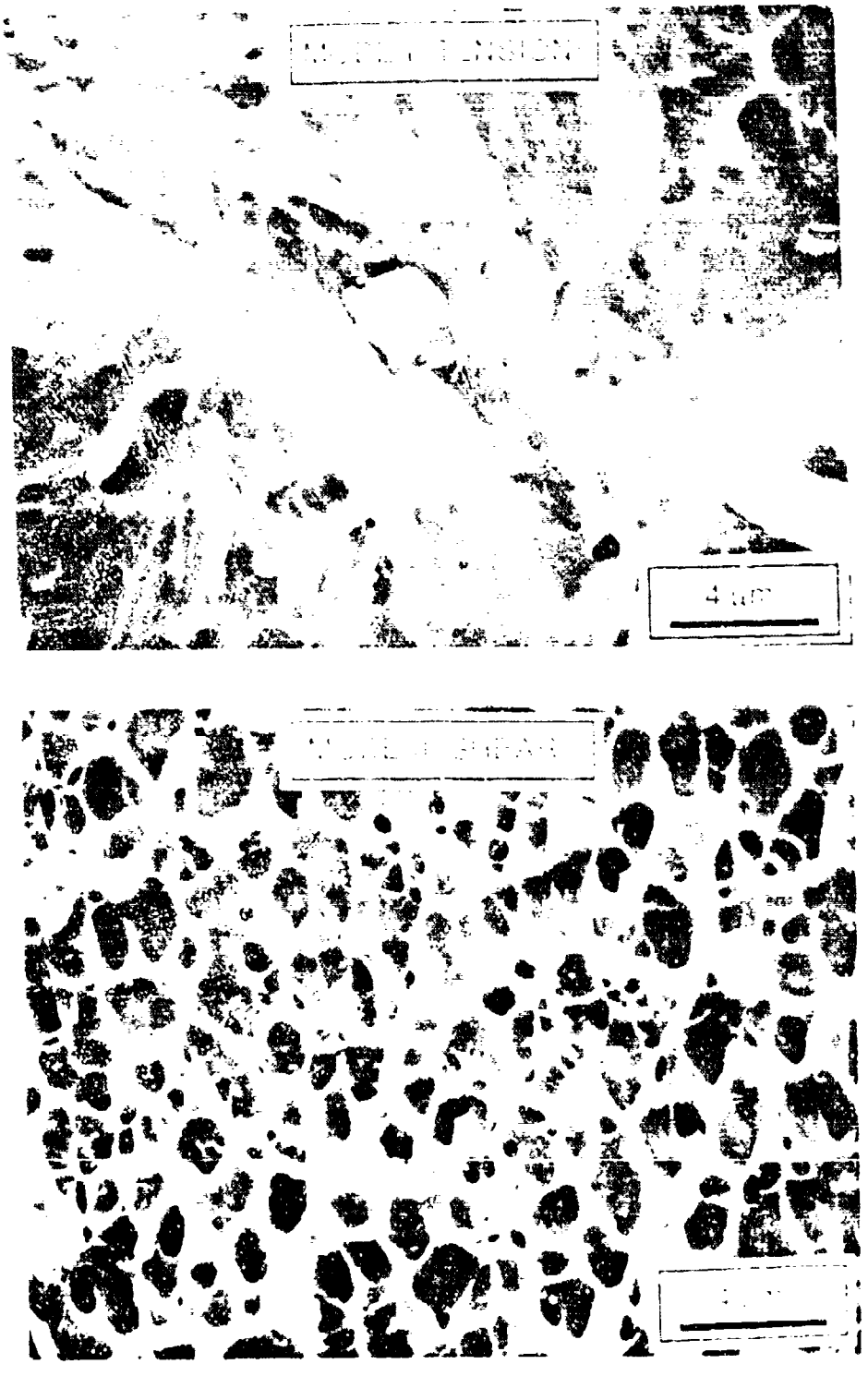

Figure 49. SEM photographs of the fracture surfaces created by mode I and mode II fracture specimens. The material is VAR 4340 steel normalized at 1010°C, austenitized at 845°C and tempered at 200°C.

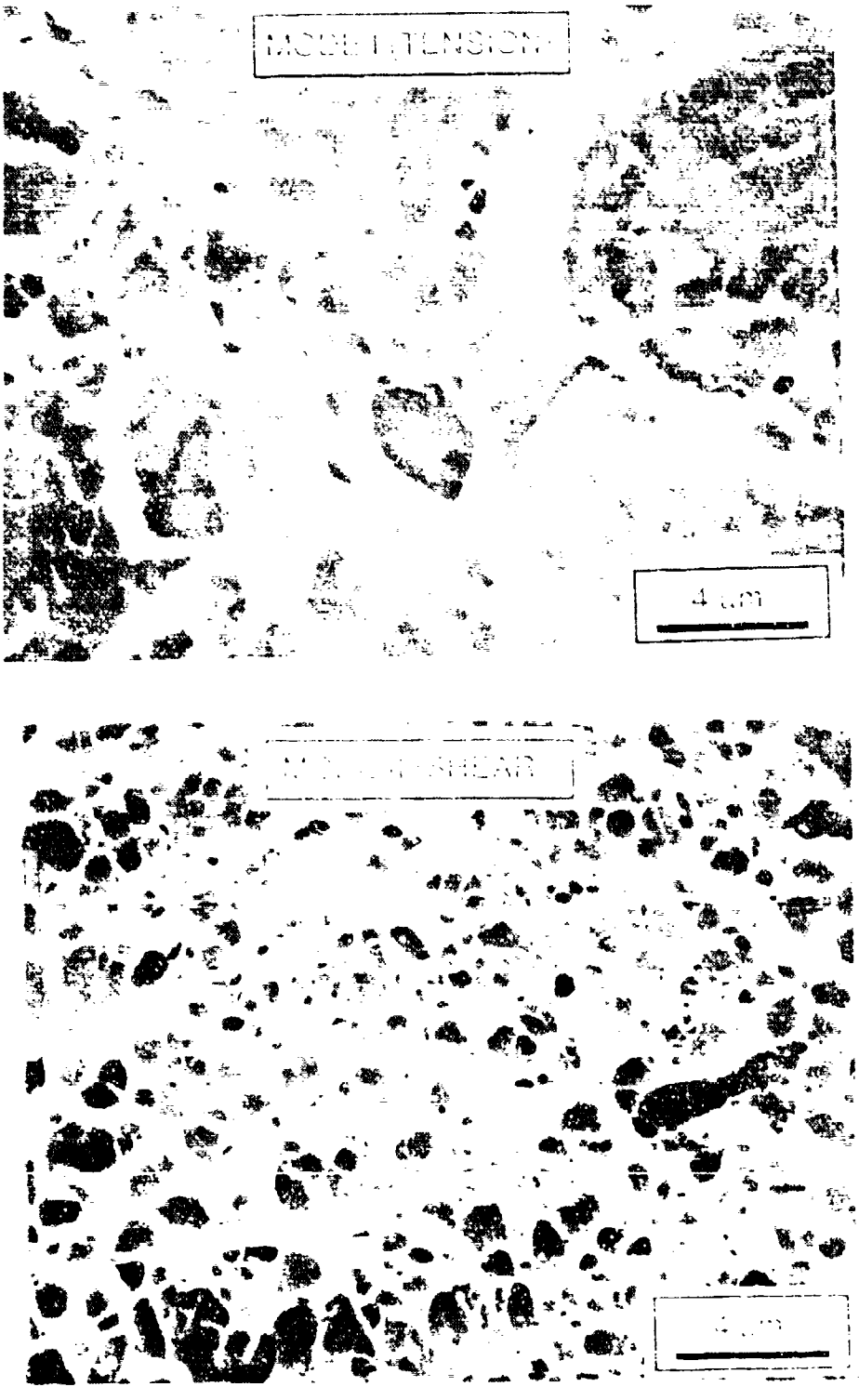

Figure 50. SEM photographs of the fracture surfaces created by mode I and mode II fracture specimens. The material is VAR 4340 steel normalized at 1095°C, austenitized at 845°C and tempered at 200°C.

There existed only small dimples on the mode II fracture surfaces due to a microvoid nucleation fracture mechanism. The mode II stress state consists of a high hydrostatic compression in addition to the shear stress. This pressure permits the development of large strains before the void nucleation event. Consequently, void nucleation at all particles occurs virtually simultaneously, resulting in rapid plastic failure by a microvoid sheeting fracture mechanism.

Whereas, there existed a mixed distribution of dimple sizes on the mode I fracture surfaces due to a void growth fracture mechanism. The hydrostatic tension stress field favors early void nucleation at the relatively large particles with weak matrix-particle interfaces. Subsequent growth and coalescence of these voids are favored with this tensile stress state.

A possible solution for the large K_{IIc}/K_{Ic} ratio and fracture surface morphology discrepancies may be found in the first approximation calculations of the crack tip stress fields detailed in Appendix C. The normalization of the hydrostatic stresses by their respective effective stresses (σ_H/σ_E) provides a reasonable solution to the discrepancy as illustrated in Figure 51. These stress calculations clearly demonstrate a high hydrostatic tension field exists just in front (0°) of the crack tip during mode I testing. However, during mode II testing, zero hydrostatic tension exists just in front (0°) of the crack tip. Needleman [75] in a series of calculations, demonstrated that high σ_H/σ_E ratios produce lower void nucleation strains. He concluded that the critical nucleation stress is inversely dependent on the hydrostatic tension, but with a coefficient that is less than or equal to unity.

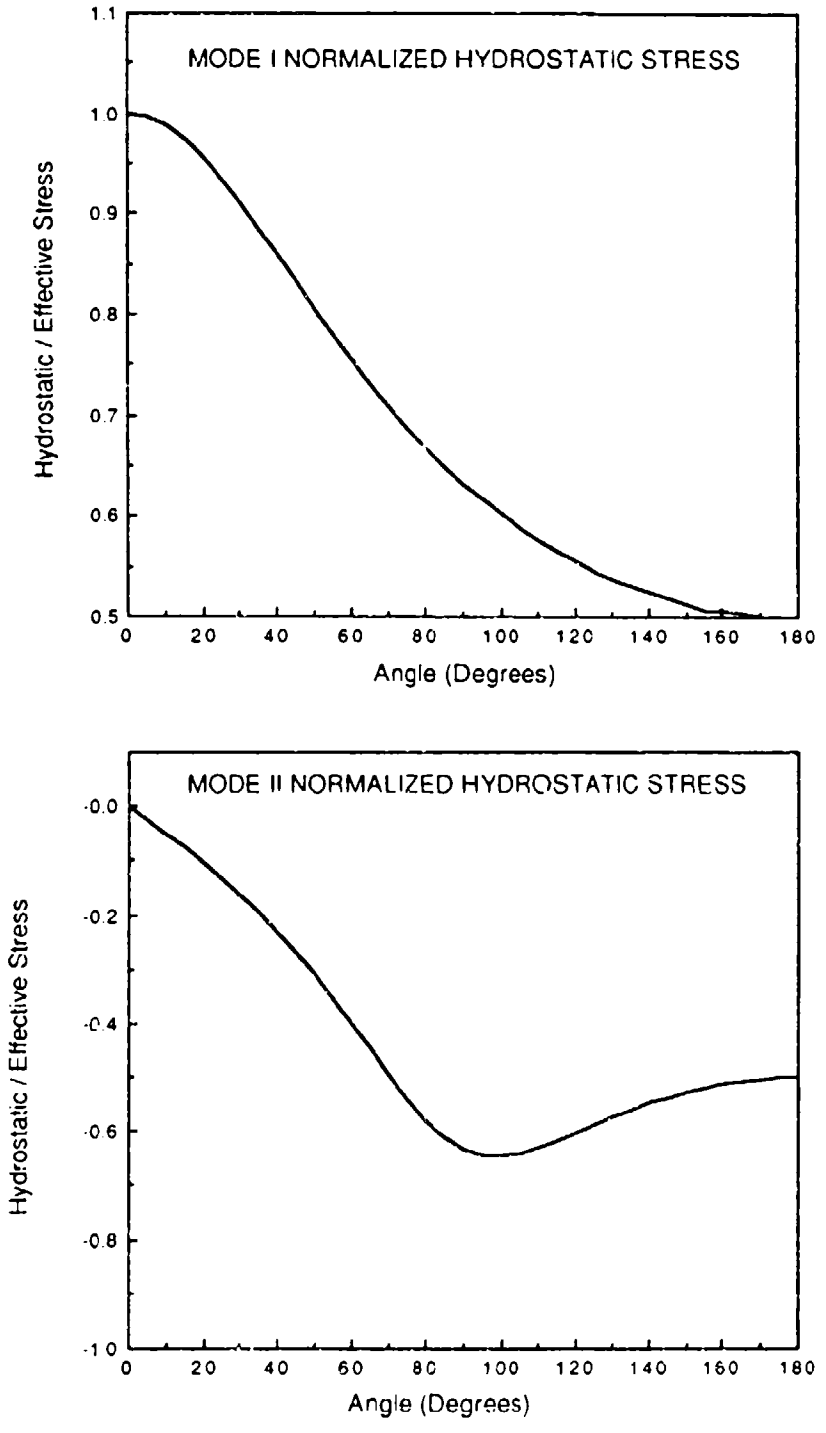

Figure 51. Comparison of normalized hydrostatic stresses around a crack tip for fracture modes I and II. The hydrostatic stress σ_H is normalized by the effective stress σ_E. Mode I fracture exhibits a high hydrostatic tension just in front (0°) of the crack tip. Whereas, mode II exhibits zero hydrostatic tension at 0°.

The lower strength material (650°C temper) was also fractured in shear. The fracture surface of this specimen contained greatly elongated microvoids indicative of greater matrix strain hardening (Figure 52). In the same manner as the UHS steel, The lower strength steel's microvoid diameters scale with the interparticle spacing. The K_{IIc}/K_{Ic} ratio equal to unity for this material indicates that there is little effect of hydrostatic stress on void nucleation around cementite particles, as there was relatively little influence of axial pressure on shear instability strain (See Figure 34).

A process zone was observed within the larger mode II plastic zone (Figures 53-56). This process zone extended only a very small fraction of the way into the plastic zone. The fracture morphology was somewhat different than in the rest of the plastic zone (compare Figures 53-56 to Figures 47-50). This fracture surface is a combination of dimple rupture and a structure with a wave-like appearance attributed to adiabatic shear which has been called a "knobbly" structure by Bedford *et al.* [6]. It is speculated that these fracture surfaces are the result of microvoid sheeting in a region of extreme plastic strain resulting from a stress field of intense effective stress combined with high hydrostatic pressure.

Mode II Fracture Toughness Model

A similar analytical model was derived for mode II, relating the material parameters to the critical stress intensity factor. The form of the fracture toughness equation relating the fracture toughness (K_{IIc}) to experimentally derived parameters is identical to that of mode I. However, the stress states are totally different. The effective stress for mode II is 1.73 times the mode I effective stress, while the mode II hydrostatic stress is less than or equal to zero for all crack plane orientations (see Appendix C).

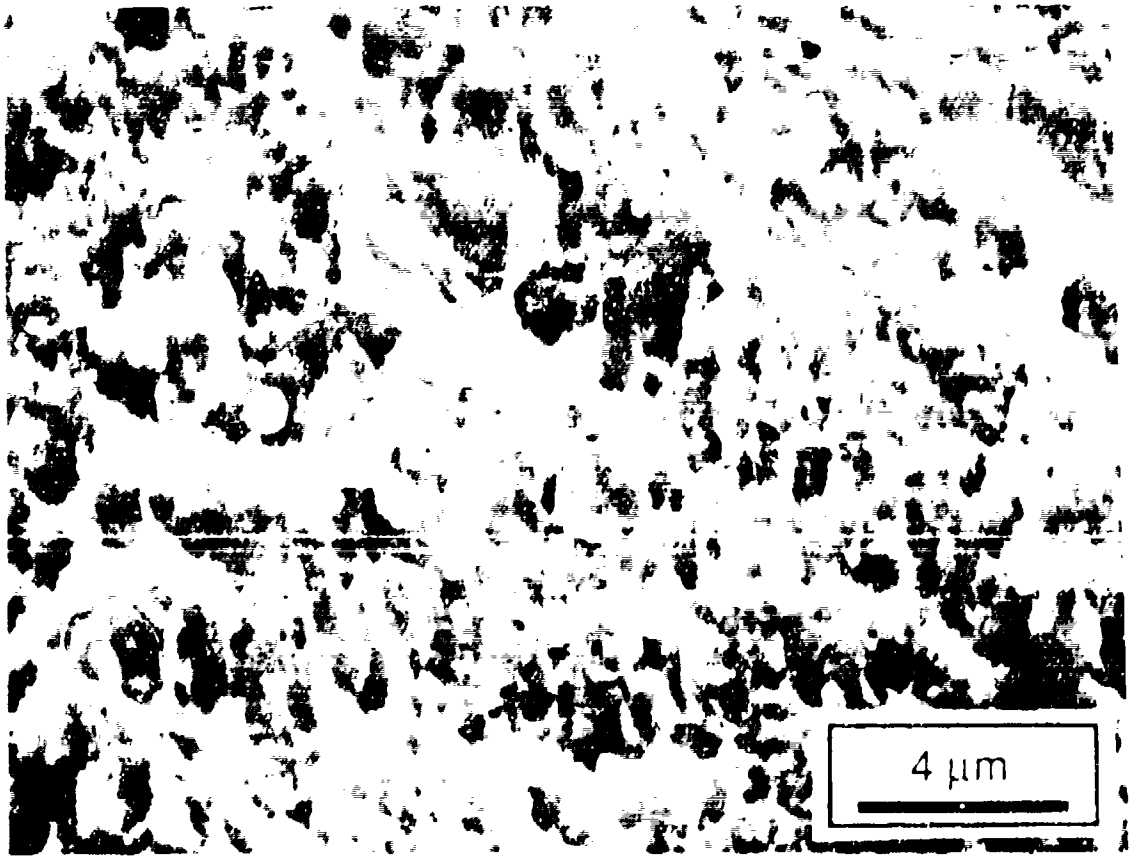

Figure 52. SEM fractograph of the fracture surface created by a K_{IIc} specimen. The material is VAR 4340 steel normalized at 845°C, austenitized at 845°C and tempered at 650°C.

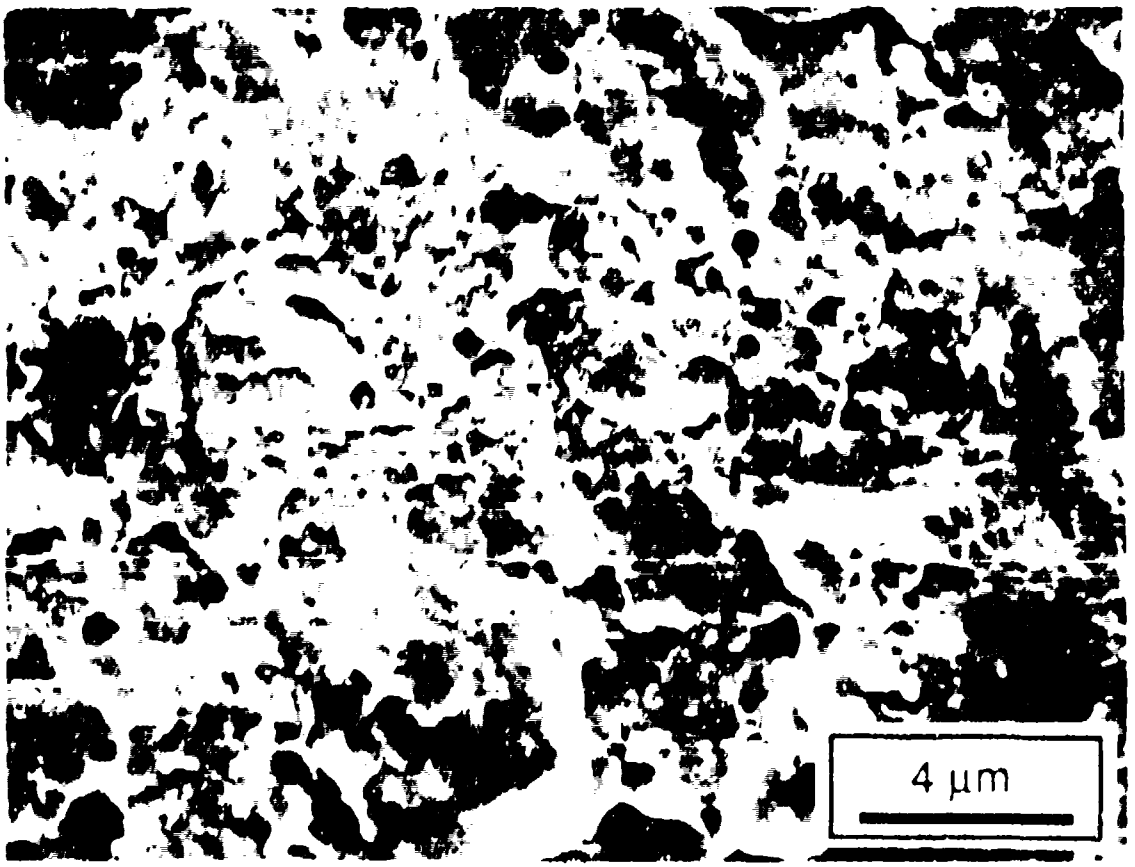

Figure 53. SEM fractograph of the fracture surface created by the K_{IIc} process zone immediately in front of the fatigue precrack. The material is VAR 4340 steel normalized at 845°C, austenitized at 845°C and tempered at 200°C.

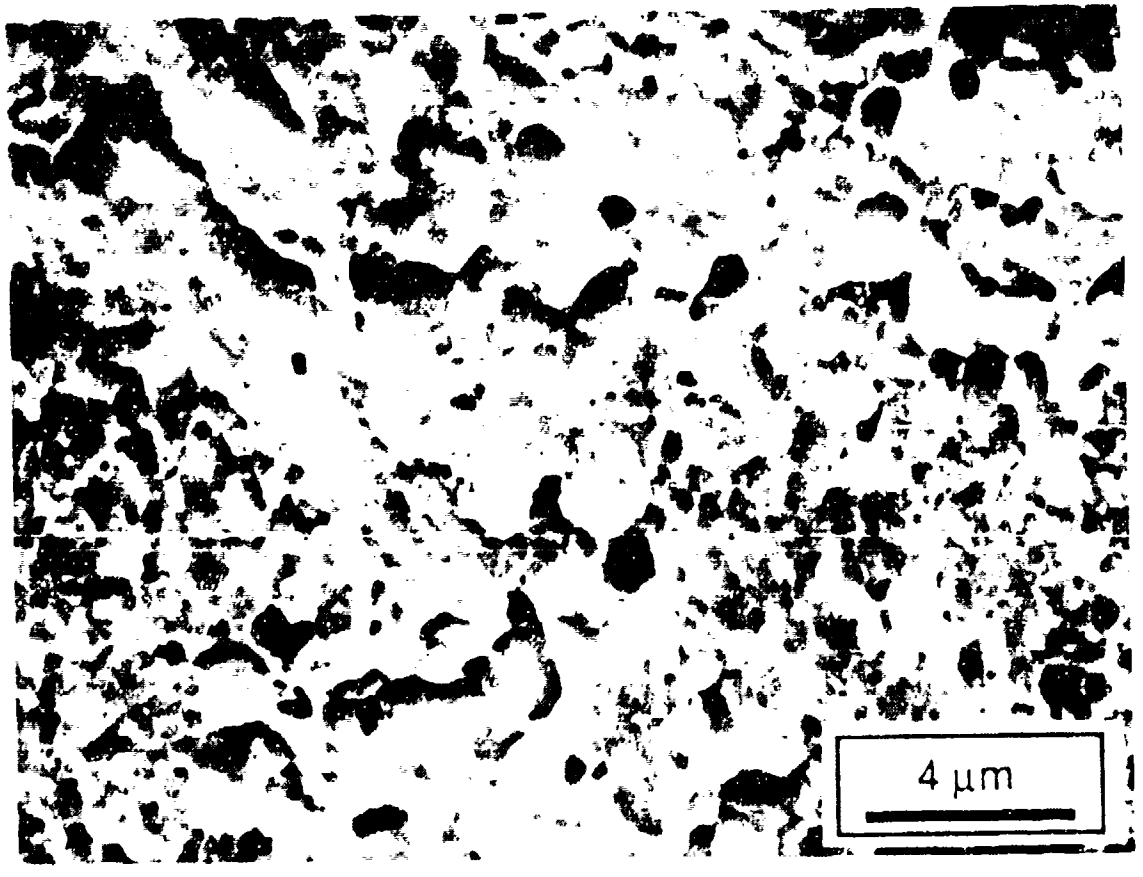

Figure 54. SEM fractograph of the fracture surface created by the K_{IIc} process zone immediately in front of the fatigue precrack. The material is VAR 4340 steel normalized at 925°C, austenitized at 845°C and tempered at 200°C.

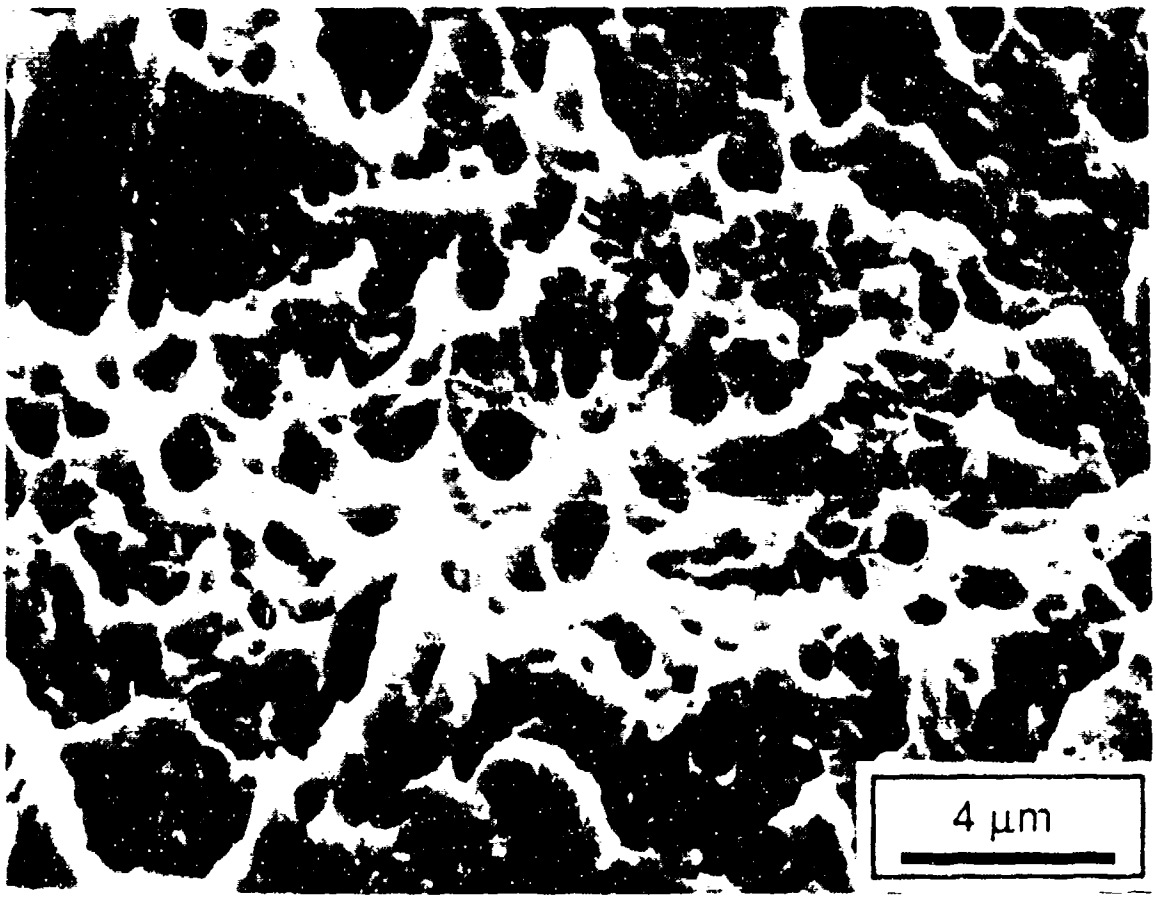

Figure 55. SEM fractograph of the fracture surface created by the K_{IIc} process zone immediately in front of the fatigue precrack. The material is VAR 4340 steel normalized at 1010°C, austenitized at 845°C and tempered at 200°C.

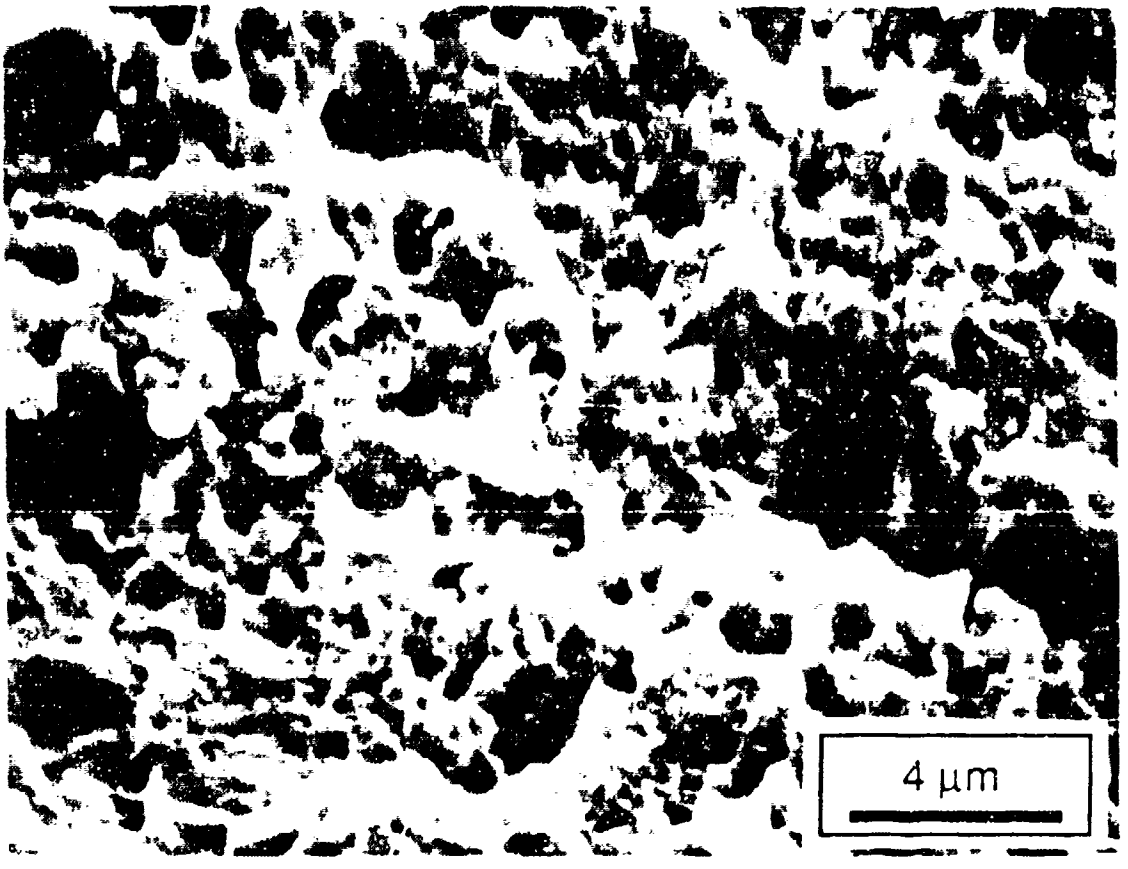

Figure 56. SEM fractograph of the fracture surface created by the K_{IIc} process zone immediately in front of the fatigue precrack. The material is VAR 4340 steel normalized at 1095°C, austenitized at 845°C and tempered at 200°C.

After calculating the mode II fracture toughness using the appropriate parameters in the model, it was found that these calculated K_{IIc}'s fell short of the actual experimentally determined values by a factor of approximately 2.3. A reasonable explanation for this discrepancy lies in the effect of pressure on shear instability. Figures 33 and 34 illustrate the dependence of shear instability on pressure.

For the case of the ultrahigh strength material (Figure 33), an axial stress equal to 1/3 the tensile yield stress increases the instability strain by a factor of approximately 4. In addition, this axial pressure converts to a much lower hydrostatic compressive stress; *i.e.*, σ_H = 1/9 the tensile yield strength. These low hydrostatic compressive stresses are operative very close to the 0° crack plane orientation (See Appendix C). Consequently, the shear instability strain measurements from the zero pressure shear tests cannot be used in the mode II fracture toughness model. In order for the model to accurately predict K_{IIc}, instability strain values from biaxially loaded (shear + axial pressure) test specimens must be substituted for the γ_i's measured from shear tests employing no applied axial stress. Experimentally measured K_{IIc}'s would be approximately equivalent to model predictions of K_{IIc}'s using γ_i's measured under a hydrostatic stress approximately equal to 14% of the material's tensile yield stress.

CONCLUSIONS

1. Shear instability strain (γ_i) directly correlated with second-phase particles size and distribution through a dimensionless term (λ/R) relating the interparticle spacing (λ) to the geometric mean particle radius (R).

2. Aluminum nitride and cementite particles were the most embrittling particles observed, responsible for low fracture toughness and loss of ductility.

3. Shear localization is produced by a microvoid nucleation softening mechanism. Microvoids nucleate at sub-micron scale second-phase particles.

4. The pressure dependent behavior of shear instability provides evidence of a microvoid nucleation softening mechanism.

5. There is little effect of deformation heating produced thermal softening influencing the instability strain for the UHS steel.

6. Both mode I (K_{Ic}) and mode II (K_{IIc}) critical stress intensity factors directly correlate with the critical particle distance ($\lambda/\sqrt{R}$).

7. A fracture toughness model was derived first principles. Excellent correlation exists between measured and calculated critical mode I stress intensity factors (K_{Ic}) for the different steels investigated in this study. Measured and calculated K_{IIc}'s did not correlate very well due to the influence of hydrostatic compression on the shear instability strain. The model result is described in detail in the Fracture - Shear Instability Correlations section. For emphasis, the end product is once again given

$$K_c = \sqrt{\frac{2\pi}{(1-\upsilon^2)} \left(\frac{\lambda}{R}\right) \lambda \, \varepsilon_i \, E \, (\sigma_E + c \, \sigma_H)}$$

8. Mode II (shear) critical stress intensity factors (K_{IIc}) were 2.5 times greater than mode I (tension) critical stress intensity factors (K_{Ic}). This discrepancy is probably due to the differing stress states. Mode I crack tips experience high hydrostatic tension, whereas mode II crack tips have zero or negative hydrostatic tension, which affects the void nucleation stress.

REFERENCES

1. M. Azrin, J. G. Cowie, and G. B. Olson, Shear Instability Mechanisms in High Hardness Steel, *Annals of Israel Physical Society, V.8, Fragmentation, Form and Flow in Fragmented Media* (1986), pp. 409-417, also *U.S. Government Report No. MTL TR 87-2*.

2. J. G. Cowie, M. Azrin, and G. B. Olson, Microvoid Formation During Shear Deformation of Ultrahigh Strength Steels, *Proceedings of the Thirty-fourth Sagamore Army Materials Research Conference* (1987), in press.

3. J. Mescall, and R. Papirno, Spallation in Cylinder - Plate Impact, *Exp. Mech.*, V.9 (1979), pp. 283-311.

4. H. Rogers, Adiabatic Shearing: A Review, *Drexel University Report* prepared for the U.S. Army Research Office (1974).

5. H. Rogers, Adiabatic Plastic Deformation, *Ann. Rev. Mater. Sci.*, V. 9 (1979), pp. 283-311.

6. A. Bedford, A. Wingrove, and K. Thompson, The Phenomenon of Adiabatic Shear Deformation, *J. Aust. Inst. Metals*, V. 19, no. 1 (1974), pp. 61-74.

7. R. Clifton, Adiabatic Shear Banding, in *Materials Response to Ultra High Loading Rates*, Chap. 8, National Materials Advisory Board Committee, Rep. No. NMAB-356 (1980), pp. 129-142.

8. A. Argon, Stability of Plastic Deformation, in *The Inhomogeneity of Plastic Deformation*, Chap. 7, ASM, Metals Park, OH (1973), pp. 161-189.

9. L. Samuels, and I. Lamborn, Failure Analysis of Armament Hardware, in *Metallography in Failure Analysis*, J. McCall and P. French, eds., Plenum Press, NY (1978), pp. 167-190.

10. G. Olson, J. Mescall, and M. Azrin, Adiabatic Deformation and Strain Localization, in *Shock Waves and High-Strain-Rate Phenomena in Metals*, M. Meyers and L. Murr, eds., Plenum Press, NY (1981), Chapt. 14.

11. T. Walker, and M. Shaw, On Deformation at Large Strains, in *Advances in Machine Tool Design and Research*, S. Tobias and F. Koenigsberger, eds., Pergamon Press, NY 91969), p. 241.

12. H. Luong, Discontinuities and Their Effects on Work Materials in Chip Formation, in *Proceedings of the Australian Conference on Manufacturing Engineering*, Monash University, Victoria, Australia (1977), p. 122.

13. J. G. Cowie, and F. R. Tuler, Flow Localization Models - A Review, *Materials Science and Engineering*, V.95 (1987), pp. 93-99.

14. L. Anand, Some Experimental Observations on Localized Shear Bands in Plane-Strain, *Scr. Metall.*, V. 18 (1984) pp. 423-427.

15. J. W. Hutchinson, Introduction to the Viewpoint Set on Shear Bands, *Scr. Metall.*, V. 18 (1984) 421-42[illegible].

16. S. L. Semiatin, and J. J. Jonas, *Formability and Workability of Metals: Plastic Instability and Flow Localization*, ASM, Metals Park, OH (1984), pp. 51-54, 68-69, 110.

17. H. G. Baron, *Journal of the Iron Steel Institute*, V. 182, no. 1 (1956), p. 354.

18. R. S. Culver, Thermal Instability Strain in Dynamic Plastic Deformation, in *Metallurgical Effects at High Strain Rates*, R. W. Rohde, B. M. Butcher, J. R. Holland, and C. H. Karnes eds., TMS-AIME, Plenum Press, NY (1973), pp. 519-530.

19. M. R. Staker, The Relation Between Adiabatic Shear Instability Strain and Materials Properties, *Acta Metall.*, V. 29 (1981), pp. 683-689.

20. R. J. Clifton, J. Duffy, K. A. Hartley, and T. G. Shawki, On Critical Conditions for Shear Bands Formation at High Strain Rates, *Scr. Metall.*, V. 18, no. 5 (1984), pp. 443-448.

21. R. J. Asaro, and A. Needleman, Flow Localization in Strain Hardening Crystalline Solids, *Scr. Metall.*, V. 18, no. 5 (1984), pp. 429-435.

22. J. Hutchinson and V. Tvergaard, *Int. J. Solids Structures*, V. 17 (1981) p.451.

23. M. Saje, J. Pan, and A. Needleman, Void Nucleation Effects on Shear Localization in Porous Plastic Solids, *Int. J. Fracture*, V. 19 (1982) pp.163-182.

24. J. R. Rice, in *Theoretical and Applied Mechanics, Proc. 14th IUTAM Congr., Delft, August 30 - September 4, 1976*, W. T. Koiter, ed., North Holland Amsterdam (1977), pp. 207.

25. J. W. Hutchinson, and V. Tvergaard, *Research Report, Mech-16*, Division of Applied Science, Harvard University, Cambridge, MA (1980).

26. J. Pan, M. Saje, and A. Needleman, Localization of Deformation in Rate Sensitive Porous Plastic Solids, *Int. J. Fracture*, V. 21 (1983) p. 261.

27. V. Tvergaard, Ductile Fracture by Cavity Nucleation Between Larger Voids, *J. Mech. Phys. Solids*, V. 30, no. 4 (1982), pp 265-286.

28. C. A. Berg, in *Inelastic Behavior of Solids*, M. F. Kanninen, W. F. Adler, A. R. Rosenfield, and R. I. Jaffee, eds., McGraw-Hill, NY, 1970, p. 171.

29. V. Tvergaard, Influence of Void Nucleation on Ductile Shear Fracture at a Free Surface, *J. Mech. Phys. Solids*, V. 30, no. 6 (1982), pp. 399-425.

30. L. Anand, and W. A. Spitzig, Initiation of Localized Shear Bands in Plane Strain, *J. Mech. Phys. Solids*, V. 28 (1980), pp. 113-128.

31. A. Needleman, and J. Rice, in *Mechanics of Sheet Metal Forming*, D. P. Koistinen, and N. M. Wang, eds., Plenum Press, NY, 1978, p. 237.

32. A. S. Argon, J. Im, and R. Safoglu, Cavity Formation Inclusions in Ductile Fracture, *Metall. Trans. A*, V. 6 (1975), pp. 825-837.

33. A. S. Argon, and J. Im, Separation of Second Phase Particles in 1045 steel in Plastic Straining, *Metall. Trans. A*, V. 6 (1975), pp. 839-851.

34. O. A. Onyenwuenyi, Microstructural Aspects of Flow Localization and Plastic Instability, *Scr. Metall.*, V. 18 (1984), pp. 455-458.

35. O. A. Onyenwuenyi, and J. P. Hirth, Plastic Instability in U-Notched Bend Specimens of Spheroidized AISI 1090 Steel, *Metall. Trans. A*, Vol. 13 (1983), p.2209.

36. O. A. Onyenwuenyi, and J. P. Hirth, Effects of Hydrogen on Notch Ductility and Fracture in Spheroidized AISI 1090 Steel, *Metall. Trans. A*, Vol. 14 (1983), p.259.

37. A. Needleman, and V. Tvergaard, Crack Tip Stress and Deformation Fields with a Solid Vertex in Its Yield Surface, *Brown University, Tech. Report 87*, November (1981).

38. K.-H. Schwalbe, On the Influence of Microstructure on Crack Propagation Mechanisms and Fracture Toughness of Metallic Materials, *Eng. Fracture Mech.*, V. 9 (1977), pp. 795-832.

39. R. C. Bates, Mechanics and Mechanisms of Fracture, in *Metallurgical Treatises*, J. K. Tien, and J. F. Elliot, eds., AIME, NY, 1981.

40. P. K. Fleyshman, Fracture Toughness of Rapidly Solidified High Strength Steels, *S.M. Thesis*, Massachusetts Institute of Technology, Cambridge, MA (1982).

41. H. Yamamoto, Conditions of Shear Localization in the Ductile Fracture of Void-Containing Materials, *Int. J. of Fracture*, V. 14 (1978), p. 347.

42. M. Saje, J. Pan, and A. Needleman, Void Nucleation Effects on Shear Localization in Porous Plastic Solids, *Int. J. Fracture*, V. 19 (1982) pp.163-182.

43. J. Pan, M. Saje, and A. Needleman, Localization of Deformation in Rate Sensitive Porous Plastic Solids, *Int. J. Fracture*, V. 21 (1983) p. 261.

44. G. Y. Lai, W. E. Wood, R. A. Clark, V. F. Zackey, and E. R. Parker, The Effects of Austenitizing Temperatures on the Microstructure and Mechanical Properties of As-Quenched 4340 Steel, *Metall. Trans.*, V. 5 (1974), p. 1663.

45. R. O. Ritchie, B. Francis, and W. L. Server, Evaluation of Toughness in AISI 4340 Alloy Steel Austenitized at Low and High Temperatures, *Metall. Trans. A*, V. 7 (1976), p.831.

46. R. O. Ritchie, and R. M. Horn, Further Considerations on the Inconsistency in Toughness Evaluation of AISI 4340 Steel Austenitized at Increasing Temperatures, *Metall. Trans. A*, V. 9, (1978), P. 331.

47. D. Firrao, J. A. Begley, G. Silva, R. Roberti, and B. De Benedetti, Radius and Austenitizing Temperatures on Fracture Appearance of As-Quenched Charpy V-Type AISI 4340 Steel Specimens, *Metall. Trans. A*, V. 13 (1982), p. 1003.

48. R. M. Fisher, Symposium Techniques in Electron Metallography, *ASTM Spec. Tech. Publ., 155:49* (1953).

49. G. F. Vander Voort, *Metallography, Principles and Practice,* McGraw-Hill, NY (1984), pp.428-432.

50. D. Tracey, and P. Perrone, Shear Specimen Stress Analysis, Presentation at the Second Annual Steel Research Group Meeting (1986), Massachusetts Institute of Technology, Cambridge, MA.

51. Standard Method of Test for Plane-Strain Fracture Toughness of Metallic Materials, *ASTM Designation E399-83, Part 10, ASTM Annual Standards*.

52. W. F. Brown, Jr., and J. E. Srawley, Plane Strain Crack Toughness Testing Of High Strength Metallic Materials, *ASTM STP 410* (1967).

53. R. J. Buzzard, B. Gross, J. E. Srawley, Mode II Fatigue Crack Growth Specimen Development, *NASA Technical Memorandum 83722*, NASA Lewis Research Center, Cleveland, OH (1984).

54. N. Iosipescu, *Journal of Materials*. V. 2, no. 3 (1967), pp. 537-566.

55. H. A. Richard, A New Compact Shear Specimen, *International Journal of Fracture,* V. 17 (1981), pp. R105-R107.

56. D. L. Jones, D. B. Chisholm, *Engineering Fracture Mechanics,* V. 7, June (1975), pp. 261-270.

57. M. Arcan, Z. Hasin, and A. Voloshin, *Experimental Mechanics*, V. 18, April (1978), pp. 141-146.

58. K. R. Raju, On the Sliding Mode Stress Intensity Factors for Three-Point Bend K_{II} Specimen and Mode II Fracture Toughness, *International Journal of Fracture*, V. 17 (1981), pp. R193-197.

59. J. Watkins, Fracture Toughness Test for Soil-Cement Samples in Mode II, *International Journal of Fracture*, V. 23 (1983), pp. R135-138.

60. R. J. Buzzard, Experimental Compliance Calibration of the NASA Lewis Research Center Mode II Fatigue Specimen, *NASA Technical Memorandum 86908* (1985).

61. T. Gladman, The Effect of Aluminum Nitride on the Grain Coarsening Behavior of Austenite, in *Metallurgical Developments in Carbon Steels*, Special Report 81, The Iron and Steel Institute, London (1963), pp. 68-70.

62. Metal Test Methods, *ASTM Designation E112-63*, Part 3, American Society for Testing and Materials, ASTM Annual Standards.

63. G. Krauss, *Principles of Heat Treatment of Steels*, American Society for Metals, Metals Park, OH (1980), pp. 176-226.

64. M. Gore, G. Olson, and M Cohen, Particle Dispersion in UHS Martensitic Steel, *Proceedings of the Thirty-fourth Sagamore Army Materials Research Conference* (1987), in press.

65. D. M. Tracey, and P. J. Perrone, Modeling of Interactions in Void Nucleation and Growth, *Proceedings of the Thirty-fourth Sagamore Army Materials Research Conference* (1987), in press.

66. J. P. Materkowski, Tempered Martensite Embrittlement in 4340 Steel As Related to Phosphorous Content and Carbide Morphology, *M.S. Thesis,* Colorado School of Mines (1978), Golden, CO.

67. N. A. Fleck, J. W. Hutchinson, and V. Tvergaard, Softening by Void Nucleation and Growth in Tension, *Harvard University Report No. MECH-123* (1988), Cambridge, MA.

68. W. F. Hosford, and R. M. Caddell, *Metal Forming, Mechanics and Metallurgy,* Prentice-Hall, Englewood Cliffs, NJ (1983), pp. 80-102.

69. Y. C. Chi, The Effects of Tempering and Test Temperatures on the Dynamic Fracture Behavior of an AISI 4340 VAR Steel, *M.S. Thesis,* Brown University, Providence, RI (1987), pp. 12, 28, and 74.

70. J. W. Hutchinson, Singular Behaviour at the End of a Tensile Crack in Hardening Material, *J. of Mech. Phys. of Solids,* V. 16 (1968), pp. 13-31.

71. J. R. Rice, and G. F. Rosengren, Plane Strain Deformation Near a Crack Tip in a Power-Law Hardening Material, *J. of Mech. Phys. of Solids,* V. 16, (1968), pp. 7-12.

72. A. S. Tetelman, and A. J. McEvily Jr., Fracture of Structural Materials, John Wiley & Sons Inc., New York (1967), pp. 234-333.

73. A. L. Gurson, Plastic Flow and Fracture Behavior of Ductile Materials Incorporating Void Nucleation, Growth and Interaction, *Ph.D. Thesis,* Brown University, Providence, RI (1975).

74. A. L. Gurson, Continuum Theory of Ductile Rupture by Void Nucleation and Growth; Part I: Yield Criterion and Flow Rules for Porous Ductile Materials, *J. Engr. Mat. Tech.*, V. 27 (1977), pp. 2-15.

75. A. Needleman, A Continuum Model for Void Nucleation by Inclusion Debonding, *J. of Applied Mechanics*, V. 54 (1987), pp. 525-531.

76. C. F. Hickey, and T. S. Thomas, Comparing a Split Heat of ESR/VAR 4340 Steel, *Metal Progress*, Oct. (1985).

APPENDIX

Appendix A - Prior Austenite Grain Size Determination

Calculation of the grain sizes was performed using the line intercept method. These data were then converted into the appropriate ASTM grain size number. The average grain diameter was calculated as follows:

$$D = \frac{\Sigma \text{ (length of lines)}}{\Sigma \text{ (number of grain boundary intersections)}}$$

where D is the measured average grain diameter at the magnification of the photograph. To convert to the ASTM grain size number, the following relations were employed

$$n = 2^{N-1}$$

$$\text{or} \quad N = \frac{\log n}{\log 2} + 1$$

where n is the number of grains per square inch, and N is defined as the ASTM grain size number.

Table A presents the grain size measurement data. The ASTM grain size averages 12.1 ± 0.5 for the four normalizing temperatures. It can be concluded that the final austenitizing treatment at 845°C for 15 min determined the final austenite size. There is however a slight increase in grain size with increasing normalizing temperature, illustrated in Figures A1-A4, due to the dissolution of some of the grain refining second phase particles.

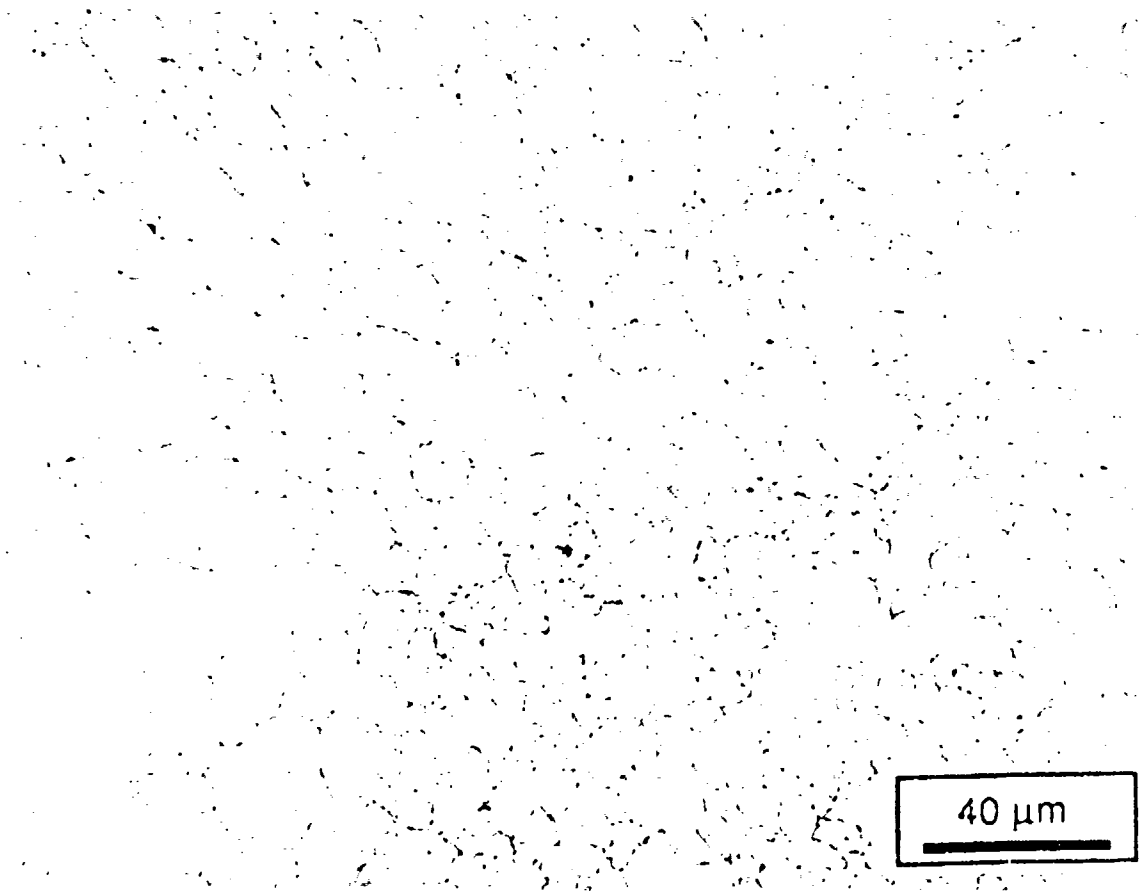

Figure A1. Photomicrograph of the prior austenite grain boundaries (normalized at 845°C).

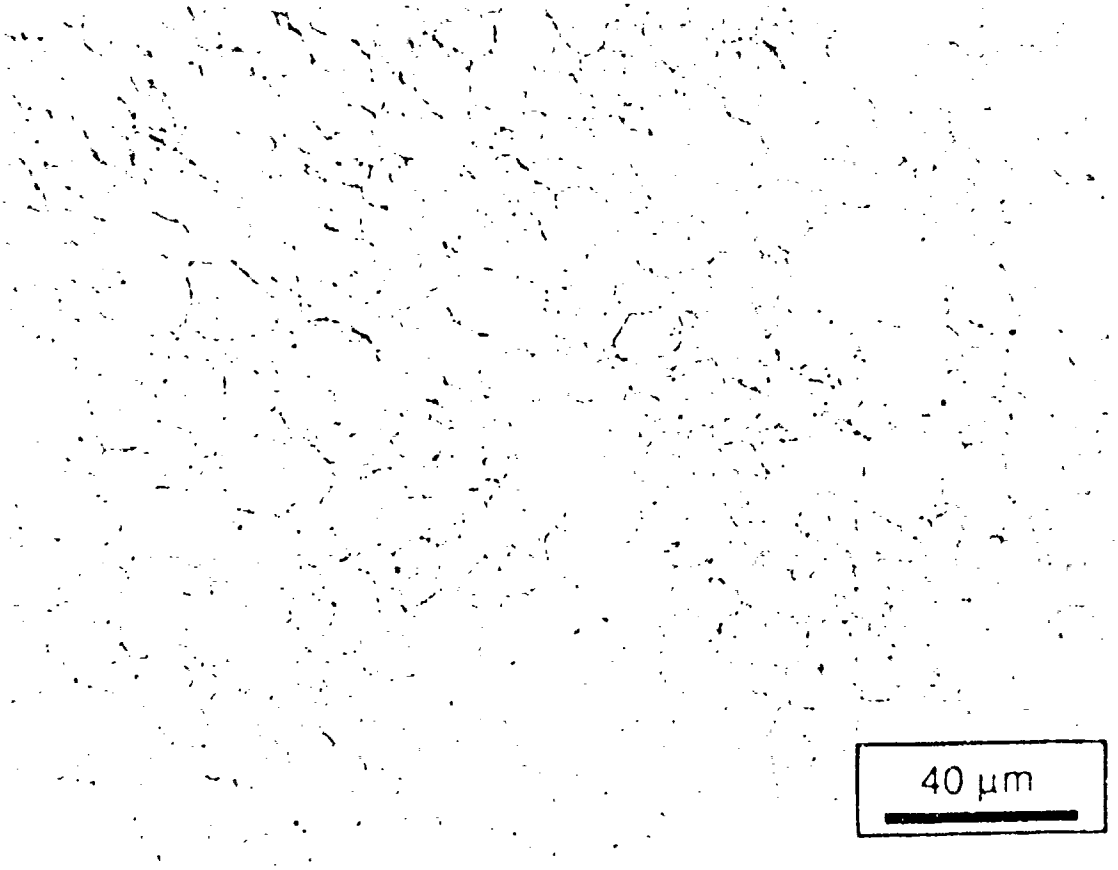

Figure A2. Photomicrograph of the prior austenite grain boundaries (normalized at 925°C).

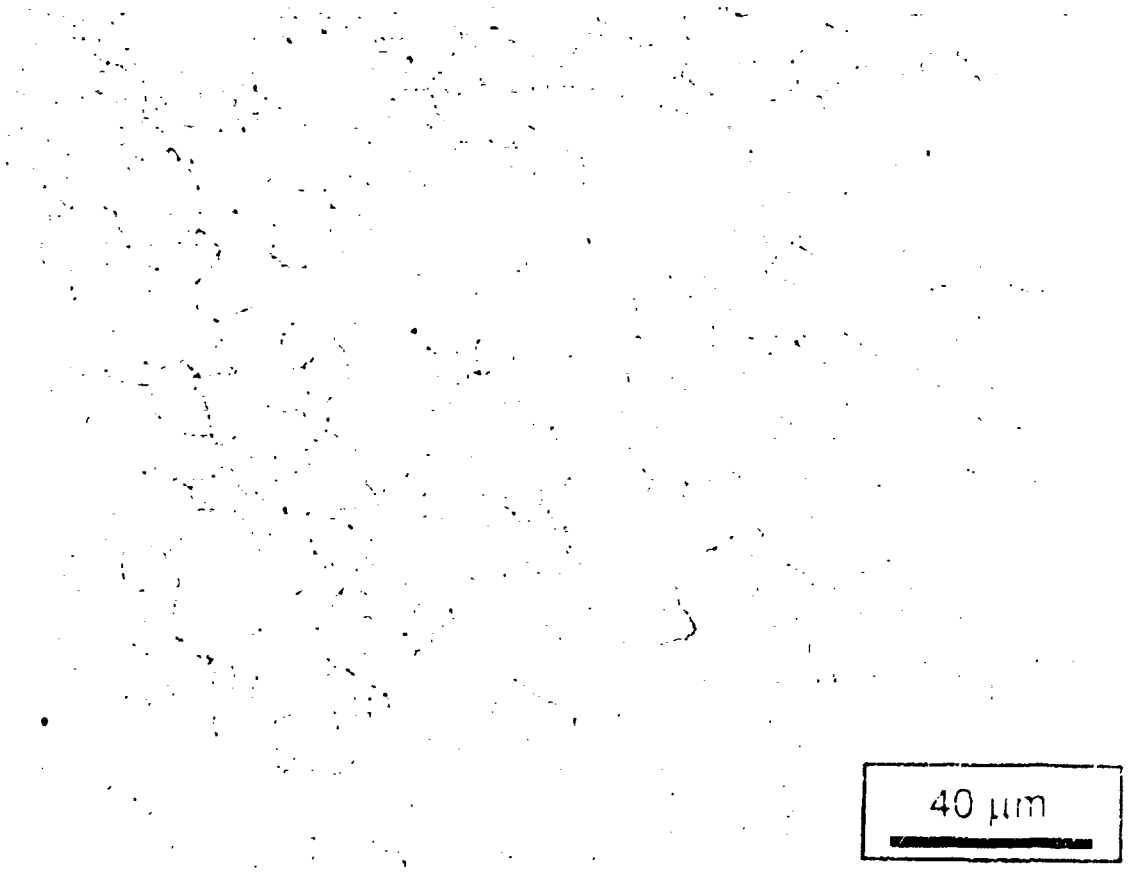

Figure A3. Photomicrograph of the prior austenite grain boundaries (normalized at 1010°C).

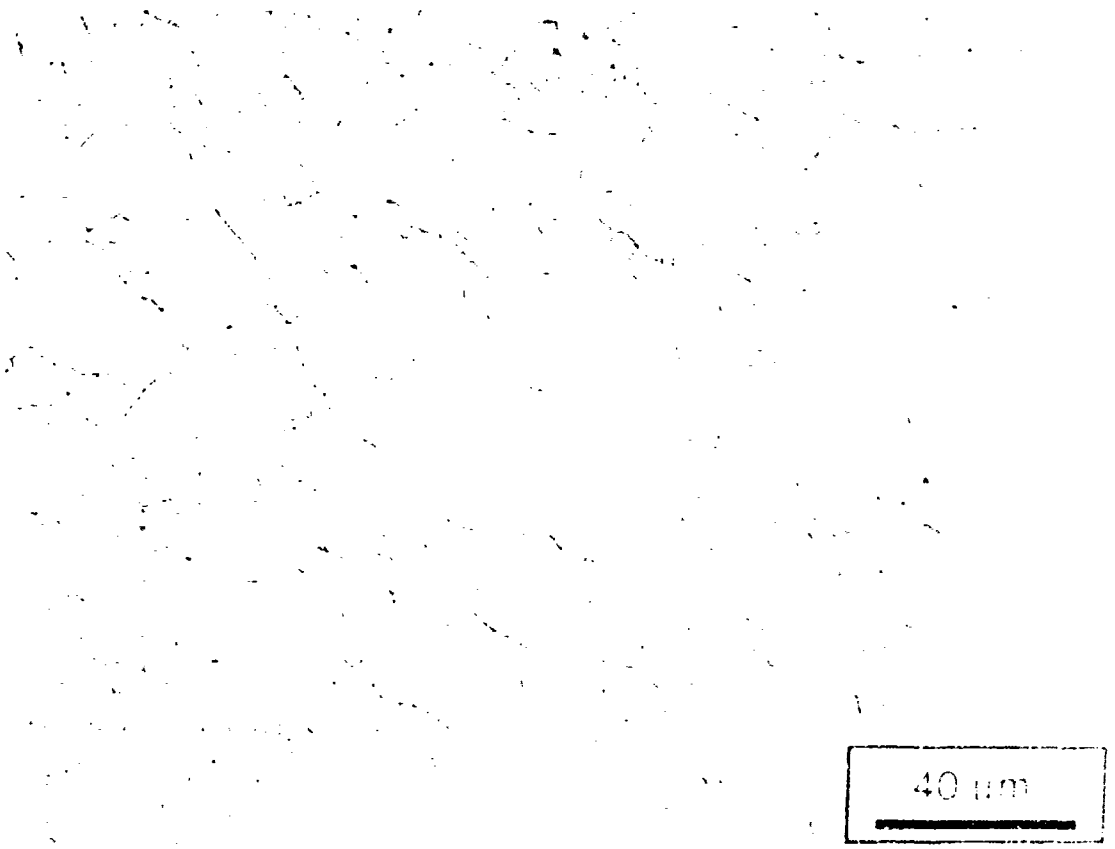

Figure A4. Photomicrograph of the prior austenite grain boundaries (normalized at 1095°C).

TABLE A. AUSTENITE GRAIN SIZE

Normalizing Temp. (°C)	Measured Diam. at 500X (inch)	ASTM Grain Size, N
845	0.107	12.5
925	0.110	12.4
1010	0.131	11.9
1095	0.150	11.5

Appendix B - Retained Austenite Determination

Retained austenite measurements were made on three specimens using the method described by Cullity* . A Cu K_α radiation x-ray diffraction trace was made of each specimen. A diffracted beam monochromator was employed to prevent the iron x-ray fluorescence from obscuring the diffracted peaks. The 200 and 311 austenite, 002/200 and 112/211 martensite integrated peak intensities were used in the direct comparison method. The relations used were as follows

$$R = \left(\frac{1}{V^2}\right)\left[|F|^2\ P\left(\frac{1+\cos^2 2\theta}{\sin^2\theta\cos\theta}\right)\right](e^{-2m})$$

$$\frac{I\gamma}{I\alpha} = \frac{R\gamma\ C\gamma}{R\alpha\ C\alpha}$$

$$F_{hkl} = \sum_{1}^{N} f_n\, e^{2\pi i(hu_n+kv_n+lw_n)}$$

F (Structure factor) = 4f for unmixed indices (fcc structures).

F = 2f for h+k+l f=even number (bcc structures).

F = 0 for h+k+l f=odd number(bcc structures).

* B. D. Cullity, *Elements of X-ray Diffraction*, Addison-Wesley, Reading, MA (1967).

P (Multiplicity factor) determined from Cullity† Appendix 9, p. 477.

$\sin \theta/\lambda$ determined from Cullity† Appendix 7, p. 472.

f (Atomic Scattering factor) determined from Cullity† , Appendix 8, p. 475.

e^{-2m} (Temperature factor) determined from Cullity† , Figure 14-5, p. 395.

Lorentz-Polarization factor determined from Cullity† , Appendix 10, p. 478.

V (Volume calculation) determined from Cullity† , Figure 12-5, p.352: Austenite: $V_\gamma = a^3 = 45.691 Å^3$, Martensite: $V_\alpha = a^2c = 23.844 Å^3$.

Table B1 presents the x-ray diffraction data used for retained austenite content calculations. Table B2 presents the retained austenite contents of the three specimens. An average of about 3% was found in each specimen.

TABLE B1. X-RAY DIFFRACTION

Peak	$1/V^2$ ($Å^{-6}$)	$\|F\|^2$	P	L-P	e^{-2m}	R
γ - 200	4.79×10^{-4}	2575.3	24	2.80	0.86	71.19
γ - 200	4.79×10^{-4}	4018.3	6	8.28	0.95	90.84
α-002/200	1.76×10^{-3}	745.0	6	4.82	0.91	34.78
α-112/211	1.76×10^{-3}	534.6	24	3.11	0.88	61.69

TABLE B2. PERCENT RETAINED AUSTENITE

Normalizing Temp. (°C)	Liquid N Refrigeration	Retained Austenite (Wt.%)
845	0	2.9 ± 1.2
1095	24 hours	3.0 ± 0.6
1095	0	3.2 ± 0.8

† B. D. Cullity, *Elements of X-ray Diffraction*, Addison-Wesley, Reading, MA (1967).

Appendix C - Crack Tip Stresses

First order approximation calculations were made of the stress fields around a crack tip subjected to mode I (tension) and mode II (shear) loading configurations.

Mode I

The cartesian coordinate stresses (σ_x, σ_y, and σ_{xy}) for mode I were calculated using the following relations

$$\sigma_x = \frac{K_I}{\sqrt{2\pi r}} \cos\frac{\theta}{2} \left(1 - \sin\frac{\theta}{2}\sin\frac{3\theta}{2}\right)$$

$$\sigma_y = \frac{K_I}{\sqrt{2\pi r}} \cos\frac{\theta}{2} \left(1 + \sin\frac{\theta}{2}\sin\frac{3\theta}{2}\right)$$

$$\sigma_{xy} = \frac{K_I}{\sqrt{2\pi r}} \sin\frac{\theta}{2}\cos\frac{\theta}{2}\cos\frac{3\theta}{2}$$

These results are presented graphically in Figure C1 as a function of the angle (θ). The stress values in the figure, and in all figures contained in Appendix C, stresses are in units of $K_I / \sqrt{2\pi r}$. The principal stresses were determined from these cartesian coordinate stresses using Mohr's circle construction

$$\sigma_1 = \frac{K_I}{\sqrt{2\pi r}} \cos\frac{\theta}{2} \left(1 + \sin\frac{\theta}{2}\right)$$

$$\sigma_2 = \frac{K_I}{\sqrt{2\pi r}} \cos\frac{\theta}{2} \left(1 - \sin\frac{\theta}{2}\right)$$

$$\sigma_3 = 0 \text{ (plane strain)}$$

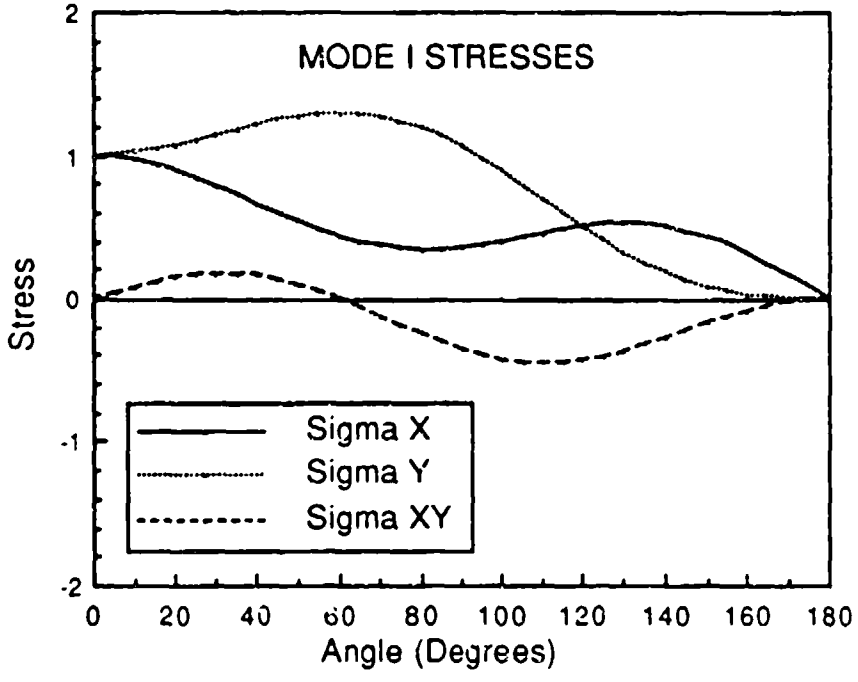

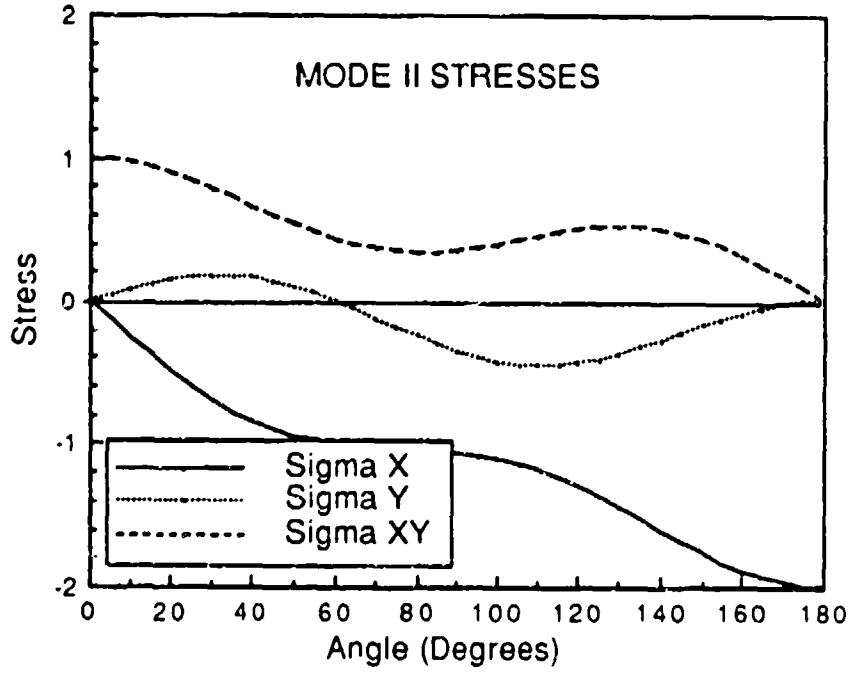

Figure C1. Comparison of the cartesian coordinate stresses for fracture modes I and II. Stresses are in units of $K/(2\pi r)^{1/2}$. Zero degrees lies directly in front of the crack tip.

The principal stresses are presented in Figure C2 as a function of the angle θ. The effective stresses were calculated in the following way and are presented in graphical form in Figure C3

$$\sigma_E = \frac{\sqrt{2}}{2}\sqrt{(\sigma_1-\sigma_2)^2 + (\sigma_2-\sigma_3)^2 + (\sigma_3-\sigma_1)^2}$$

The hydrostatic or mean stress is determined simply by averaging the three principal stresses (presented in Figure C4)

$$\sigma_H = \frac{\sigma_1 + \sigma_2 + \sigma_3}{3}$$

Mode II

The cartesian coordinate stresses (σ_x, σ_y, and σ_{xy}) for mode II were calculated using the following relations

$$\sigma_x = \frac{-K_{II}}{\sqrt{2\pi r}} \sin\frac{\theta}{2}\left(2 + \cos\frac{\theta}{2}\cos\frac{3\theta}{2}\right)$$

$$\sigma_y = \frac{K_{II}}{\sqrt{2\pi r}} \cos\frac{\theta}{2}\sin\frac{\theta}{2}\cos\frac{3\theta}{2}$$

$$\sigma_{xy} = \frac{K_{II}}{\sqrt{2\pi r}} \cos\frac{\theta}{2}\left(1 - \sin\frac{\theta}{2}\sin\frac{3\theta}{2}\right)$$

These results are presented graphically in Figure C1 as a function of the angle (θ). The stress values in the figure, and in all figures contained in Appendix C, stresses are in units of $K_{II} / \sqrt{2\pi r}$. The principal stresses were determined from these cartesian coordinate

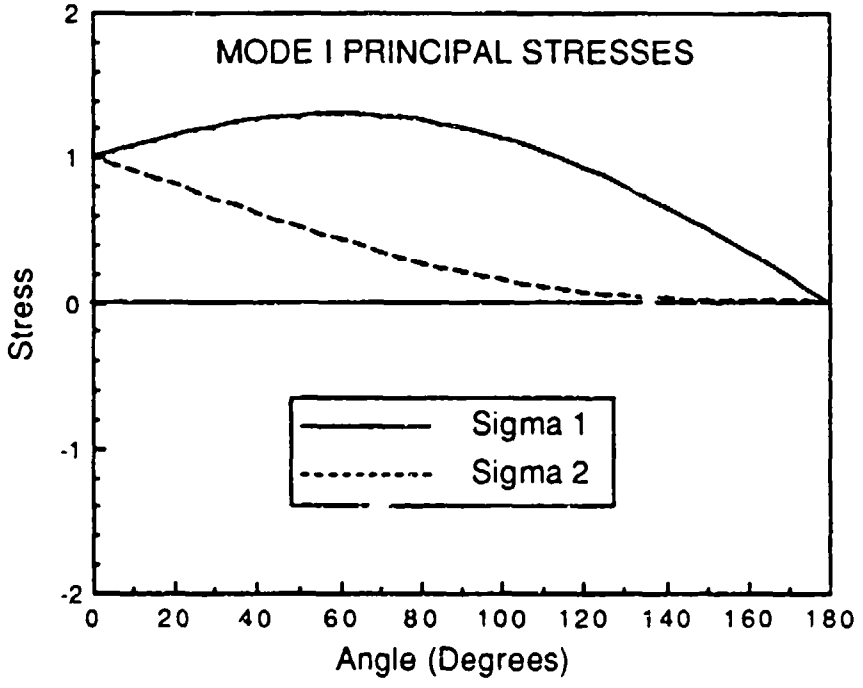

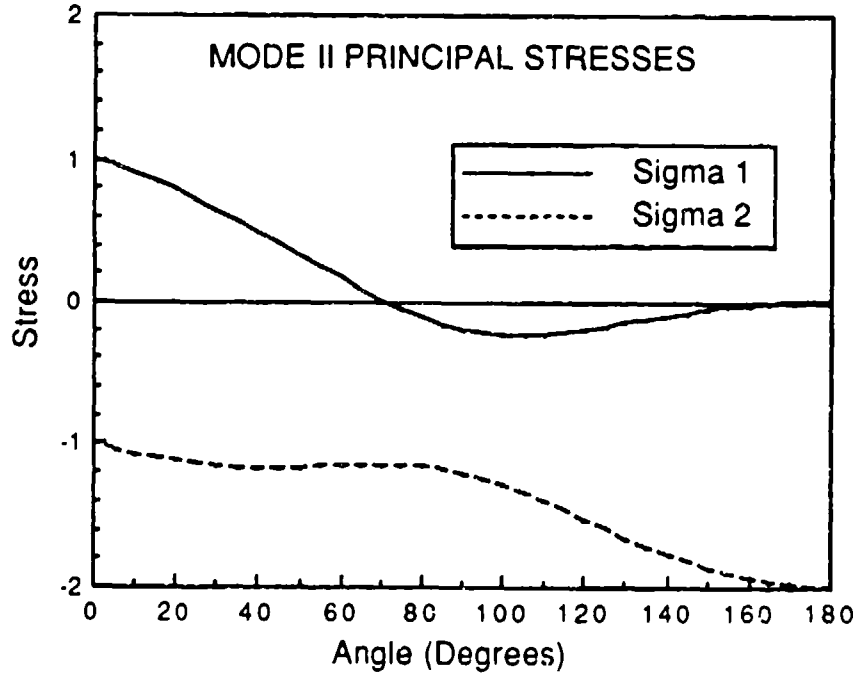

Figure C2. Comparison of the principal stresses for fracture modes I and II. Stresses are in units of $K/(2\pi r)^{1/2}$. Zero degrees lies directly in front of the crack tip.

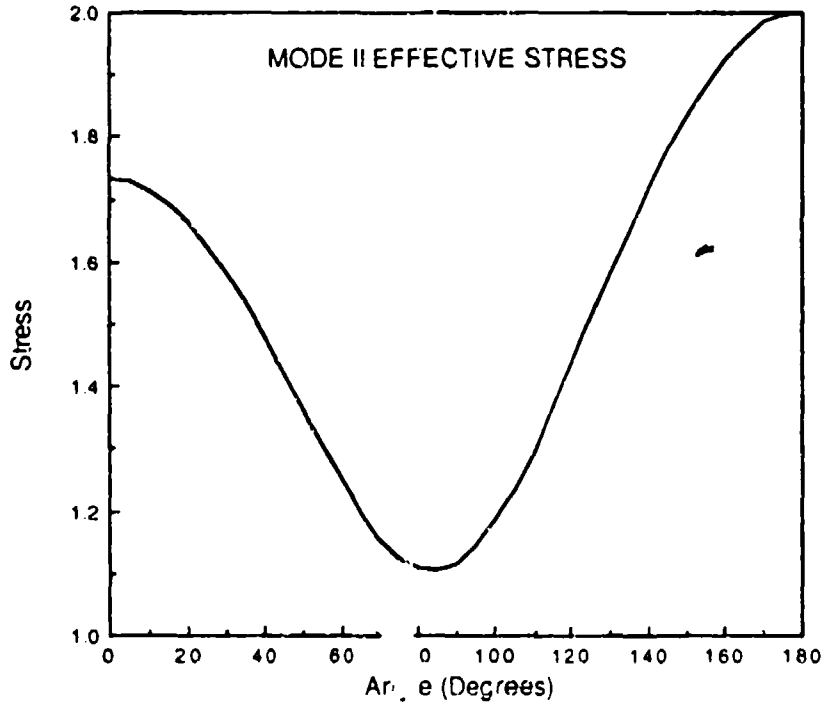

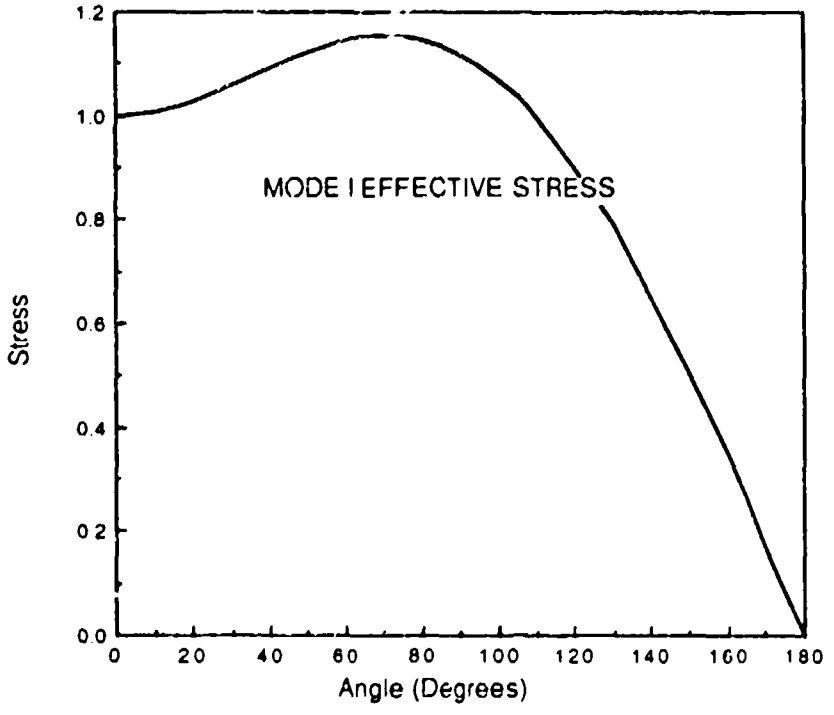

Figure C3. Comparison of the effective stresses for fracture modes I and II. Stresses are in units of $K/(2\pi r)^{1/2}$. Zero degrees lies directly in front of the crack tip.

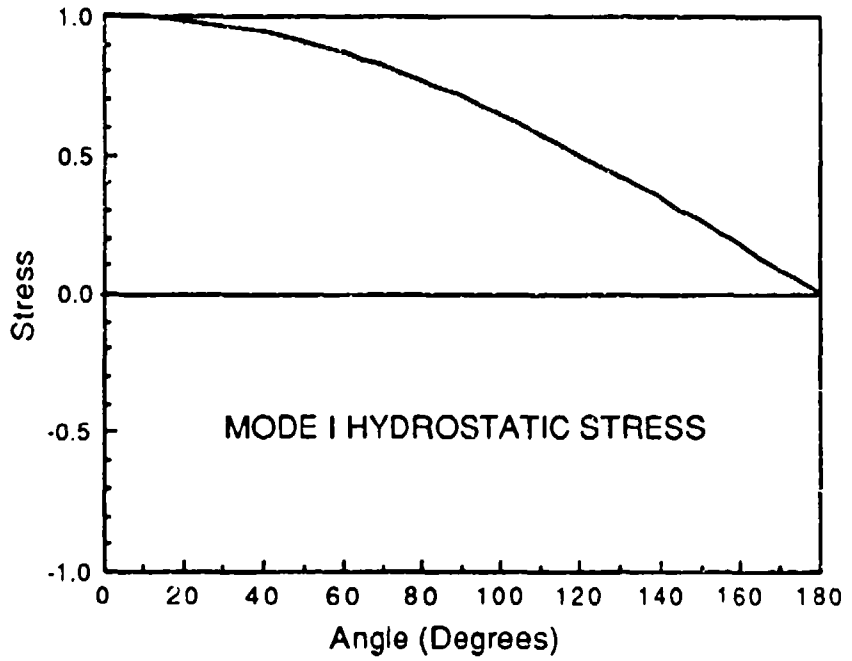

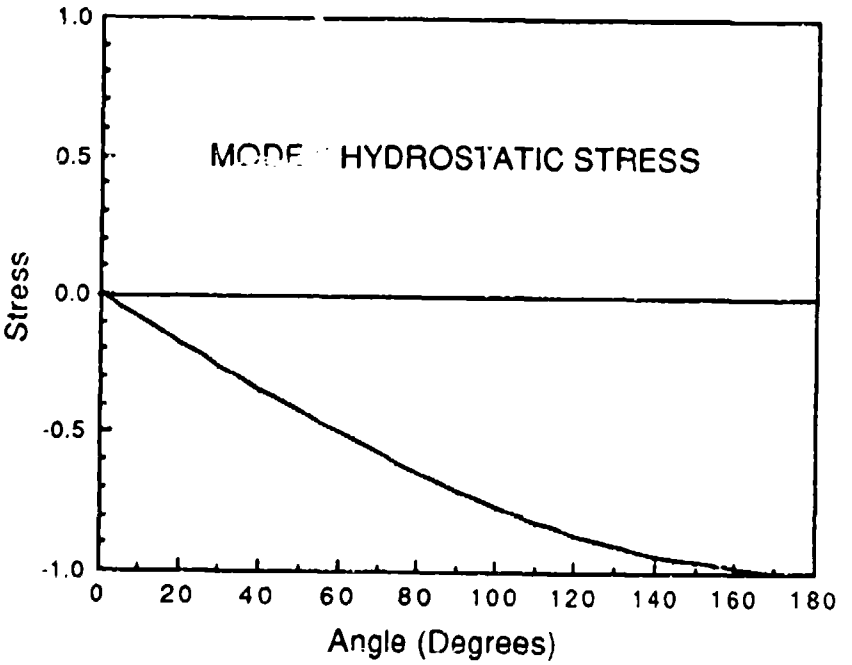

Figure C4. Comparison of the hydrostatic stresses for fracture modes I and II. Stresses are in units of $K/(2\pi r)^{1/2}$. Zero degrees lies directly in front of the crack tip.

stresses using Mohr's circle construction

$$\sigma_1 = \frac{K_{II}}{\sqrt{2\pi r}} \left[-\sin\frac{\theta}{2} + \sqrt{1 - \frac{3}{4}\sin^2\theta} \right]$$

$$\sigma_2 = \frac{K_{II}}{\sqrt{2\pi r}} \left[-\sin\frac{\theta}{2} - \sqrt{1 - \frac{3}{4}\sin^2\theta} \right]$$

$$\sigma_3 = 0$$

The principal stress results are presented in Figure C2. The effective and hydrostatic stresses were calculated using the same equations used for mode I (σ_E and σ_H). The results for these stresses are presented in Figures C3 and C4 respectively.

DISTRIBUTION LIST

No. of Copies	To
	Commander, U.S. Army Laboratory Command, 2800 Powder Mill Road, Adelphi, MD 20783-1145
1	ATTN: AMSLC-IM-TL
	Commander, Defense Technical Information Center, Cameron Station, Building 5, 5010 Duke Street, Alexandria, VA 22304-6145
2	ATTN: DTIC-FDAC
	Commander, U.S. Army Materiel Command, 5001 Eisenhower Avenue, Alexandria, VA 22333
1	ATTN: AMCLD
	Wyman-Gordon Company, R&D Department, North Grafton, MA 01536
1	ATTN: Dr. J. Hyzak
	Worcester Polytechnic Institute, Mechanical Engineering Department, 100 Institute Road, Worcester, MA 01609
1	ATTN: Dr. R. Biederman
1	Dr. Isa Bar-On
1	Dr. F. Tuler
1	Dr. R. Sisson
	Northwestern University, Department of Materials Science and Engineering, Evanston, IL 60208
1	ATTN: Dr. G. Olson
	Inland Steel Company, Research Laboratories, 3001 East Columbus Drive, East Chicago, IN 46312
1	ATTN: Dr. Hiroshi Yaguchi
	University of Kentucky, Department of Metallurgical Engineering and Materials Science, Lexington, KY 40506-0046
1	ATTN: Dr. M. Saum
	Lockheed Missiles and Space Company, Inc., 1111 Lockheed Way, Sunnyvale, CA 94086
1	ATTN: G. Hopple, O/48-92 B/195B
1	B. Boggs, O/48/92 B/195B
1	K. Massarat, O/81-22 B/157
	Norton Company, Goddard Road, Northboro, MA 01532-1545
1	ATTN: K. Siebein
	U.S. Secret Service, 1310 L Street NW, Room 800, Washington, DC 20005
1	ATTN: T. Thomas
	Harvard University, Pierce Hall, Cambridge, MA 02138
1	ATTN: Professor J. W. Hutchinson
1	Professor C. Hayzelden

No. of Copies	To
	Cambridge University, University Engineering Department, Cambridge CB2 IPZ, England
1	ATTN: Professor N. Fleck
	Massachusetts Institute of Technology, Cambridge, MA 02139
1	ATTN: Professor M. Cohen, Room 13-5046
1	Professor A. Argon, Mechanical Engineering Department
	Brown University, Box D, Providence, RI 02912
1	ATTN: Professor A. Needleman
1	Professor J. Duffy
1	Professor R. Clifton
	Colorado School of Mines, Metallurgical and Materials Engineering Department, Golden, CO 80401
1	ATTN: Professor G. Krauss
	Carenter Technology Corporation, Tool and Alloy R&D, P.O. Box 14662, Reading, PA 19612-4662
1	ATTN: M. Schmidt
1	R. Hemphill
	Drexel University, Materials Engineering Department, 32nd & Chestnut Street, Philadelphia, PA 19104
1	ATTN: Professor H. Rogers
	Los Alamos National Laboratory, MS G730, Los Alamos, NM 87545
1	ATTN: M. Stevens
	National Aeronautics and Space Administration, Lewis Research Center, 21000 Brookpark Road, Cleveland, OH 44135
1	ATTN: R. Buzzard
	University of California, San Diego, Department of Applied Mechanics and Engineering Sciences, La Jolla, CA 92093
1	ATTN: Professor S. Nemat-Nasser
1	Professor M. Meyers
1	Professor R. Asaro
	Director, U.S. Army Materials Technology Laboratory, Watertown, MA 02172-0001
2	ATTN: SLCMT-TML
1	Author

U.S. Army Materials Technology Laboratory,
Watertown, Massachusetts 02172-0001
THE INFLUENCE OF SECOND-PHASE DISPERSIONS ON SHEAR INSTABILITY AND FRACTURE TOUGHNESS OF ULTRAHIGH STRENGTH 4340 STEEL
John G. Cowie

Technical Report MTL TR 89-20, March 1989, 140 pp - Illus-tables, D/A Project 1L162105AH84

AD_____

UNCLASSIFIED
UNLIMITED DISTRIBUTION

Key Words

Ordnance steel
High strength alloys
Fracture (mechanics)

The resistance to shear instability and subsequent flow localization in ultrahigh strength (UHS) steels is dependent upon second-phase particle dispersions and the matrix strain hardening. The effect of the interparticle spacing (λ) to the geometric mean particle radius (R) ratio on the shear instability strain of UHS 4340 steel is discussed. Experimental results indicate a linear relationship exists between shear instability strain and this λ/R ratio. Microvoid nucleation softening associated with second-phase particles appears to be the dominant destabilizing event leading to fracture. Strain rate and hydro static compression effects are also discussed. Experimental results of modes I and II fracture toughness testing are compared and contrasted. A high hydrostatic tension field was found to be the cause for the lower mode I critical stress intensity factor (K_{Ic}) than mode II (K_{IIc}). The high hydrostatic tensile stress field induced early microvoid nucleation which promoted flow localization leading to fracture. However, both mode I (K_{Ic}) and mode II (K_{IIc}) critical stress intensity factors directly related to the critical particle distance ($\lambda/\sqrt{R}$). A bimodal fracture toughness model has been developed for this material and failure mechanism, which relates K_c to a combination of microstructural features and stress-strain behavior. Excellent agreement was found between calculated and measured mode I fracture toughness values. The calculated mode II fracture toughness did not relate as well to the measured toughness values due to the influence of hydrostatic compression on the shear instability strain.

U.S. Army Materials Technology Laboratory,
Watertown, Massachusetts 02172-0001
THE INFLUENCE OF SECOND-PHASE DISPERSIONS ON SHEAR INSTABILITY AND FRACTURE TOUGHNESS OF ULTRAHIGH STRENGTH 4340 STEEL
John G. Cowie

Technical Report MTL TR 89-20, March 1989, 140 pp - Illus-tables, D/A Project 1L162105AH84

AD_____

UNCLASSIFIED
UNLIMITED DISTRIBUTION

Key Words

Ordnance steel
High strength alloys
Fracture (mechanics)

The resistance to shear instability and subsequent flow localization in ultrahigh strength (UHS) steels is dependent upon second-phase particle dispersions and the matrix strain hardening. The effect of the interparticle spacing (λ) to the geometric mean particle radius (R) ratio on the shear instability strain of UHS 4340 steel is discussed. Experimental results indicate a linear relationship exists between shear instability strain and this λ/R ratio. Microvoid nucleation softening associated with second-phase particles appears to be the dominant destabilizing event leading to fracture. Strain rate and hydro static compression effects are also discussed. Experimental results of modes I and II fracture toughness testing are compared and contrasted. A high hydrostatic tension field was found to be the cause for the lower mode I critical stress intensity factor (K_{Ic}) than mode II (K_{IIc}). The high hydrostatic tensile stress field induced early microvoid nucleation which promoted flow localization leading to fracture. However, both mode I (K_{Ic}) and mode II (K_{IIc}) critical stress intensity factors directly related to the critical particle distance ($\lambda/\sqrt{R}$). A bimodal fracture toughness model has been developed for this material and failure mechanism, which relates K_c to a combination of microstructural features and stress-strain behavior. Excellent agreement was found between calculated and measured mode I fracture toughness values. The calculated mode II fracture toughness did not relate as well to the measured toughness values due to the influence of hydrostatic compression on the shear instability strain.

U.S. Army Materials Technology Laboratory,
Watertown, Massachusetts 02172-0001
THE INFLUENCE OF SECOND-PHASE DISPERSIONS ON SHEAR INSTABILITY AND FRACTURE TOUGHNESS OF ULTRAHIGH STRENGTH 4340 STEEL
John G. Cowie

Technical Report MTL TR 89-20, March 1989, 140 pp - Illus-tables, D/A Project 1L162105AH84

AD_____

UNCLASSIFIED
UNLIMITED DISTRIBUTION

Key Words

Ordnance steel
High strength alloys
Fracture (mechanics)

The resistance to shear instability and subsequent flow localization in ultrahigh strength (UHS) steels is dependent upon second-phase particle dispersions and the matrix strain hardening. The effect of the interparticle spacing (λ) to the geometric mean particle radius (R) ratio on the shear instability strain of UHS 4340 steel is discussed. Experimental results indicate a linear relationship exists between shear instability strain and this λ/R ratio. Microvoid nucleation softening associated with second-phase particles appears to be the dominant destabilizing event leading to fracture. Strain rate and hydro static compression effects are also discussed. Experimental results of modes I and II fracture toughness testing are compared and contrasted. A high hydrostatic tension field was found to be the cause for the lower mode I critical stress intensity factor (K_{Ic}) than mode II (K_{IIc}). The high hydrostatic tensile stress field induced early microvoid nucleation which promoted flow localization leading to fracture. However, both mode I (K_{Ic}) and mode II (K_{IIc}) critical stress intensity factors directly related to the critical particle distance ($\lambda/\sqrt{R}$). A bimodal fracture toughness model has been developed for this material and failure mechanism, which relates K_c to a combination of microstructural features and stress-strain behavior. Excellent agreement was found between calculated and measured mode I fracture toughness values. The calculated mode II fracture toughness did not relate as well to the measured toughness values due to the influence of hydrostatic compression on the shear instability strain.

U.S. Army Materials Technology Laboratory,
Watertown, Massachusetts 02172-0001
THE INFLUENCE OF SECOND-PHASE DISPERSIONS ON SHEAR INSTABILITY AND FRACTURE TOUGHNESS OF ULTRAHIGH STRENGTH 4340 STEEL
John G. Cowie

Technical Report MTL TR 89-20, March 1989, 140 pp - Illus-tables, D/A Project 1L162105AH84

AD_____

UNCLASSIFIED
UNLIMITED DISTRIBUTION

Key Words

Ordnance steel
High strength alloys
Fracture (mechanics)

The resistance to shear instability and subsequent flow localization in ultrahigh strength (UHS) steels is dependent upon second-phase particle dispersions and the matrix strain hardening. The effect of the interparticle spacing (λ) to the geometric mean particle radius (R) ratio on the shear instability strain of UHS 4340 steel is discussed. Experimental results indicate a linear relationship exists between shear instability strain and this λ/R ratio. Microvoid nucleation softening associated with second-phase particles appears to be the dominant destabilizing event leading to fracture. Strain rate and hydro static compression effects are also discussed. Experimental results of modes I and II fracture toughness testing are compared and contrasted. A high hydrostatic tension field was found to be the cause for the lower mode I critical stress intensity factor (K_{Ic}) than mode II (K_{IIc}). The high hydrostatic tensile stress field induced early microvoid nucleation which promoted flow localization leading to fracture. However, both mode I (K_{Ic}) and mode II (K_{IIc}) critical stress intensity factors directly related to the critical particle distance ($\lambda/\sqrt{R}$). A bimodal fracture toughness model has been developed for this material and failure mechanism, which relates K_c to a combination of microstructural features and stress-strain behavior. Excellent agreement was found between calculated and measured mode I fracture toughness values. The calculated mode II fracture toughness did not relate as well to the measured toughness values due to the influence of hydrostatic compression on the shear instability strain.